(Bio)Molecular Transport and Recognition in Heavy Ion Track-Etched Polymeric Nanopores

Vom Fachbereich Material- und Geowissenschaften
der Technischen Universität Darmstadt

zur Erlangung des akademischen Grades
eines Doktor rerum naturalium (Dr. rer. nat.)
genehmigte

Dissertation

von
M.Sc. Quoc Hung Nguyen
aus Dongnai (Vietnam)

Darmstadt 2013
D17

(Bio)Molecular Transport and Recognition in Heavy Ion Track-Etched Polymeric Nanopores

(Bio)molekularer Transport und Molekül-Identifizierung in Schwerionen-geätzten Nanoporen

genehmigte Dissertation von Quoc Hung Nguyen aus Dongnai (Vietnam)

1. Gutachten: Prof. Dr. rer. nat. Wolfgang Ensinger
2. Gutachten: Prof. Dr. rer. nat. Reinhard Neumann

Tag der Einreichung: 08.01.2013
Tag der Prüfung: 19.04.2013

Erklärung zur Dissertation

Hiermit versichere ich, die vorliegende Dissertation ohne Hilfe Dritter nur mit den angegebenen Quellen und Hilfsmitteln angefertigt zu haben. Alle Stellen, die aus Quellen entnommen wurden, sind als solche kenntlich gemacht. Ein Teil der Dissertation wurde bereits in wissenschaftlichen Journalen veröffentlicht, siehe *List of Publications*, und ist in der Dissertation mit Erlaubnis der Herausgeber der Journale reproduziert. Diese Arbeit hat in gleicher oder ähnlicher Form noch keiner Prüfungsbehörde vorgelegen.

Darmstadt, den 20. Juni 2013

_____

(Quoc Hung Nguyen)

Diese Arbeit wurde unter der Leitung von Prof. Dr. rer. nat. Wolfgang Ensinger im Fachgebiet Materialanalytik des Fachbereichs Materialwissenschaft der Technischen Universität Darmstadt in der Zeit von August 2008 bis Dezember 2012 durchgeführt.

Acknowledgements

It has been a long journey in order to finish my PhD study and I could not do it alone. Therefore, I would like to use this opportunity to thank all people who contributed to this thesis.

First of all I express my special thanks to my supervisor, Prof. Dr. W. Ensinger, for giving me the opportunity to do my doctoral work in his research group. I am so grateful for the constant support, encouragement and advice he has provided throughout my study, and also for allowing me the independence and flexibility to do my work.

I also want to present my great attitude to Prof. Dr. R. Neumann for being my second supervisor and for helping me to get the scholarship from Daimler-Benz Foundation so I could do my PhD study in Germany. I am so thankful for his guidance and enthusiasm, as well as for reading and correcting of my manuscripts and thesis.

I am very grateful for the continuous help of Dr. M. Ali during my PhD work. I specially acknowledge his guidance with experiments, new ideas and a lot of support with writing and corrections.

I would like to send many thanks to Prof. Dr. C. Trautmann for providing me the working place to perform my work at the Materials Research Department at GSI and for her great support with irradiation experiments.

Also I express my sincere thanks to:

- Dr. M. Rauber for his instruction of the nanowire fabrication process and the SEM measurements.
- Prof. Dr. Patricio Ramírez from the Polytechnic University of Valencia in Spain for the fruitful discussion and helping me with the theoretical calculations of surface charge density in nanopores which I presented in this thesis.
- Dipl.-Phys. V. Bayer for the useful discussions to this work.
- Dr. O. Picht and Dr. S. Müller for the support with some SEM measurements.
- All members of the GSI Materials Research Department for the great atmosphere during my work, enjoyed beamtime shifts and many help in daily life.

I would like to send my sweet thanks to my parents and my family for their care and support during my dotoral work. Especially I acknowledge my wife for her encouragements and taking care of our little daughter.

Last but not least I am grateful for the financial support from Daimler-Benz Foundation and Beilstein Institute during my research work.

Abstract

This thesis is focused on the potential applications of ion track-etched nanopores in polymeric membranes, such as molecular separation, gating and biosensing. The nanopores are fabricated in polyethylene terephthalate (PET) membranes by heavy ion track-etching technique. Ion track technology provides the feasibility to produce membranes with nanopores of desired diameters and geometries. The characterizations of the nanopores are performed by field emission scanning electron microscopy, replica technique and conductometry measurements. Heavy ion irradiation and subsequent track-etching lead to the generation of carboxylic groups (–COOH) on the inner pore walls. At neutral pH, nanopores are cation-selective due to the presence of ionized carboxylate groups ($–COO^-$) on the pore surface. The chemical modification of –COOH groups with amino-terminated molecules switches the surface polarity from negative to positive which in turn flipped the nanopore perm-selective behaviour. Polymeric membranes containing cylindrical nanopores are employed for the transport of ionic organic (bio)molecules through the nanopores. The nanopores have the ability to selectively transport and discriminate the molecules based on their size and charge. For the transport studies main focus is the modulation of pore density, pore diameter, ionic strength of buffer solution and electric field which affect the ionic selectivity and flux of the membrane. Moreover, the polyethyleneimine (PEI) modified pores are also applicable as gate to control the ionic/molecular flux across the membrane. Finally, single (conical and cylindrical) nanopores modified with boronic acid receptor are studied for the molecular recognition of monosaccharides and glycoprotein inside confined geometries. The recognition events are observed by measuring the current – voltage *(I–V)* curves in an electrolyte solution in the presence of glucose, fructose and glycoprotein separately.

Zusammenfassung

Die vorliegende Arbeit zeigt potenzielle Anwendungen Ionenspur-geätzter Nanoporen in Polymermembranen, wie zum Beispiel molekulare Trennung, Steuerung und Detektion. Die untersuchten Nanoporen wurden in Polyethylenterephthalat (PET) durch Schwerionenspurätztechnik erzeugt. Diese bietet die Möglichkeit, Nanoporen mit erwünschten Durchmessern und Geometrien herzustellen. Die Charakterisierung der Nanoporen wurde mittels Feldemissions-Raster-Elektronenmikroskopie, Replika-Technik und Leitfähigkeitsmessungen vorgenommen. Polymermembranen mit zylindrischen Nanoporen wurden für den Transport ionischer organischer Moleküle und Biomoleküle eingesetzt. Schwerionenbestrahlung und nachfolgendes Spur-Ätzen führen zur Erzeugung von Carboxyl-Gruppen (–COOH) an den inneren Porenwänden. Bei neutralem pH-Wert sind Nanoporen kationenselektiv aufgrund der Gegenwart von ionisierten Carboxylat-Gruppen ($–COO^-$) auf der Porenoberfläche. Die chemische Modifikation von –COOH-Gruppen mit Amino-terminierten Molekülen wechselt die Oberflächenpolarität von negativ zu positiv, wodurch das permselektive Verhalten der Nanoporen umgedreht wird. Die Nanoporen lassen bestimmte Analytmoleküle entsprechend ihrer Größe und Ladung bevorzugt hindurchtreten und diskriminieren andere. Das Hauptaugenmerk dieser Studie lag auf der Variation der Porendichte, des Porendurchmessers, der Ionenstärke der Pufferlösung und des elektrischen Felds, die die ionische Selektivität und den Durchfluss durch die Membranen beeinflussen. Zusätzlich sind die Polyethylenimin-(PEI)-modifizierten Poren auch anwendbar als Gate mit verschiedenen Zuständen des ionischen/molekularen Durchflusses durch die Membranen. Schließlich wurden einzelne (konische und zylindrische) Nanoporen, die mit Borsäure-Rezeptor modifiziert wurden, bezüglich der molekularen Erkennung von Monosacchariden und Glykoproteinen durch eingeschränkte Geometrie untersucht. Es wurden Erkennungsereignisse durch die Messung von Strom-Spannungs (*I-V*)-Kurven in einer Elektrolytlösung in Gegenwart von Glucose, Fructose und Glykoprotein erhalten.

Contents

1 Motivation and outline

The study of molecular and ionic transport in nanometer-sized pores has gained a lot of attention in recent years. At such length scales, structures have a high surface-to-volume ratio, leading to new physical phenomena that are not observed in macro- or micropores. A nanoscale pore promotes the interactions between translocating molecules (or ions) and pore walls. Such interactions would lead to the control over molecular (or ionic) transport, which become the basis for sensing biomolecules, separation and purification applications.

In living systems, ion channels (pores) which are formed by membrane proteins are present in the cellular membranes. It is well-known that biological ion channels in living organisms facilitate the diffusion of ions, water or small organic molecules across the cell membranes, providing the basis for communication with each other, for example, for metabolic and signaling purposes [1]. So far, biological pores have been used as a model system to investigate transport phenomena at the nanoscale [2, 3]. They offer precisely controlled structures and interfacial chemistry. However, they are not suitable for practical applications due to the fragility and sensitivity of the embedding lipid bilayer induced by external parameters such as pH, temperature, and salt concentration. To overcome these difficulties, various routes have been explored to meet the challenge of fabricating pores in solid-state materials with the ability to mimic functions of biological ion pores [4, 5]. Among synthetic platforms, nanopores produced by track-etching technique have gained a lot of attention during recent years. Track-etched membranes offer several advantages over conventional membranes. By using track-etching technique, it is possible to produce nanopores with controlled pore size, shape and areal density. Therefore, membranes with the required transport properties can be fabricated.

This thesis is focused on the transport properties of nanopores fabricated in heavy ion-track polyethylene terephthalate (PET) membranes. Up to now, the study of nanopores in PET membranes has mostly concentrated on potential applications of single conical nanopores as biomolecular sensors [6-8], stimuli-responsive systems [9, 10] and integration in nanofluidic devices [11, 12]. In this study, sets of experiments have been made to understand the transport of ionic species based on their electrical charge and molecular size. Great effort has been undertaken to use the cylindrical nanopores in PET membranes for transport of ionic species (organic molecules and biomolecules), which is crucial for separation and purification applications. Furthermore, this study also addressed the ability of using nanopores as a gate for the control of ionic and molecular flow across the membrane. Further, it also considered potential applications of single pores for sensing of saccharides and glycoprotein. The structure of the thesis is organized as follows:

Chapter 2 describes the basis of the transport phenomena in nanopores in electrolyte solution. This is the cornerstone for the understanding of experimental results in this study. In this section, the electrical double layer (EDL) concept is introduced. Electrostatic interactions and electrokinetic effects in nanopores are also discussed in this chapter.

Chapter 3 presents the process of fabrication and characterization of track-etched single pores and multi-nanopores in PET membranes. At first, the irradiation of polymer foils with heavy ions is described in detail. Then, the track-etching processes for the transformation of latent tracks into cylindrical multi-nanopores, and single conical and cylindrical nanopores are explained. The characterization of

nanopores by different methods is also described in this chapter. Furthermore, the procedures of nanopore functionalization, mass-transport experiment and current-voltage measurement are included.

Chapter 4 involves results and discussion of the following experiments:

- Examination of the transport of molecules (organic and bio-molecules) in cylindrical nanopores. Various parameters, such as pore diameter, buffer concentration, pore density and electric field, have been taken into account for their effect on the membrane performance.
- Presentation of the theoretical concept of Poisson and Nernst-Planck (PNP) equations to describe the ionic transport through a cylindrical nanopore. By fitting the calculations to experimental results, the density of charged groups inside nanopores is estimated.
- The application of nanopores as a molecular gate in the presence of adenosine-triphosphate (ATP) to control the anion flux across the membrane. The gating experiments were performed in both single conical pores and cylindrical pores.
- The molecular recognition of saccharides and glycoprotein inside single conical nanopores modified with boronic acid receptors. The change in the current – voltage curves is observed upon the addition of saccharide and glycoprotein in the electrolyte solutions.

Finally, Chapter 5 summarizes the main points discussed in the thesis and presents an outlook for future work.

2 Introduction

Recent advancements in micro-/nanofabrication techniques have opened new opportunities to construct well controlled nanofluidic systems which can be employed in many analytical applications [13]. In general, nanofluidic research involves the study of phenomena which occur in confined structures of nanometer scale (typically 1-100 nm). At such small scale, systems have enhanced surface-to-volume ratio, leading to new observations which result from the interactions with the molecules. Therefore, further exploring interactions between molecules and nanofluidic systems, and improving molecular manipulation at this level provide us with new tools for chemical analysis and detection. Up to now, considerable work has been performed to demonstrate the utilization of nanofluidic structures as various miniaturized components and systems for chemical analysis on small length and volume scales. Such miniaturization would be very helpful because the sample volume needed for the analysis is reduced. In addition, the reduction in physical dimensions in nanoscale structures also leads to the decrease in analysis time due to the enhanced mass transport rate [14, 15]. Thus, it is critical to control molecular transport at small length scales by using materials and structures that can discriminate molecules based on their characteristics (size, charge, molecular shape, etc.).

Practically, miniaturization of nanodevices also helps to reduce the size of laboratory devices. As a result, power consumption, waste, material and operating costs can also be reduced. Although working at the nanometer scale normally involves increasing the complexity in the experiments, one could benefit some advantageous factors using nanofluidic systems such as (a) new transport phenomena, (b) enhanced surface-to-volume ratio, (c) diffusion as a main transport mechanism, and (d) ability to integrate large molecules into small (1–10-nm) physical structures [16]. Therefore, it is extremely important to construct nanofluidic systems that address all four criteria.

2.1 Nanochannels and nanopores

Nanofluidic structures are normally categorized into nanopores and nanochannels, but sometimes these two terms can be used interchangeably to represent similar systems. Nanopores are typically formed in biological or synthetic membranes. They can have different geometries (cylindrical or conical) and are circular in shape along the pore length [17]. Some examples of nanopores are engineered protein pores [18], nanopipettes [19], and track-etched nanopores in polymer membranes [20]. Furthermore, a pore can also be produced by drilling a membrane with a femtosecond laser [21], a focused ion beam [22], or a focused electron beam [23]. The use of an electron beam offers an additional ability to precisely control pore diameter by shrinking effect. Dekker and coworkers reported the success of using transmission electron microscope (TEM) as a tool to control the size of silicon oxide nanopores with single-nanometer precision [24]. In this report, a pore in a silicon membrane was initially fabricated by electron-beam lithography and anisotropic etching. Then, a silicon oxide layer with a thickness of 40 nm was formed on the silicon surface by thermal oxidation. Finally, the pore size was reduced to a single nanometer under a high energy electron beam exposure. This can be achieved because the silicon oxide is fluidized which then leads to a shrinking of the pore. Figure 2.1a shows a TEM image of a 19-nm silicon oxide nanopore and Figure 2.1b-d displays the images obtained while imaging the pore in a TEM microscope. The electron beam exposure causes the pore to shrink gradually to a size of about 3 nm.

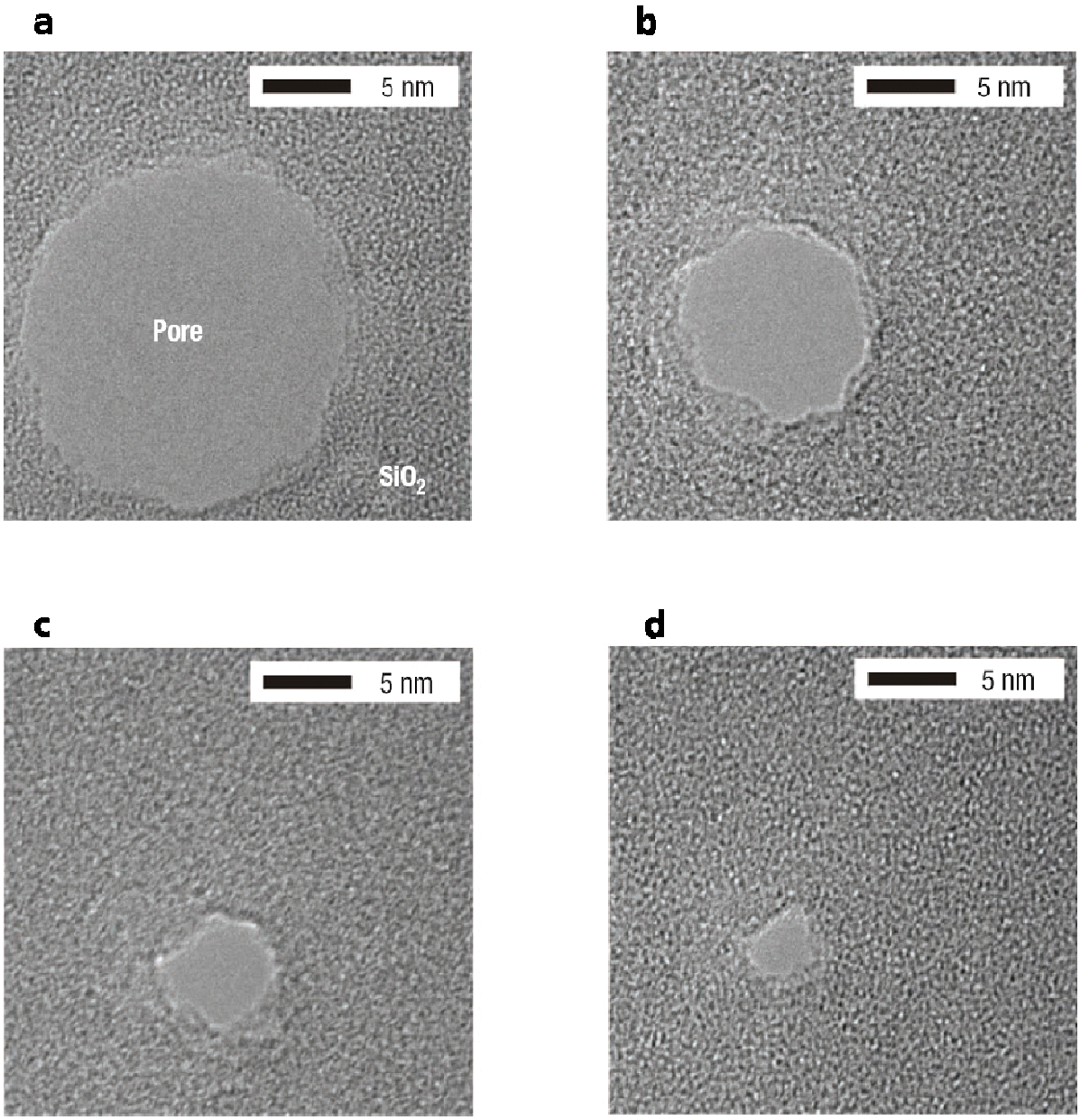

Figure 2.1: (a) Transmission electron microscope image of a silicon oxide nanopore. The pore diameter is 19 nm. (b)-(d) Sequence of micrographs obtained during imaging of the pore in a TEM microscope. The electron beam shrinks the pore gradually to a size of about 3 nm. Adapted by permission from Macmillan Publishers Ltd: Nature Materials [24], copyright (2003).

Nanochannels are typically formed in the plane of a substrate. They have dimensions of depth and width with at least one dimension in the nanometer range and are not circular in shape along the channel [17]. The structures of nanochannels are normally patterned by micro- and nanofabrication techniques. Some examples of fabrication processes of nanochannels are sacrificial layer deposition [25], photolithography [26], and electron beam lithography [27]. Nanochannel structures can also be produced by the combination of electron beam and optical lithography techniques. For instance, Mannion et al. used this procedure to fabricate nanochannels on a fused silica wafer of 500 μm thickness [28]. Some electron micrographs of these nanostructures (100 nm deep and 90 nm wide) are shown in Figure 2.2.

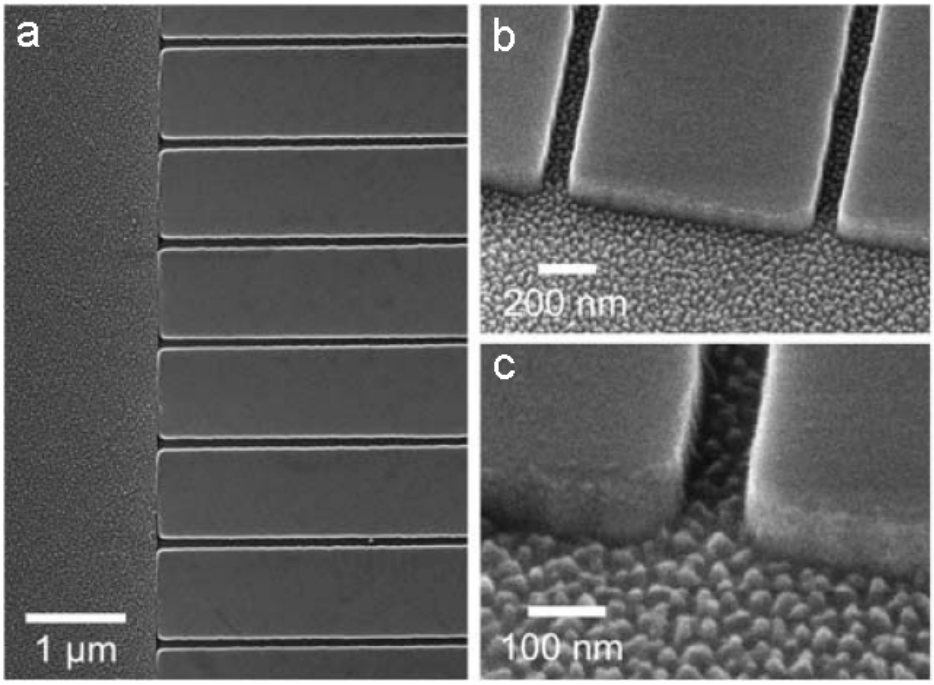

Figure 2.2: Electron micrographs of nanochannel array in 500 μm fused silica wafer. (a) Top-down view showing the interface between the microchannel and the array of nanochannels. Channel depth is 100 nm. (b) Entrance to two nanochannels. The channels are 90 nm wide. (c) Closer view of a nanochannel entrance. Adapted with permission from J.T. Mannion et al. [28], copyright (2006) Elsevier.

Molecular transport in nanopores having characteristic dimensions is a critical component of a large number of separation technologies. Also, the capabilities to fabricate and modify nanopores at the molecular level provide a benefit for chemical analysis. Therefore, it is necessary to understand the mechanism of ion transport inside the nanopores so that nanofluidic devices can successfully be exploited in practical applications. This is especially important when pore dimensions reduce to nanometer range. At this length scale, some phenomena for instance double-layer overlap, diffusion, ion permittivity and surface charge become dominant [29, 30]. Particularly, when the pore size is comparable to the Debye length, the concentration of ions inside the nanopore is controlled by the surface charge. Therefore, the surface charge in nanopores plays a crucial role in controlling the flow of charged species [31]. Moreover, under an applied electric field, surface charges on pore walls induce electrostatic ion screening and electrokinetic effects, including electrophoresis and electro-osmosis. Hence, understanding how fluid behaves inside the nanopores and how ions/molecules are transported through the pores is essential in order to manipulate precisely fluids and analytes for practical applications.

2.2 Electrical double layer

When a charged surface of a solid object is placed into an electrolyte solution, an electrical double layer (EDL) is created on this surface. This EDL is composed of oppositely charged ions (counter-ions) developing in the area close to surface in order to neutralize the surface charges. The counter-ions in the EDL will not be uniformly distributed throughout the liquid phase, but will be concentrated near the charged surface.

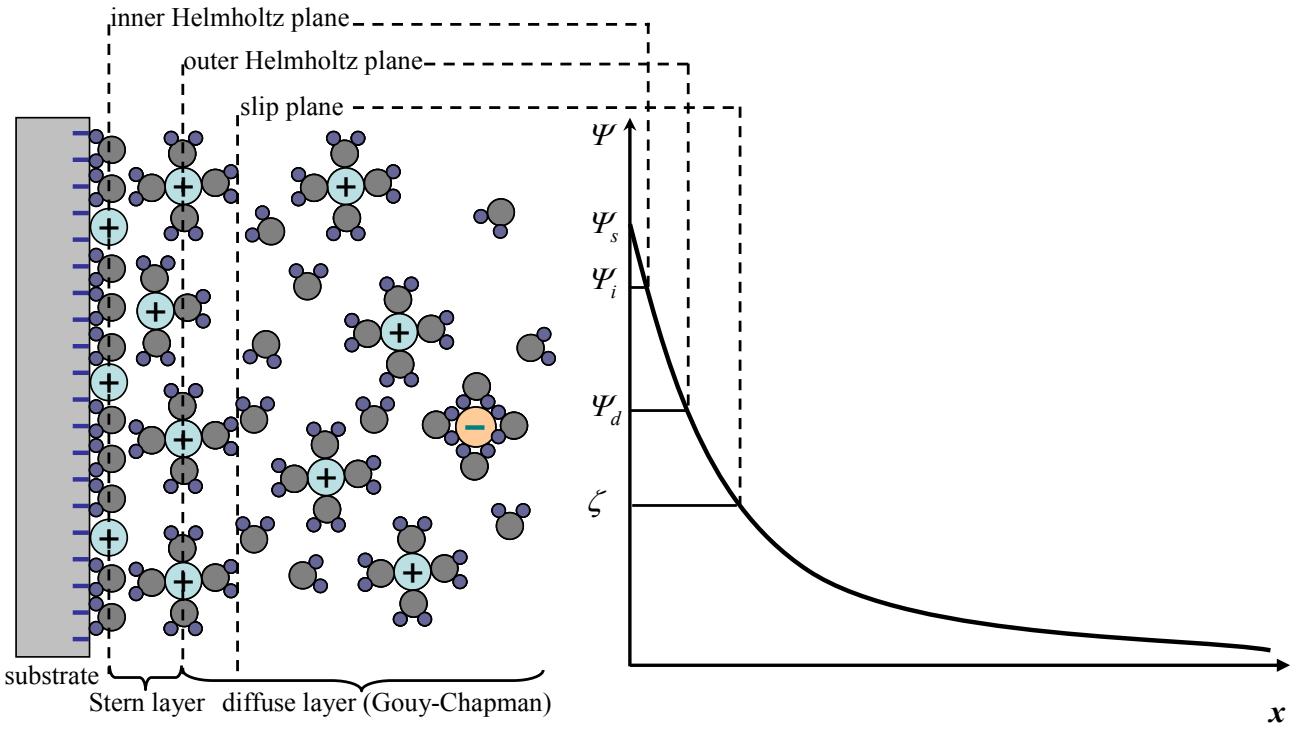

Figure 2.3: Gouy-Chapman-Stern model of electrical double layers at solid-electrolyte interface (left) with the corresponding potential distribution Ψ *versus* the distance x from the surface (right). The solid is illustrated with a negative surface potential Ψ_s. The inner Helmholtz plane layer and the outer Helmholtz plane layer have the potential Ψ_i and Ψ_d, respectively. The diffuse layer containing the slip plane with the potential ζ [32].

Up to now, several models have already been introduced to describe and explain the EDL. First, the Helmholtz model was used to describe the EDL as two charged layers separated by a fixed distance (a simple capacitor). This model considers each charged layer as a single layer of ions adsorbed at the surface. Then, Gouy and Chapman developed a model illustrating the EDL as a surface charge and a charged layer of diffused mobile ions, named a diffuse layer in which the electric potential decays exponentially away from the surface to the electrolyte solution. Later, Stern combined the two Helmholtz and Gouy-Chapman models together. Figure 2.3 demonstrates the combined Gouy-Chapman-Stern model which represents the EDL to be composed of an internal Stern layer (Helmholtz layer) and an outer diffuse layer (Gouy-Chapman layer). The Stern layer comprises an inner Helmholtz and an outer Helmholtz plane which have the potential Ψ_i and Ψ_d, respectively. In the inner Helmholtz plane, co-ions and counter-ions are not hydrated and specifically absorbed on the charged surface, whereas the outer Helmholtz plane contains only hydrated and partially hydrated counter-ions. The outer diffuse layer, where both mobile co-ions and counter-ions are present, contains the slip plane which bears the ζ potential. In practical, the measurement of the Ψ_d potential is quite difficult. Therefore, Ψ_d can be approximated with the ζ potential because the outer Helmholtz plane and the slip plane are normally located very close to each other [30].

Since the EDL is characterized by the high amount of counter charges required to screen the net charge on the surface, there is excess of counter-ions and a deficit of co-ions in the region close to a surface. For instance, if a surface is negatively charged, the concentration of cations in EDL is higher that that of anions. The resulting ion distribution calculated from Gouy-Chapman model is presented in Figure 2.4. It is shown that almost all the surface charge is balanced mainly by the accumulation of counter-ions (cations). The reduction of co-ions (anions) also plays a role but with less impact [33].

In principle, one may expect that there are only counter-ions in the EDL for neutralizing the charge on the surface if there is no Brownian motion of ions in the solution. However, the ions move randomly in the liquid phase due to their thermal motion at a given temperature. Therefore, if ions have enough thermal energy to overcome the electrostatic energy, there are also the abilities that co-ions from the bulk solution may enter the EDL and counter-ions may escape from the EDL to the bulk liquid. This leads to the definition of the Debye screening length, a characteristic distance from the solid surface where the potential energy of the ions and the kinetic energy of the counter-ions ($kT/2$) are about the same for each degree of freedom [34]. Debye length, or the thickness of the EDL (λ_D), can be calculated using the following formula:

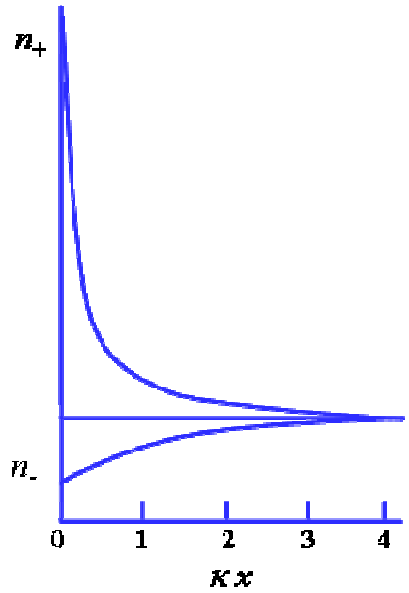

Figure 2.4: Distribution of ion concentration (from Gouy-Chapman model) of cation (n_+) and anion (n_-) in the area close to a negatively charged surface as a function of the dimensionless number κx [33].

$$\lambda_D = \kappa^{-1} = \sqrt{\frac{\varepsilon_r \varepsilon_0 k_B T}{2 N_A e^2 I}} \tag{1}$$

where

I is the ionic strength of the electrolyte (mole·m^{-3}),
ε_0 is the permittivity of free space (C^2·J^{-1}·m^{-1}),
ε_r is the dielectric constant,
k_B is the Boltzmann constant (J·K^{-1}),
T is the absolute temperature (K),
N_A is the Avogadro number (mole^{-1}),
e is the elementary charge (C).

It can be seen that λ_D is inversely proportional to the square root of the ionic strength (or electrolyte concentration). The Debye length depends solely on the properties of the liquid and not on the surface properties such as charge or potential. For example, the Debye length is ~ 800 nm for deionized water (limited by the autoprotolysis of water), and ranges from 1 to 100 nm depending on the bulk ion concentration.

2.3 Electrostatic interactions inside nanopores

When a charged nanopore is placed in an electrolyte solution, EDL developing from each pore wall results in a high concentration of counter-ions inside the nanopore. The counter-ions could be positively charged or negatively charged depending on the type of surface charge on the pore walls. For example, if the pore surface is negatively charged, the pore is filled mainly with cation, and *vice versa*. The concentration of the counter-ions inside a nanopore is governed by both the electro-neutrality and the surface charge density on the pore walls [35].

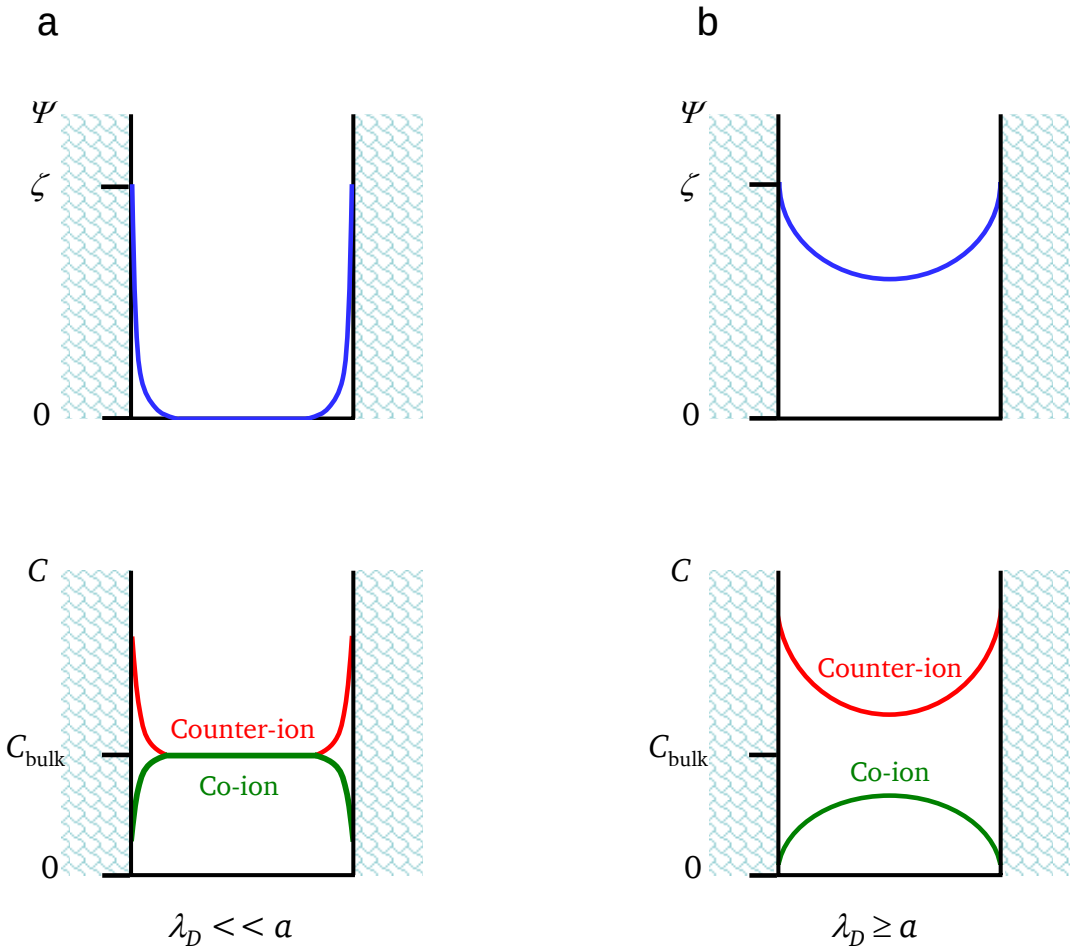

Figure 2.5: Ion concentrations and potential profiles in a negatively charged nanopore. (a) At high ion concentration ($\lambda_D << a$) the potential and ion concentration in the pore are almost not affected by surface charge. (b) At low ion concentration ($\lambda_D \geq a$) the potential remains high in the whole pore. The counter-ions are accumulated while co-ions are excluded.

The profiles of electric potential and ion concentrations in a negatively charged nanopore are sketched in Figure 2.5. At high bulk ion concentration, at which the Debye length is much smaller than the pore radius ($\lambda_D << a$), the potential decays fast, reaching zero at very small distance from the surface. As a result, the EDLs containing mainly counter-ions are thin, close to the pore walls. At a certain distance from the wall, where the electric potential is zero in most part of the pore (Figure 2.5a), the concentrations of counter-ions and co-ions are the same and equal to that outside in bulk solution. On the other hand, if the bulk ion concentration is low enough, to the point where the thickness of the EDL is

larger than the pore diameter ($\lambda_D \geq a$), there would be the overlapping of EDLs inside the nanopore, as shown in Figure 2.5b. In this case, the potential remains high inside the whole nanopore and there is accumulation of counter-ions inside the pore and exclusion of co-ions from the pore [36]. In general, if the surface is negatively charged, the nanopore will be mainly filled with cations. In contrast, the concentration of anions is much higher than cations inside the pore when the pore surface is positively charged. This implies that the surface charge on the pore wall causes the electrostatic effect which can influence the concentration of ions inside the pore having a radius equal to the thickness of the EDL.

Electrokinetic effects in nanopores

When a charged nanopore in electrolyte solution is subjected to an applied electric field, the transport of solvent liquid, ions and solvatized molecules inside the pore can be manipulated by means of electrokinetic effects. Typically, electrokinetic phenomena in nanopores involve the movement of the fluid (electro-osmosis) and electrically charged molecules and particles (electrophoresis) [37]. Since the presence of EDL affects the electrostatic potential and ion distribution inside the pore, it also has an influence on the motion of water and charged molecules and particles if an external electric field is applied.

a. Electro-osmosis

Electro-osmosis occurs when an electric field is applied across the length of a nanopore, leading to the movement of the solvent liquid (water) inside the pore. Under an applied electric field, the mobile counter-ions in the EDL experience an electrostatic force which causes the ions to migrate toward the oppositely charged electrode. The movement of counter-ions will cause viscous interactions with the liquid inside the pore, leading to a flow of liquid toward the same direction with counter-ions [38]. For instance, in a negatively charged nanopore, the EDL contains mainly cations which will migrate toward the cathode. This movement will result in a electro-osmotic flow of liquid toward the same direction (cathode) [38].

b. Electrophoresis

Electrophoresis is an effect, commonly used to move ions and charged molecules in nanopores [39]. Here, it is worth noting that a charged molecule in an electrolyte solution also has the EDL of counter-ions in order to screen the charge of that molecule. In this case, there are some competitive processes governing the direction in which the molecule would move. For example, if a molecule is negatively charged, it will move to the positively charged electrode (anode) due to electro-migration under an applied electric field. However, the mobile counter-ions (cations) in the EDL surrounding the charged molecule also move, leading to the movement of the liquid (electro-osmosis) in the area close to the molecule in the opposite direction (cathode). Therefore, the moving direction of a charged molecule is dependent on factors such as the number of charges on that molecule, the concentration and viscosity of the aqueous medium, as well as the strength of the electric field.

2.4 Types and applications of nanopores

2.4.1 Single nanopores

Biological pores

One of the most potential applications in nanopore research is the sensing of individual molecules which is very important in biochemistry, biophysics, and chemistry. Within the past decade, the research using this single-molecule technique has increased exponentially due to the simplicity of the approach. In nanopore sensing, individual molecules are detected when they translocate through a single pore, leading to detectable changes in ionic current through the pore [40]. At the beginning, biological nanopores were used for the detection of ionic species and molecules because they have a well-controlled geometry and chemical structure. So far, the most widely used biological pore in chemical analysis is the bacterial protein pore α-hemolysin (αHL). The cross-section of a α-hemolysin pore is shown in Figure 2.6. This protein pore is very popular because it has some advantageous features. Firstly, the structure of αHL is robust and there is no moving parts inside the pore. As a result the fluctuation of ionic current signal can be avoided. Secondly, there is no specific binding of analyte inside αHL pore [40]. And thirdly, the pore walls of αHL can be functionalized by genetic mutation and chemical mean [41]. However, biological pores are not stable because they are embedded in lipid bilayers which are fragile and may rupture. Therefore, it is required to have membranes which are stable in experiments with long recording time. Also, the membranes should also be stable if they are integrated into sensing devices which can withstand pressure fluctuations or mechanical forces.

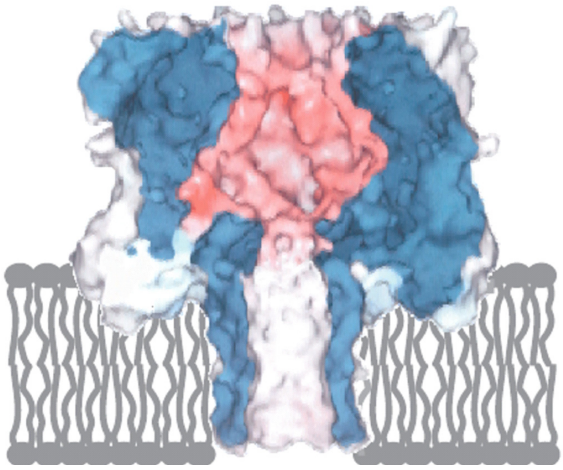

Figure 2.6: The cross-sectional view of a α-hemolysin pore. Adapted by permission from Macmillan Publishers Ltd: Nature Biotechnology [42], copyright (2008).

Solid-state nanopores

Solid-state (synthetic) nanopores nowadays offer a great alternative to the biological systems because they are stable in external conditions such as temperature, pH, and ionic strength. In addition, by using synthetic platforms, it is allowed for long-recording measurements and the synthetic pores can be easily integrated into sensing devices. Silicon nitride (Si_3N_4) membrane is known as the first template used for

solid-state nanopore fabrication. By using an ion-beam, the nanopore was sculptured into Si_3N_4 membrane [43]. The method of ion beam sculpting can also be used for other materials such as silica, Al, poly(methyl methacrylate) and polyimide [44]. For molecular sensing, the detection of single molecules is recorded by current changes as they translocate through the pore. As an example, Figure 2.7 shows molecular events of a 5-nm nanopore in a Si_3N_4 membrane separating two compartments filled with electrolyte solution. After applying a voltage bias, the current through the pore was measured as a function of time. In the presence of DNA molecules, the ionic-current blockades were observed indicating the translocation of DNA through the nanopore.

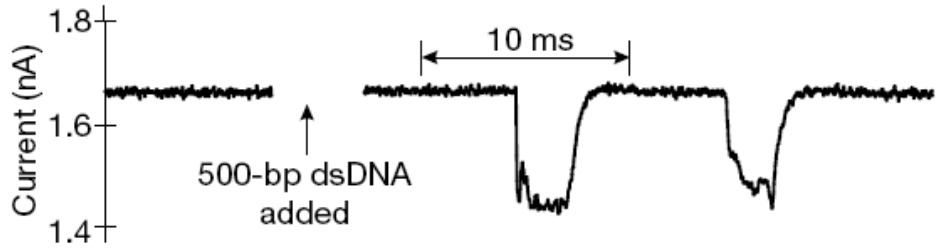

Figure 2.7: Translocation of double-stranded DNA, 500 base pairs long, through 5-nm nanopore in a Si_3N_4 membrane. Adapted by permission from Macmillan Publishers Ltd: Nature [43], copyright (2001).

Glass nanopipettes have recently become another alternative for molecule sensing. The fabrication process of glass nanopipettes normally is performed with commercially available pipette pullers. Generally, a glass capillary is first heated in the middle with a laser. Then the heated glass capillary can be mechanically pulled until it breaks at the narrow neck, thereby forming two open-ended nanopipettes. This process can produce nanopipettes with opening diameter of several tens of nanometers [45, 46]. Glass pipettes were also employed for the detection of DNA molecules attached to gold nanoparticles by observing the pore current blockades when the molecules pass through a pipette pore [46].

The other candidates for single non-biological pores are polymer nanopores prepared by the track-etching technique. It has been mostly applied to prepare pores in polymer films such as polyethylene terephthalate (PET), polycarbonate (PC), polyimide (PI) and mica [47]. In this technique, the polymer membranes are exposed to a high-energy heavy ion beam, followed by a wet etching process that creates nanopores along the damaged zones (latent tracks) caused by the heavy ions along their trajectory. Especially, single conically shaped nanopores possess unique transport properties. A conical pore having a small tip opening exhibits much lower resistance in solution than a cylindrical pore of the same diameter. In addition, conical nanopores show nonlinear current–voltage behaviour (rectification) at certain pH and ionic strength of electrolyte solutions which can be exploited for ionic devices [48]. Furthermore, conical nanopores in polymer membranes can be used as sensing platforms to detect DNA molecules via pore current blockades [49, 50] or protein molecules by ionic current rectification [6, 51, 52].

2.4.2 Nanoporous membranes

The transport using nanoporous (multi-nanopore) membranes offers great potential for many applications, for instance protein separation and purification, drug delivery and biomedical applications [53]. In order for the membrane to be applied in membrane technology, it is necessary to control the performance of the nanoporous membrane, i.e. the selectivity and the molecular flux (throughput). In addition, the fabrication of membranes containing nanopores must also be economical and scalable [54]. Nanoporous membranes cover a wide range of materials. They can be inorganic (metals, ceramics etc.), organic (polymeric), or composite materials. Here, some nanoporous membranes with well-ordered pore structure are highlighted for the application of controlled molecular transport and separation.

Anodized membranes

Anodic aluminum oxide (AAO) membranes represent one of the most common nanoporous materials. In general, the fabrication of AAO membranes involves the anodization of aluminum (Al) substrates in an aqueous acidic solution, for instance oxalic, sulphuric, chromic or phosphoric acids [55]. This process leads to the oxidation of Al to form aluminum oxide and the formation of pore arrays which are self-organized on the substrate. Then the remaining Al substrate is etched away in a mixture solution of HCl and $CuCl_2$. The geometry and morphology of the nanopores can be easily controlled by adjusting the conditions during the anodization processes. In general, nanoporous AAO membranes containing closely packed hexagonal pores of 10–200 nm in diameter can be fabricated. The typical pore densities in these membrane are of the order of 10^{11} pores cm^{-2} and the pore length is about several tens of μm due to the chemical mechanisms of the fabrication process. As examples, scanning electron microscope (SEM) images of the surface and the cross section of an AAO membranes are shown in Figure 2.8 presenting a close-packed array of approximately hexagonal cells.

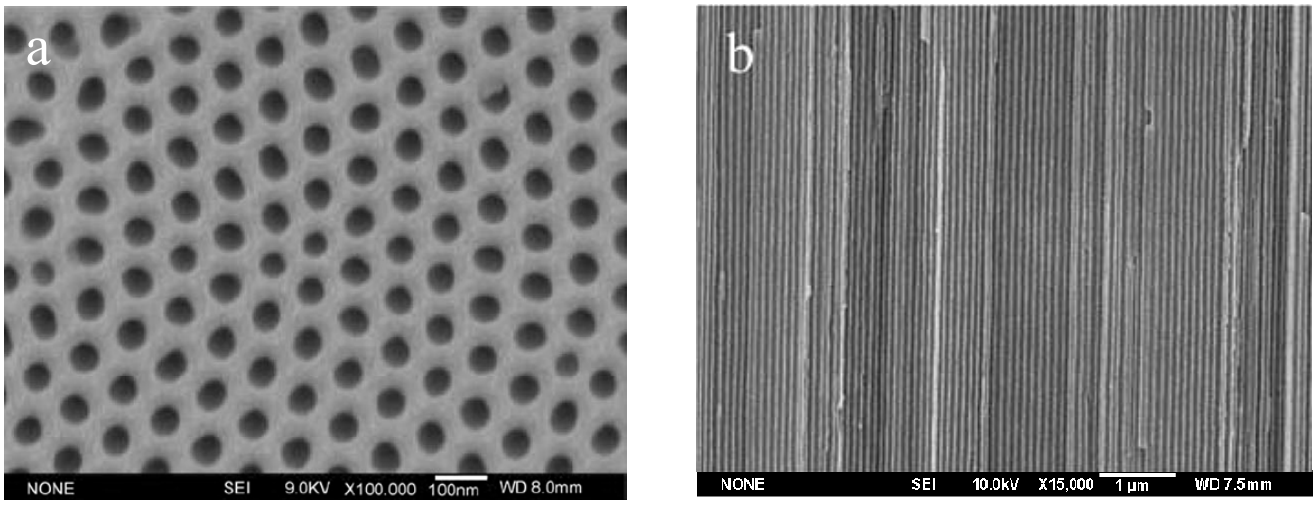

Figure 2.8: (a) SEM micrograph of the surface of a nanoporous AAO membrane showing a close-packed array of approximately hexagonal cells . The average pore diameters a are 50 nm. Adapted with permission from P. Gu et al. [56], copyright (2004) Springer. (b) SEM image of the cross-section of a AAO template. Adapted with permission from X.Y. Sun et al. [57], copyright (2005) Elsevier.

AAO membranes have been intensively studied for diffusion and separation of molecules. For instance, the diffusion of crystal violet molecules, encapsulated in sodium dodecylsulfate micelles, was studied in AAO membranes containing pores with diameter ranging from 20 to 200 nm [58]. This study indicated that AAO membranes can be suitable for drug delivery applications. Furthermore, AAO membranes have also been chemically modified for the study of the detection and separation of DNA molecules [59]. AAO membranes are normally chosen for the investigations because they are quite inexpensive and widely available. Also, the fabrication process of these membranes is well-known and simple. However, AAO membranes are thick (~ 60 μm), leading to low transport rates (molecular fluxes) because the molecular diffusion rate is inversely proportional to pore length. Therefore, they are not applicable in many separation and filtration processes [54].

Microfacricated Membranes

Recently, the development of micro- and nanofabrication technologies has provided new tools to fabricate cylindrical arrays of nanopores in silicon (Si) and silicon nitride (Si_3N_4) membranes. These processes have the advantages for the control of pore diameter and for the integration of such nanopores into microfluidic devices. Tong *et al*. have used focused ion beam (FIB) etching technique to fabricate an array of uniform cylindrical nanopores in an ultrathin silicon nitride membrane [60]. A SEM image of the nanoporous membrane containing pores with diameter about 25 nm is shown in Figure 2.9a. The authors proved that the membranes can withstand high temperatures and that they are inert to aggressive chemicals. Also, ultrathin nanoporous silicon membranes (Figure 2.9b) have been fabricated and applied for the separation of macromolecules based on their size and charge [61]. However, one of the disadvantages of this technology is that the production of these membranes is still costly. Therefore, it is necessary to find alternative methods for inexpensive fabrication of nanoporous membrane with good separation performance.

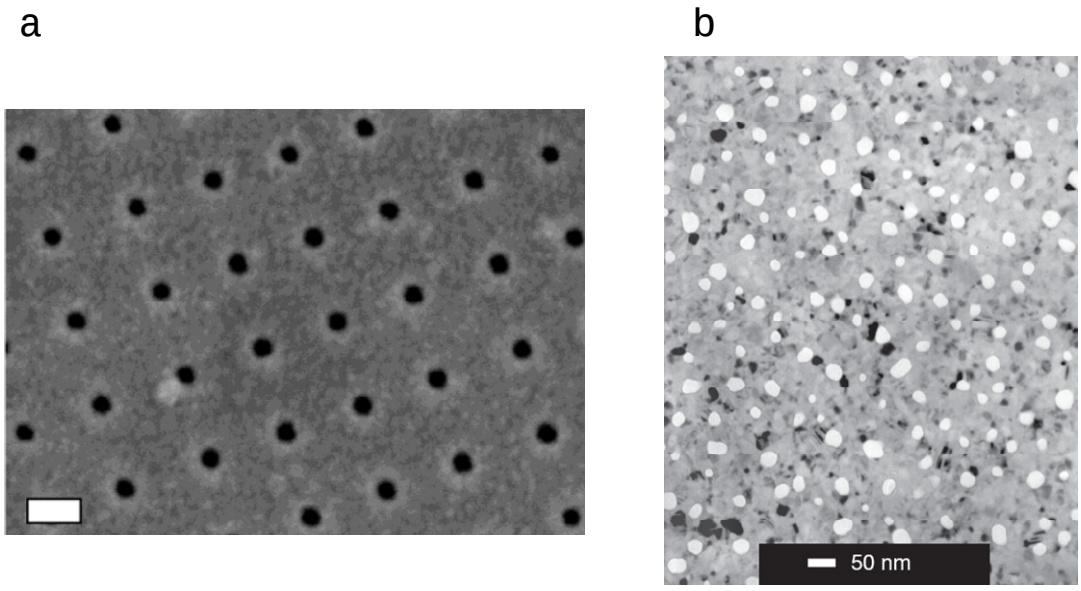

Figure 2.9: (a) SEM image of 25-nm nanopores, drilled by FIB in a 10-nm Si_3N_4 membrane (scale bar: 50 nm). Adapted with permission from reference [60], copyright (2004) American Chemical Society. (b) A TEM image of a nanoporous silicon membrane (15-nm-thick). The nanopores in this image appear as bright spots while nanocrystalline silicon is in grey or black color. Adapted by permission from Macmillan Publishers Ltd: Nature [61], copyright (2007).

Track-etched nanoporous membranes

Ion-track technique is the most common method used for the fabrication of nanoporous polymeric membranes. With this technique, it is quite easy to control the pore size by changing the conditions in the etching process (etching time, temperature and etchant concentration). The density of the pores per unit area can be controlled by adjusting the density of the projectile ions (ion fluence). The commonly used track-etched membranes include PC, PET, and PI of various thicknesses ranging from 5-100 μm. Track-etched nanopores are randomly distributed and normally cylindrical or conical in geometry. A SEM image of a track-etched membrane containing cylindrical nanopores is shown in Figure 2.10 [62]. Up to now, commercial track-etched membranes are widely available with the highest achievable pore density of approximately 6 x 10^8 pores cm^{-2} [63, 64]. The low pore density will limit the transport rates of molecules through the membranes, making them not sufficient for many applications.

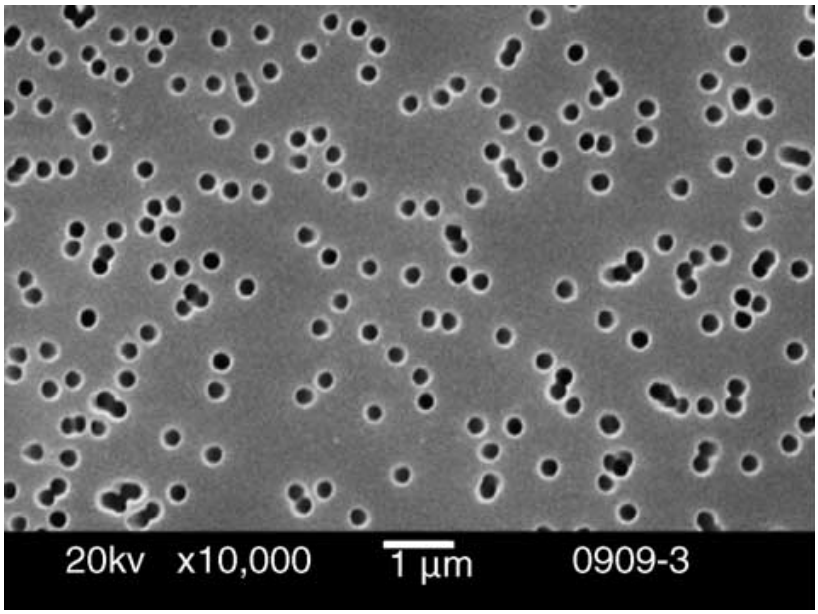

Figure 2.10: SEM image of a polycarbonate track-etched nanoporous membrane. Adapted with permission from R. Xie et al. [62], copyright (2005) Elsevier.

In this work, track-etched nanopores (single and multi-nanopores) fabricated in PET membranes are employed for selective molecular permeation nad biosensing purposes. With the unique facility for heavy ion irradiation at the UNILAC (GSI, Darmstadt), membranes with a variety of pore densities (ranging from single pore to multi-nanopores) can be produced. We are interested in PET membranes because they show good mechanical strength, flexibility and stability, as well as the ability of surface modification to introduce new functionalities to the pore walls. Membranes containing cylindrical nanopores are used to study the molecular transport of ionic species. The experimental studies are aimed at optimising the parameters to obtain high selectivity and throughput of these membranes which are suitable for separation applications. Furthermore, modified nanopores are also studied for their capabilities to be employed as a molecular gate and saccharides/glycoprotein recognition inside the confined geometries.

3 Experimental details

3.1 Irradiation of polymer membranes

The nanopores studied here are fabricated by using the heavy ion track-etching technique. In the first step, the polymer foils are irradiated with swift heavy ions, creating cylindrical damage zones (latent tracks). Then, the transformation of these ion tracks into pores is achieved by selective chemical etching. In this study, polyethylene terephthalate (PET) membranes (Hostaphan RN 12, Hoechst) of 12 μm thickness are used as templates for ion irradiation. The irradiation of polymer membranes is performed with heavy ions (^{238}U or ^{197}Au) having a kinetic energy of up to 11.4 MeV per nucleon, provided by the linear accelerator UNILAC (GSI, Darmstadt).

When an energetic heavy ion travels through the material, it is slowed down and transfers a certain amount of energy per path unit to the material (energy loss) along its trajectory, creating a damage trail in the material [65]. In the case of track formation in polymers, the energy transfer of the charged projectile creates the excitation and ionization of molecules and atoms. Afterwards, electron collision cascades occurring in the hydrocarbon matrix lead to the formation of highly exited unstable molecules (radicals) which results in homolytic bond breaking [66]. Figure 3.1 shows the envisioned character of track formation in a polymer [47].

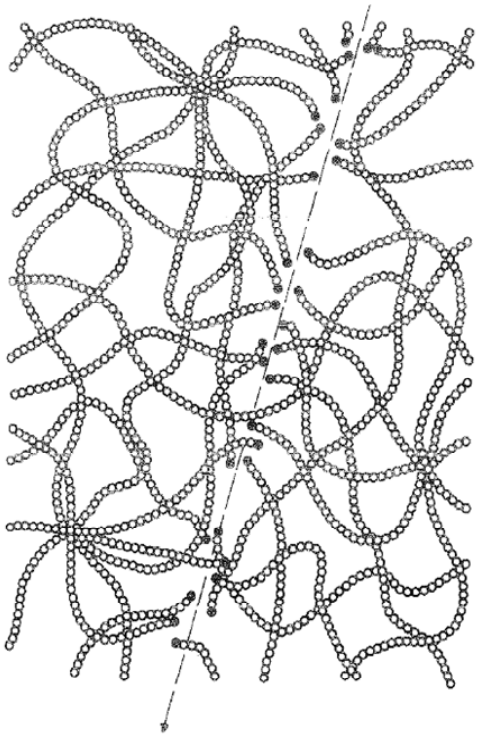

Figure 3.1: Track formation in a polymer involving chain scission and the formation of new functional groups [47].

Energy loss

The energy loss of an ion is defined as dE/dx which is dependent on mass and energy of the ion. In heavy ion irradiation, the energy loss is mainly composed of electronic energy loss, $(dE/dx)_{\text{electronic}}$ and nuclear energy loss, $(dE/dx)_{\text{nuclear}}$. At high energy (typically > 0.1 MeV/u), the electronic energy loss is dominating through inelastic interaction between the projectile ions and electrons, causing the excitation or ionization of target atoms. When the projectile slows down and its energy is reduced to the point where the electron shell of the target atoms can no longer be penetrated. At such low energies (typically below 0.01 MeV/u), the nuclear energy loss, $(dE/dx)_{\text{nuclear}}$, dominates through elastic collisions with the target atoms, whereby the energy and momentum of the projectile are directly transferred to the atoms.

Projectile range

The projected range R of an ion depends on its energy loss dE/dx in the material and is given by following relation:

$$R = \int_0^{E_0} \left(\frac{dE}{dx} \right)^{-1} dE \tag{2}$$

In order to estimate energy loss and projected range, computer simulation methods have been developed to calculate the motion of ions in a medium. The best known simulation program is SRIM (Stopping and Range of Ion in Matter) [67]. For instance, Figure 3.2a presents the calculated energy loss (nuclear and electronic) for an Au ion with specific energy 11.4 MeV/u penetrating a PET membrane. At such high kinetic energy of an ion, it is clear that the electronic energy loss dominates the total energy loss while the contribution of nuclear energy loss is minor. Figure 3.2b depicts the projected range plotted *versus* ion energy. For Au ions with kinetic energy of 11.4 MeV/u, a calculated ion range of approximately 160 μm in PET is obtained by the SRIM Code.

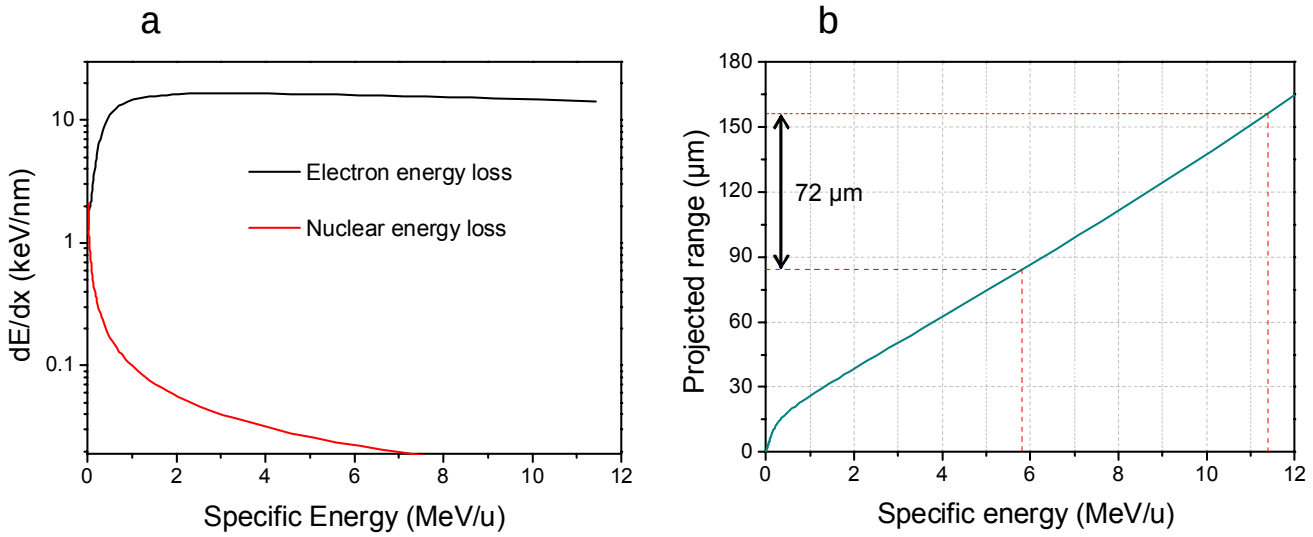

Figure 3.2: Energy loss and ion range calculated for Au ions in a PET membrane using the SRIM2008 code. (a) Electronic and nuclear energy loss as a function of ion specific energy. (b) Projected range *versus* ion specific energy. The red lines indicate that Au ions of a specific energy of 11.4 MeV/u have a range of approximately 160 μm.

In this study, the irradiation of PET membranes of thickness ~12 μm is normally performed with a stack of 6 membranes (72 μm). The reason for choosing heavy ions (^{238}U and ^{197}Au) for the irradiation is that the energy loss reaches a high value which makes them ideal for creating continuous etchable tracks. Tracks formed with too little energy deposition are either not etchable at all or etch discontinuously, so that the size distribution of the pores can become too broad. For polymer materials, a minimal energy loss of about 2–5 keV/nm is required [68]. As can be seen in Figure 3.2b, with the ion range of 72 μm, the specific energy of Au ions reduces from 11.4 to approximately 5.8 MeV/u. Within that range of energy, the energy loss is about 14 to 16 keV/nm as depicted in Figure 3.2a, which is sufficiently high to create the homogeneous damage along the whole latent track, leading to a good etchability.

The density of ion tracks in a polymer membrane can be varied from single ion to high fluence. Figure 3.3 shows the scheme for the irradiation of a sample stack of 6 PET membranes with the fluence $5x10^9$ ions/cm^2. The brown area of a circle at the center of polymer indicates the irradiated region. For single-ion irradiation, a metal mask with a centered aperture of diameter d = 300 μm is placed in front of the sample, and is exposed to a defocused ion beam. Therefore, if the ion flux is sufficiently low only one ion at a time passes through the aperture and travels across the sample. The irradiation is stopped by deflecting the ion beam when the first ion is registered by the detector behind the sample, thus avoiding a second ion from reaching the target. For high fluence irradiation, the desired fluence can be achieved either by focusing the incoming ion beam, or increasing the irradiation time during which the target is exposed to the beam with a constant flux.

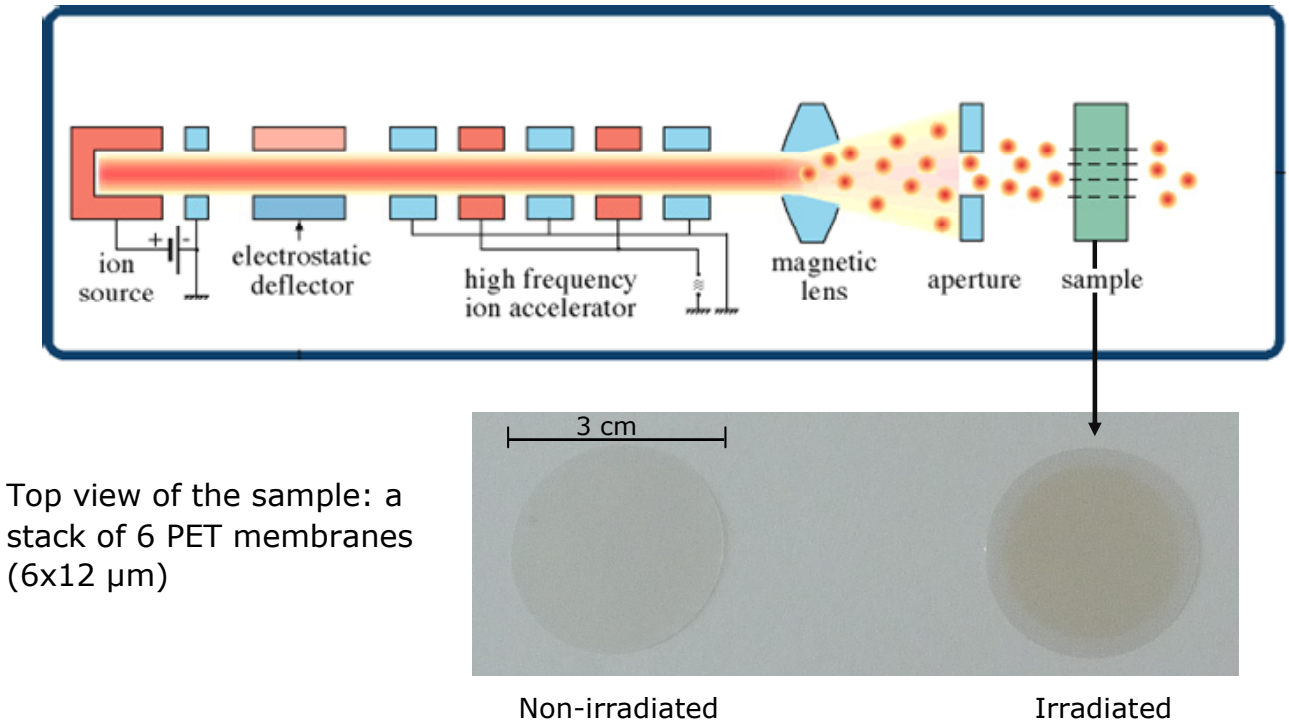

Figure 3.3: Scheme illustrating the irradiation process of polymer material at the UNILAC of GSI, Darmstadt, Germany. The sample diameter is 3 cm.

3.2 Fabrication of nanopores

The transformation of ion tracks into nanopores is obtained by chemical etching. During chemical etching the damaged zone is removed and transformed into a hollow pore. The scheme of the etching process is illustrated in Figure 3.4. This process controls pore size and shape. The pores are formed because the damage material along the ion tracks is removed faster than the (undamaged) bulk material by the chemical etchant. It means that the track-etch rate (v_{track}) is higher than the bulk-etch rate (v_{bulk}). The bulk etch rate depends on the material, on etchant composition and concentration, as well as on temperature. The track etch rate depends on the sensitivity and chemical nature of the material, irradiation conditions, post-irradiation conditions, and also etching conditions. Finally, the pore size is

controlled by the etching time, and the shape of the etched pores could be cylindrical or conical depending on etching the polymer membrane on both sides or on one side, respectively.

In heavy ion-track polymer membranes, the track core is mainly composed of chemically active polymer fragments which then can undergo post-irradiation reactions, such as oxidation, photo-oxidation, etc. For this reason, storage of irradiated polymers in air leads to a significant increase in track etch rate. Additionally, the exposure of UV light to the sample before performing the etching step can also help to sensitize the ion tracks [69]. It is believed that UV light deposits its energy on the ion track and breaks additional chemical bonds, thereby increasing the track-etch rate. Therefore, before the etching process, the polymer foils were treated with UV light (wavelength 320 nm) for 1 h on each side to sensitize the tracks for fast removal of the damaged material.

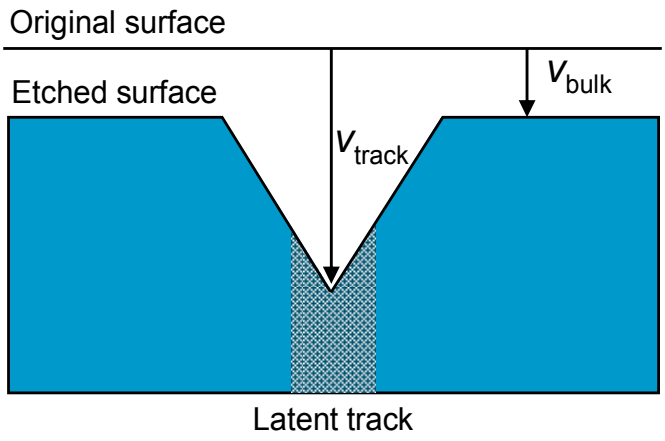

Figure 3.4: Schematic illustration of the etching process of heavy ion tracked polymer membrane with bulk-etch rate (v_{bulk}) and track-etch rate (v_{track}).

3.2.1 Cylindrical nanopores

In this study, the chemical etchant for the fabrication of nanopores in PET membranes is sodium hydroxide (NaOH). The cylindrical nanopores are obtained by etching the track-membranes on both sides. To achieve this, the ion-track membranes (single or multi) are suspended in a double-walled beaker filled with an etching solution (2 M NaOH). The temperature of the etching solution is maintained at 50°C by a circuit of heated water flowing through the double walls of the beaker. In order to stop the etching process, the membranes are taken out of the beaker and are thoroughly washed with distilled water. For further removal of the residual salts, the membranes are additionally immersed in deionized water overnight. The scheme of the fabrication of cylindrical nanopores is shown in Figure 3.5.

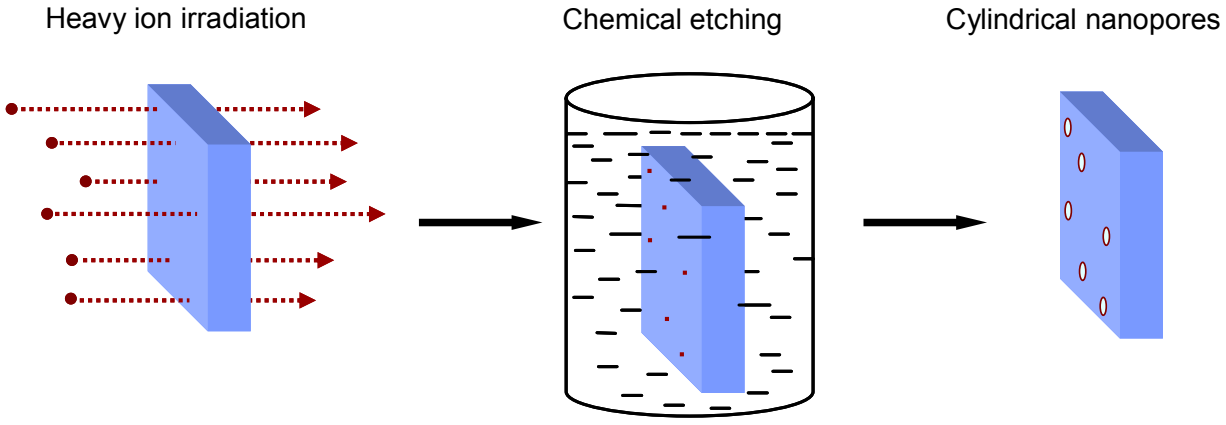

Figure 3.5: Scheme illustrating the fabrication process of cylindrical nanopores in PET membrane.

3.2.2 Conical nanopores

To create a conical pore, the polymer membrane is clamped between the two compartments of a conductivity cell. The principle of the procedure is to perform the etching only from one side of the membrane while the other side is protected by a solution that is able to neutralize the etchant as soon as the pore opens, thus slowing down the etching process. The experimental setup is shown in Figure 3.6a. The etching solution (9 M NaOH) is inserted into one compartment, and the other compartment is filled with a stopping solution containing a mixture of 1 M formic acid (HCOOH) and 1 M potassium chloride (KCl). The stopping solution protects this side from etching, and assures the conical geometry of the resulting nanopore. The etching process is carried out at room temperature. To additionally control the etching, a potential difference of 1 V is applied across the membrane. The voltage is applied in such a way that negatively charged (OH^-) ions of the etchant are drawn out of the pore tip (Figure 3.6b). This is necessary for the fabrication of nanosized pores. The measured current remains zero as long as the pore is not yet etched through. After the break-through, HCOOH neutralizes NaOH to protect the pore tip. The etching process is stopped when the current reached a certain value (Figure 3.6c). Subsequently, the pore is washed first with stopping solution in order to quench the etchant, followed by deionized water. The etched membrane is immersed in deionized water in order to remove the residual salts.

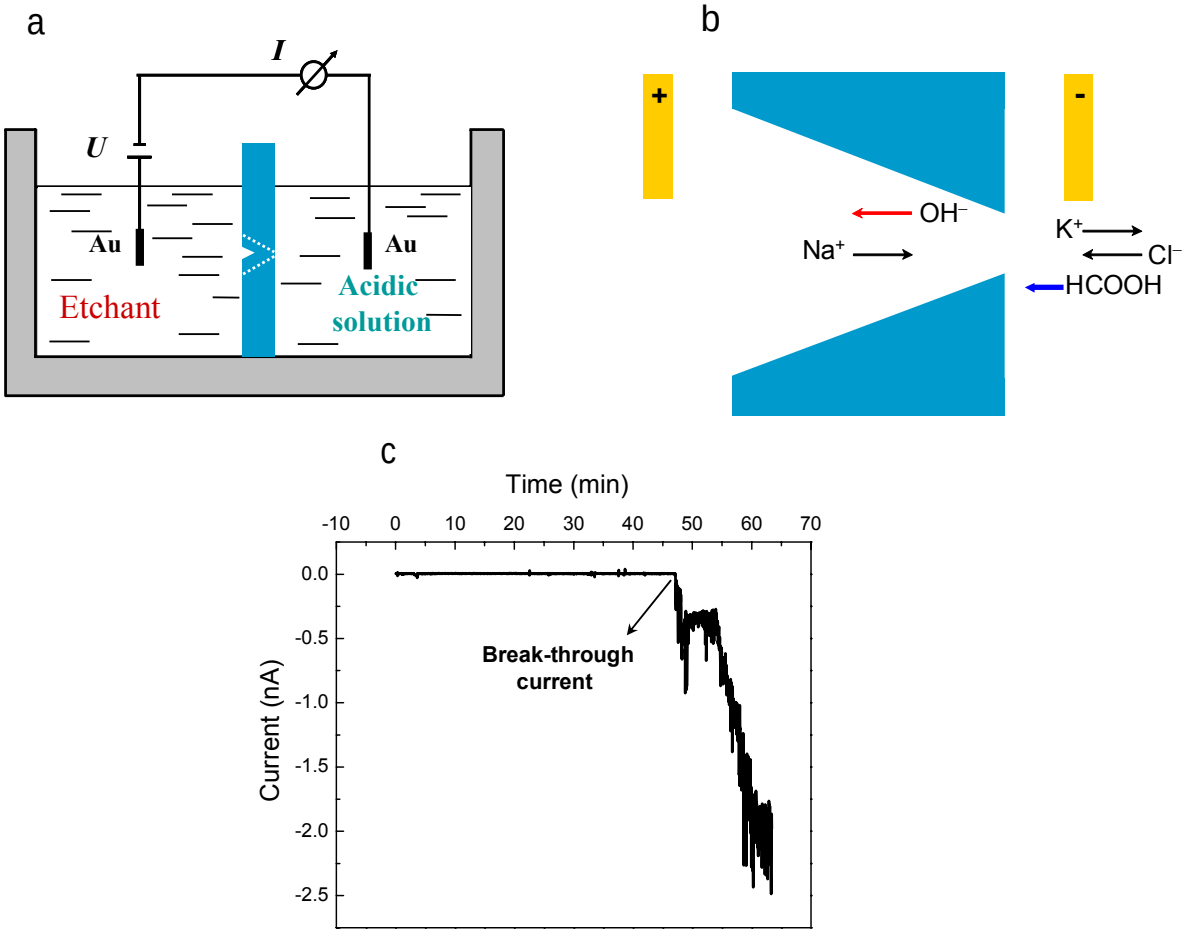

Figure 3.6: Scheme illustrating the asymmetric etching process of a single conical nanopore. (a) The etching setup for fabrication of conical nanopore. (b) Principle of the neutralization between NaOH and a stopping solution (1 M HCOOH + 1 M KCl). (c) The current *versus* time graph to monitor the etching process.

3.3 Characterization of nanopores

For any application or theoretical description of the nanopores, it is very important to know exactly their real shape and dimensions. Some methods are used here to obtain this information. Scanning electron microscopy (SEM) is applied to investigate the effect of UV treatment prior to etching on the pore size distribution by imaging the pore openings on the membrane surface. Replica technique and conductometry are used in combination with SEM to study the geometry of the nanopores and to measure the diameter of the pores.

3.3.1 Scanning electron microscopy

In this study, field emission scanning electron microscopy (FESEM-JEOL JMS-7401F, Japan) is used to investigate the geometrical characterization of the track-etched nanopores, including diameter of the pore opening, shape of the nanopores and pore distribution on the membrane surface. Firstly, the membrane surface containing nanopores is easily viewed by SEM. For this purpose, a piece of etched nanopore membrane was glued on a sample holder and covered with a thin layer of gold (~ 3 nm) by a sputtering machine. This gold layer is necessary to create the conductive surface required for imaging and to avoid the thermal damage of the polymer membrane by the electron beam [70].

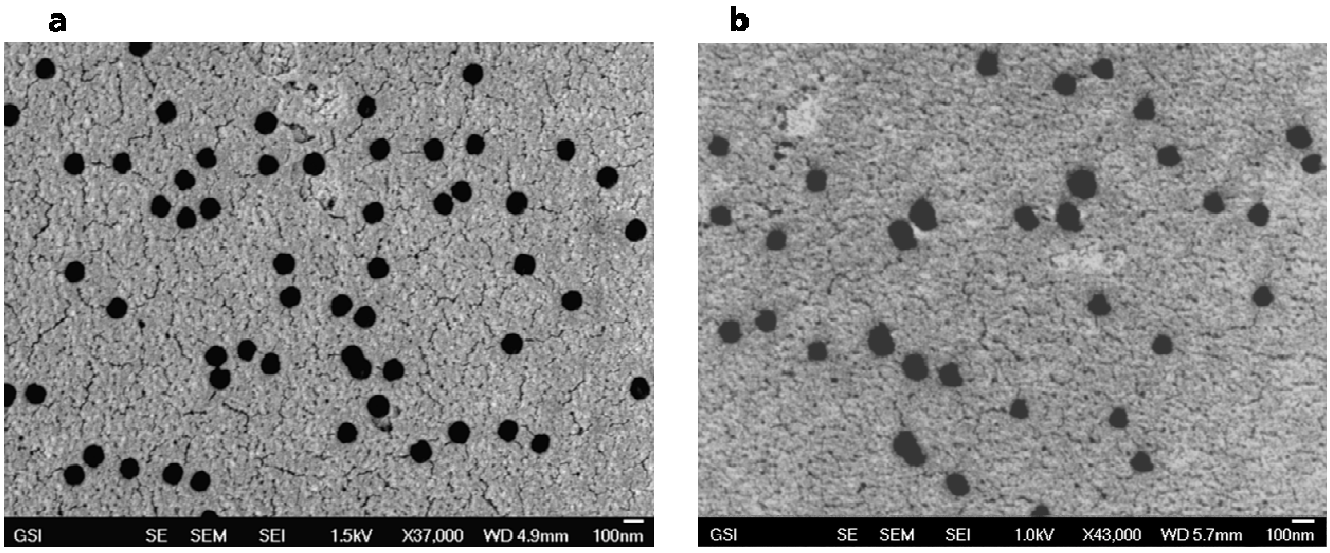

Figure 3.7: FESEM micrographs of track-etched polymer membranes containing cylindrical nanopores with (a) and without (b) UV treatment before the etching process.

As mentioned earlier, one aim of using SEM was to study the effect of UV irradiation on the pore size distribution of track-etched membranes. The irradiation was performed by exposing the sample to UV light for 1 h from each side prior to the etching process. The results for UV treated and non-treated membranes are shown in Figure 3.7. Obviously, two positive effects were attained by UV irradiation. One is that the pore openings are more circular and the other is that the membrane treated with UV shows narrower pore size distribution. The influence of UV irradiation on track-etched nanopores in PC was also well studied previously and showed the same effects [71]. A narrow pore size distribution is definitely of importance for applications using nanoporous membranes for separation.

3.3.2 Replica technique

Combined with SEM method, the replica technique gives insight about the internal geometry of the track-etched nanopores. This was achieved by galvanic filling of the pores with metal (Au), followed by removing the polymer by chemical dissolution. The shape of the nanopores could be visualized with the FESEM images of Au wires. This technique was used for membranes containing multi-nanopores (both cylindrical and conical).

Preparation of nanowires

Nanowires were fabricated using the ion track template electrodeposition method. Figure 3.8 illustrates the procedure of nanowire deposition. Firstly, the track-membranes were chemically etched to produce nanopores. Prior to electrodeposition of nanowires, a thin Au layer of ~ 50 nm thick is sputtered on one side of the track-etched membrane and reinforced electrochemically by copper (Cu). This Au/Cu layer serves afterwards as a cathode for nanowire deposition in an electrochemical cell. A bar of Au metal immersed in a sulphite-based gold electrolyte (Au-SF) serves as an anode for the deposition of nanowires. During deposition, the temperature is controlled at a value of ~ 50°C and a constant voltage of 0.7 V is applied. The deposition is stopped when a sharp increase of the measured current is observed.

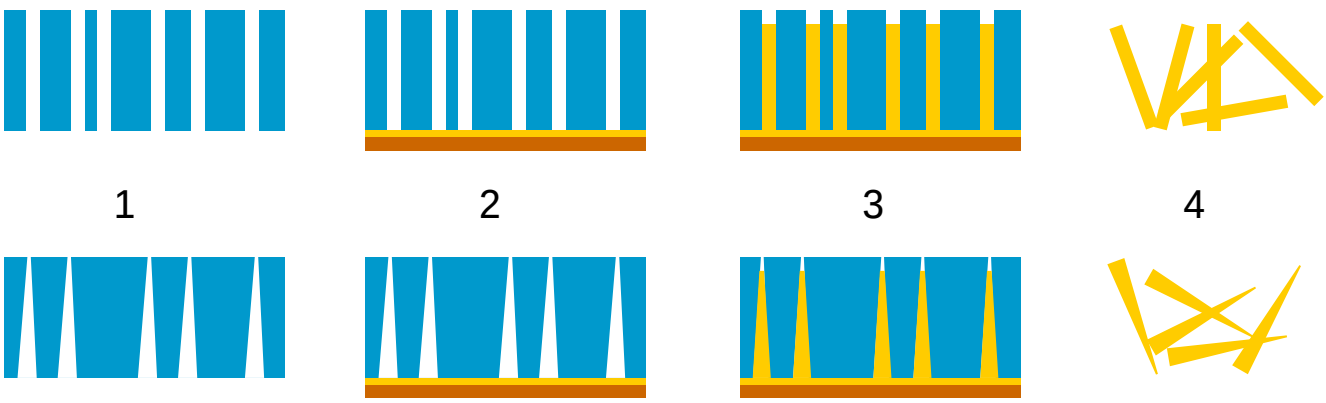

Figure 3.8: Template deposition of Au nanowires in track-etched PET membranes containing cylindrical and conical nanopores. (1) Track-etched nanopores. (2) Formation of Au/Cu cathode. (3) The deposition of Au nanowires. (4) The dissolution of polymer template to expose Au nanowires.

After the wire deposition, the template is dissolved by immersing the membrane in 4 M NaOH solution at 50 °C overnight. The nanowires are then investigated with the FESEM. Figure 3.9 shows FESEM images of cylindrical and conical gold nanowires after removing the polymer templates. It is worth noting that in the case of the conical nanowires, the membrane containing 10^7 tracks/cm^2 was etched via asymmetric technique. In addition, the Au/Cu layer, serving as a cathode for the electrochemical deposition of the nanowires, is deposited on the big opening side of membrane containing conical nanopores.

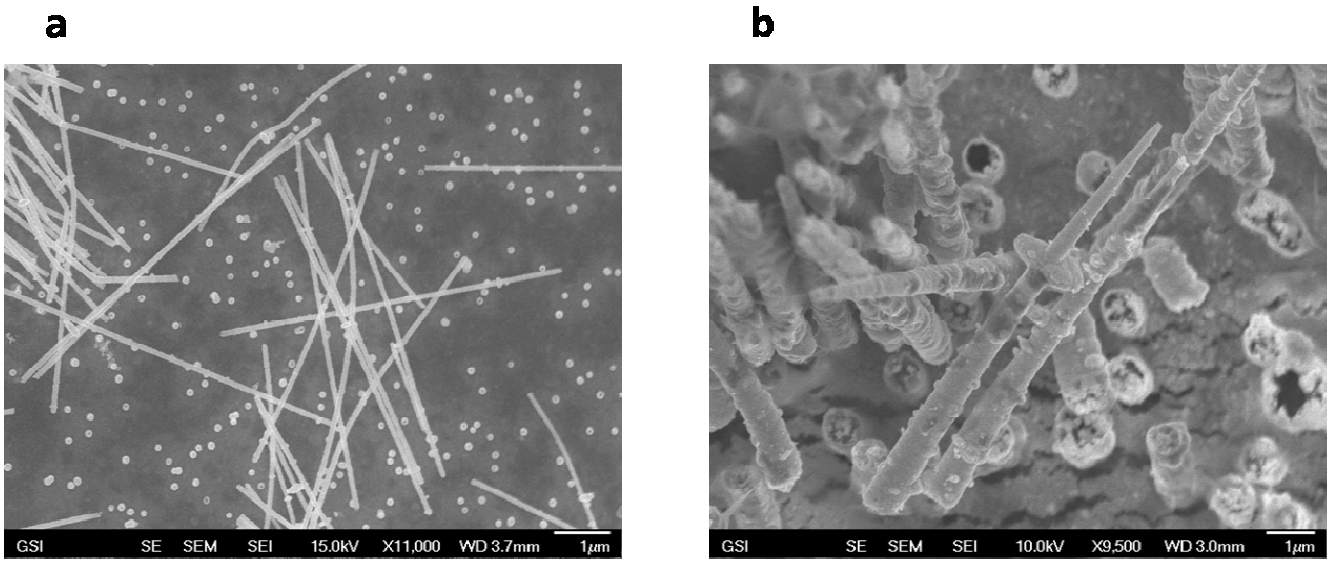

Figure 3.9: FESEM images of Au nanowires fabricated in track-etched PET membranes containing (a) cylindrical nanopores and (b) conical nanopores.

3.3.3 Conductometry measurement

By assuming a certain geometry, the pore diameter can be calculated by using an electrochemical method. After track-etching, a membrane containing a single pore is washed with distilled water and mounted between the two halves of a conductivity cell. An electrolytic solution (1 M KCl) with known conductivity is filled into each half, and Ag/AgCl electrodes are used in order to obtain a current-voltage (*I-V*) curve of the pore.

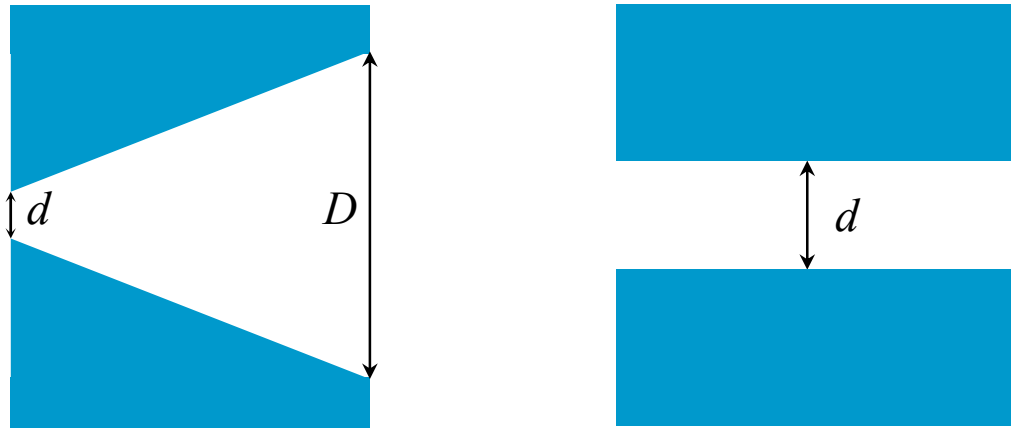

Figure 3.10: Scheme illustrating the geometrical parameters of conical (left) and cylindrical (right) nanopores in polymer membranes.

Cylindrical nanopore

For cylindrical pores, the *I-V* curve is linear, and the slope is a measure of the ionic resistance of the electrolyte-filled pore. The diameter of a cylindrical nanopore is determined by the following relation [71]:

$$d = \sqrt{\frac{4LI}{\pi\kappa V}} \tag{3}$$

where L is the length of the pore, which could be approximated to the thickness of the membrane; d is the diameter of the pore; κ is the specific conductivity of the electrolyte (11.377 S/m for 1 M KCl at 26 °C), V is the voltage applied across the membrane, and I is the measured current.

Conical nanopore

This method can also be used for the estimation of the small tip opening, with diameter d, of a conical nanopore. For the calculation of tip opening diameter, the equation has to be slightly modified by taking into account the conical geometry with a different diameter on each side [48]:

$$d = \frac{4LI}{\pi\kappa VD} \tag{4}$$

The large opening with so-called base diameter (D) of a conical pore was determined independently by FESEM, using a sample containing 10^7 pores/cm^2, which was etched simultaneously with the single-pore membrane under the same conditions.

3.4 Functionalization of nanopores

PET membranes are produced by the condensation of terephthalic acid and ethylene glycol to form ester bonds. In the chemical etching process of ion-track membranes, these ester bonds are the main points for the chemical attack of an etchant (NaOH). The alkali easily hydrolyses these bonds in the polymer chains. Therefore, during the process of alkaline etching, these weak bonds are broken into terminated carboxyl (–COOH) and hydroxyl (–OH) groups, as shown in Figure 3.11. The surface chemistry of nanopore walls containing carboxyl moieties can be manipulated by covalent attachment of a variety of functional groups. The chemical functionalization of these carboxyl groups was achieved via *N*-(3-dimethyl-aminopropyl)-*N*-ethylcarbodiimide hydrochloride (EDC)/pentafluorophenol (PFP) coupling chemistry [6]. The reaction scheme is given in Figure 3.12. The first step was the activation of carboxyl groups into pentafluorophenyl ester. A membrane having single (or multi-) nanopores was mounted between the two halves of the conductivity cell. An ethanol solution, containing a mixture of 0.1M EDC and 0.2 M PFP was filled in both halves of the cell. The activation was carried out for 60 minutes at room temperature. Then, these reactive esters were further reacted with molecules having primary amine (–NH_2) groups through the formation of covalent bonds. In this study, the amine-terminated molecules used for the functionlization are: ethylene diamine (EDA), polyethyleneimine (PEI), propylamine (PA) and 3-aminophenylboronic acid (APBA). In each case, an ethanol solution of

0.1 M of reacting molecules was placed on both sides of the membrane for an overnight period. Finally, the functionalized membranes were washed several times with ethanol followed by deionized water.

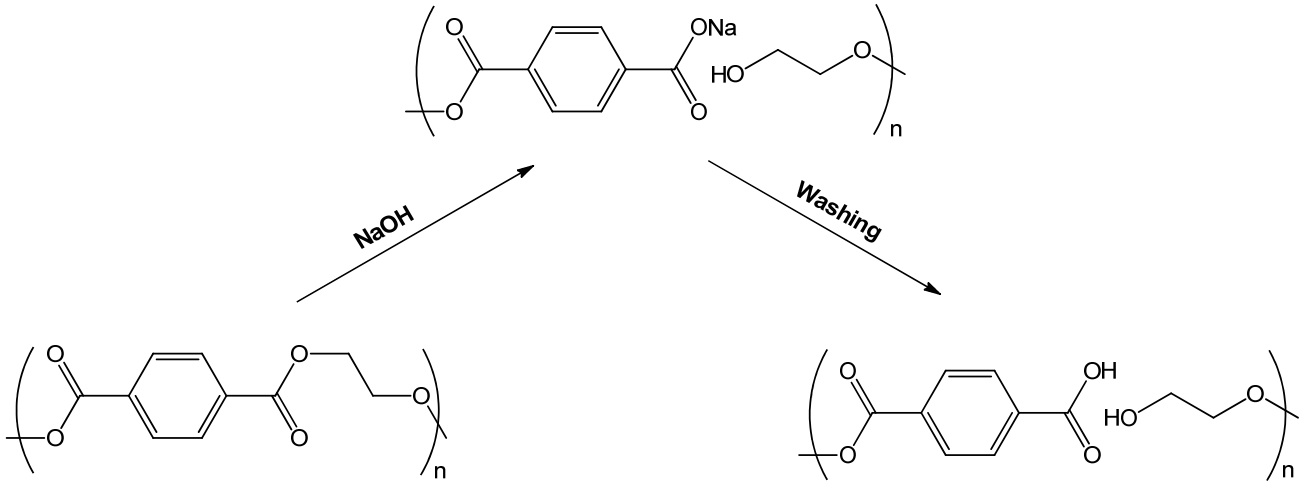

Figure 3.11: Chemical etching of an ion-track PET membrane in aqueous NaOH solution.

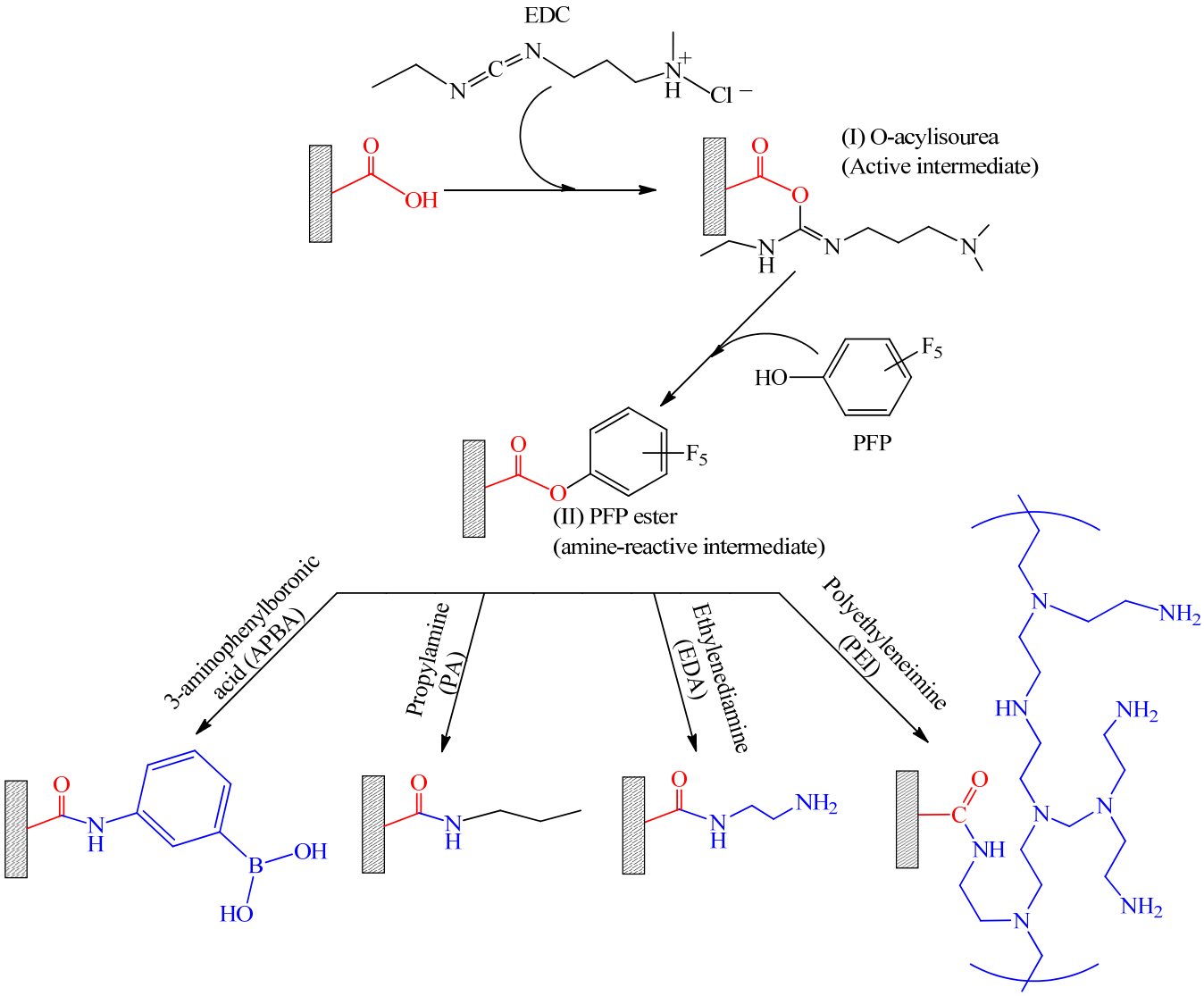

Figure 3.12: Reaction scheme of pore surface carboxyl groups with terminated amino groups by carbodiimide coupling chemistry.

3.5 Mass-transport experiments

Unmodified and modified membranes were used for the transport of charged organic molecules and biomolecules. The analyte molecules were dissolved in phosphate buffer (10 mM, pH 6.5) solution. For the transport experiments, membranes were mounted between the two halves of the conductivity cell (see Figure 3.13). Each half-cell volume was 3.4 ml with an effective permeation area of the membrane of 1.15 cm^2. The feed half-cell was filled with the buffer solution containing a known concentration of an analyte, whereas the permeate half-cell was filled with pure buffer solution. Both solutions were continuously stirred during the whole process. Due to difference in concentration of analyte in the two halves, the analytes from the feed cell tend to diffuse through the membrane to the permeate cell. After a preset time, the concentration of analyte in the permeate half-cell was determined by measuring the UV absorbance with a UNICAM UV/vis spectrometer.

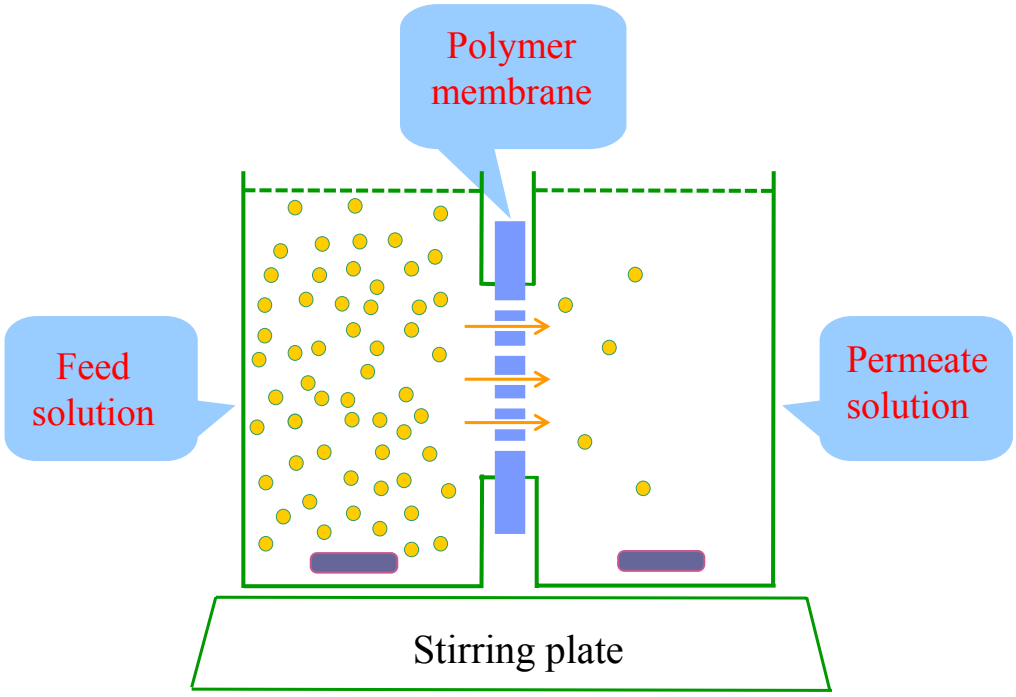

Figure 3.13: Schematic illustration of the diffusion of charged analyte through a nanoporous polymer membrane.

Figure 3.14 presents an example of concentration measurement for an analyte. Methyl viologen (MV^{2+}) has a maximum UV absorption in aqueous solution at a wavelength 258 nm. In the first step, different known concentrations of MV^{2+} in the same buffer solution for transport experiments were measured with UV spectrometer (Figure 3.14a). Then the absorption values at λ_{max} were extracted from the UV data and their linear relation with analyte concentration was established (Figure 3.14b). During transport experiments, the analyte concentration was calculated from this calibration curve according to the observed UV absorption of the analyte solution.

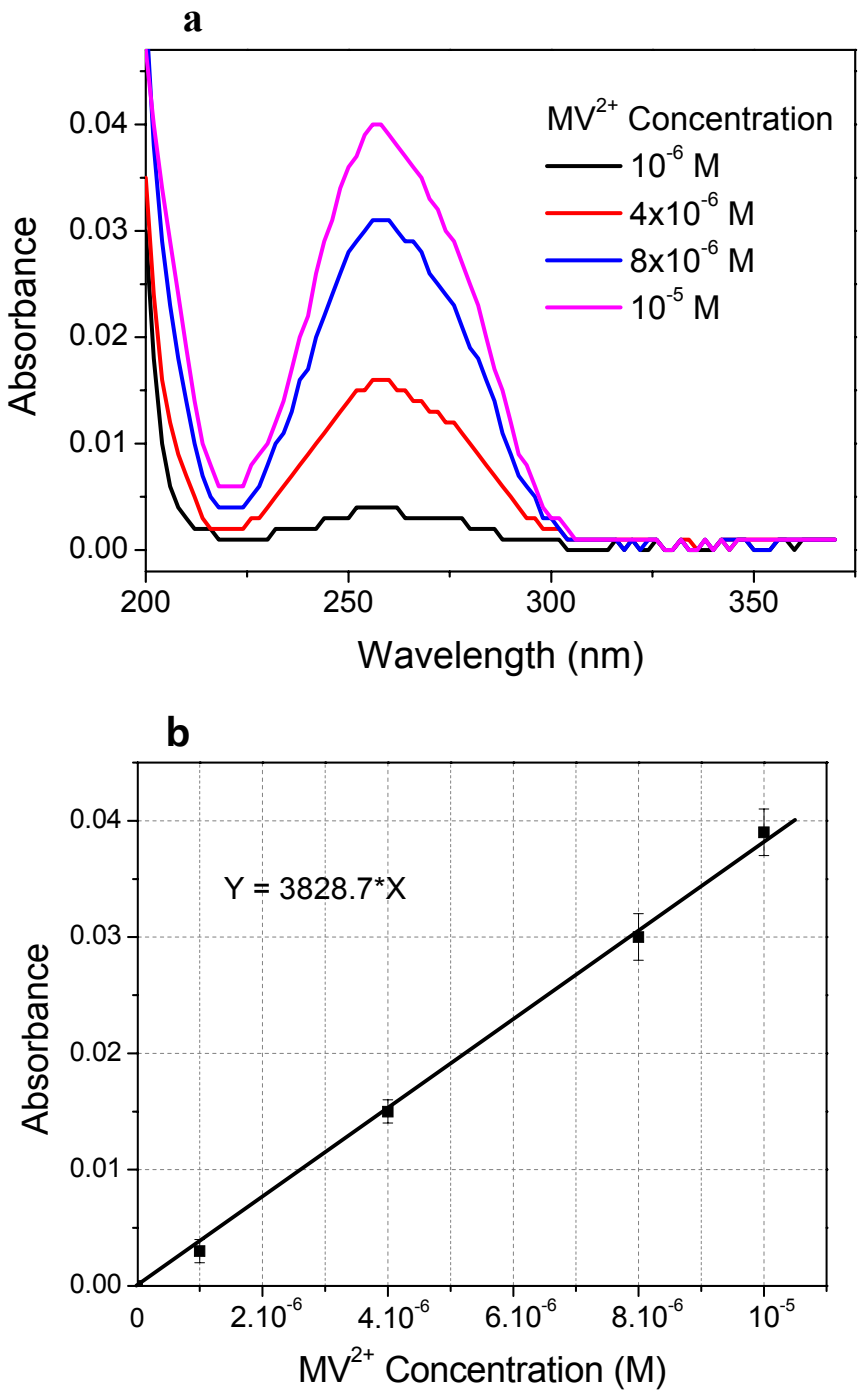

Figure 3.14: (a) UV-spectra of MV^{2+} at different concentrations; (b) the relation between absorption values and analyte concentrations.

3.6 Current-voltage measurements

For measurements of experimental current-voltage (*I-V*) curves, the membrane containing a single nanopore (conical or cylindrical) was mounted between the two halves of the conductivity cell, and both halves of the cell were filled with electrolyte solutions (1 M or 0.1 M KCl). The pH of the electrolyte was adjusted by dilute hydrochloric acid (HCl) or potassium hydroxide (KOH) solutions. A Ag/AgCl electrode was placed into each half-cell solution, and the Keithley 6487 picoammeter/voltage source

(Keithley Instruments, Cleveland, OH) was used to apply the desired transmembrane voltage. To measure the resulting ion current flowing through the pore, a scanning triangle voltage with steps of 100 mV from -2*V* to +2*V* was applied. By introducing a delay time of at least 1 second between each step, the system could be assumed to be in equilibrium all the time. It is noted that in the *I-V* curve measurements of a single conical pore, the base side of the pore remained connected to the ground electrode. Figure 3.15 gives an example of *I-V* measurement for a single cylindrical pore and the corresponding *I-V* curve.

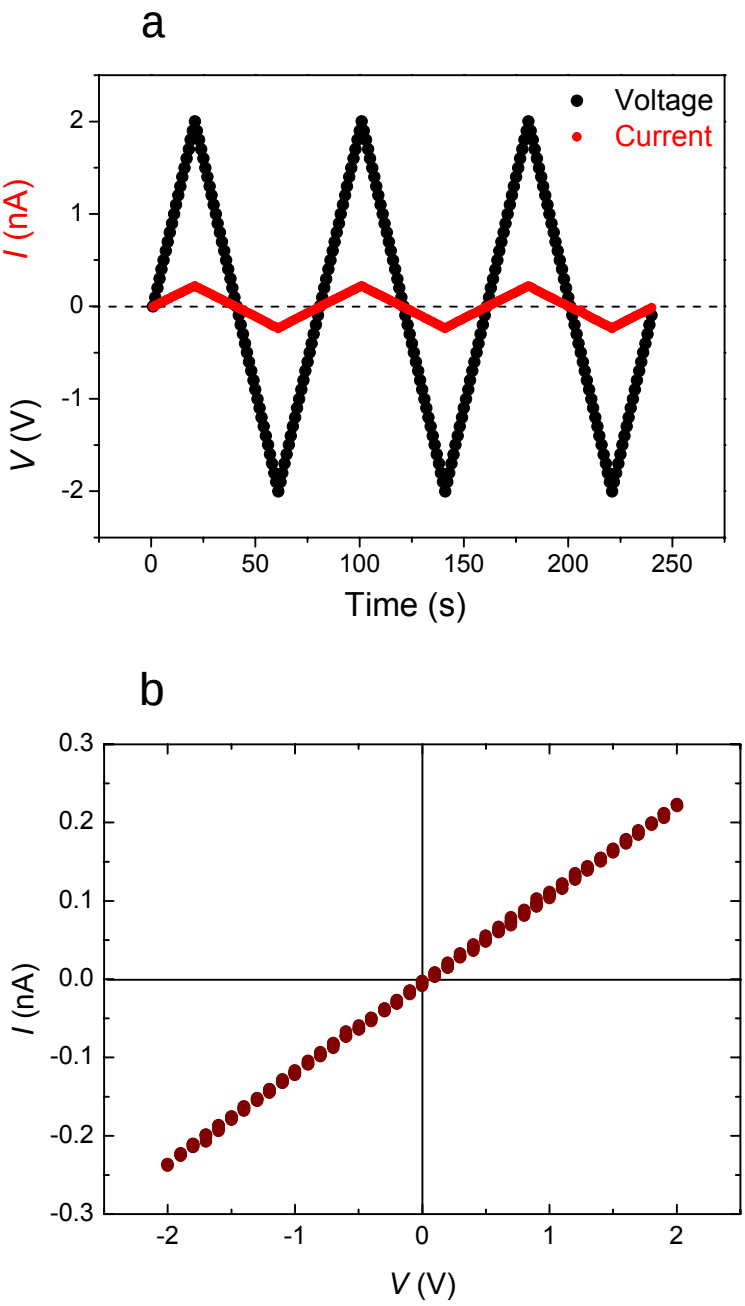

Figure 3.15: (a) An example of *I-V* measurement in a cylindrical nanopore: triangle sweeps of voltage (black) and measured current (red). (b) Corresponding *I-V* curve.

4 Results and discussion

4.1 Geometric characterization of nanopores

4.1.1 Cylindrical nanopores

The cylindrical nanopores in PET were fabricated by etching the ion-track membrane on both sides using aqueous 2 M NaOH solution at 50°C. After washing with deionized water, the nanopores were filled galvanically with Au by electrochemical deposition method (section 3.3.2). An FESEM image of the Au nanowires after dissolving the polymer is shown in Figure 4.1(a). The shape of the nanowires represents exactly the geometry of the nanopores. The SEM image shows that the nanowires are cylindrical, i.e. they have the same diameter throughout the wire. This means that the corresponding geometry of nanopores is also cylindrical. The cylindrical geometry is formed because the etching rate along the ion track is considerably higher than the bulk etching rate of the polymer. Figure 4.1(b) presents the diameter of gold nanowires (corresponding to the nanopore diameter) as a function of the etching time. We found a linear relation between the etching time and pore diameter in the time range of this study. For each data point, about 50 nanowires were measured. From the slope of the linear fit, an etching rate of 5.4 ± 0.4 nm·min^{-1} was extracted. For small pores ($d < 20$ nm), the diameter is estimated from the etching rate at a certain etching time. It should be mentioned that very small pore diameters can not be obtained, because a certain minimum time for etching through the membrane is required.

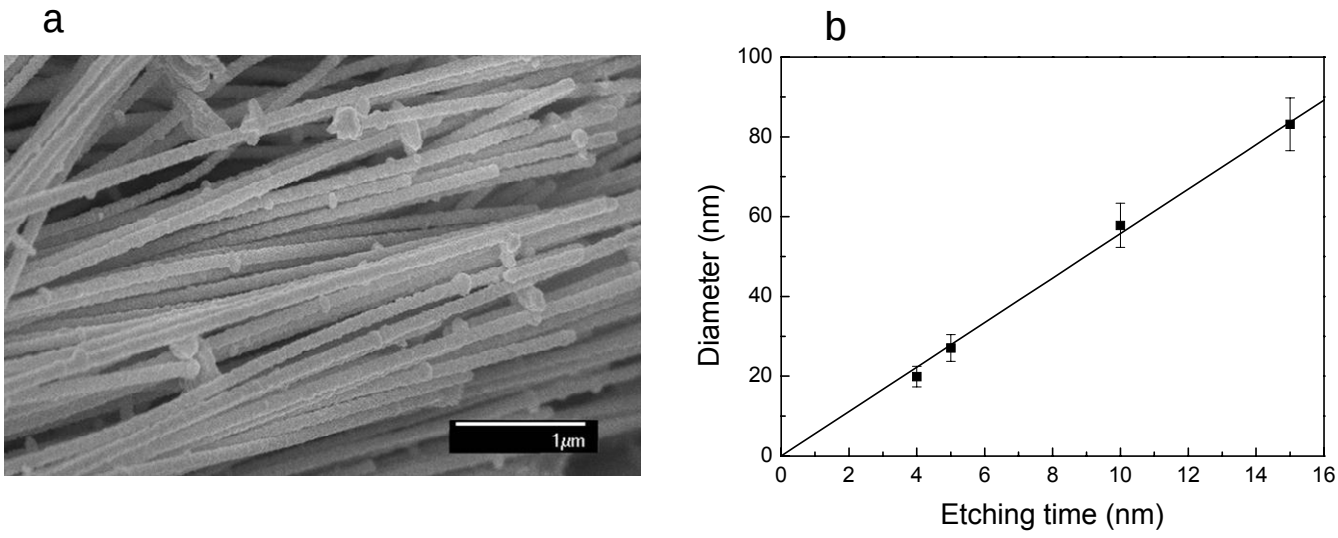

Figure 4.1: (a) FESEM image of gold nanowires deposited in a track-etched PET template. (b) Nanowire (nanopore) diameter as a function of etching time.

4.1.2 Conical nanopores

Single conical nanopores in PET membranes were fabricated by etching the ion-track membranes only from one side (see 3.2.2). For the characterization of pore geometry and diameter, a membrane containing 10^7 tracks/cm^2 was etched simultaneously under the same condition as that of a single track membrane. By galvanic filling the pores with Au and dissolving the polymer by chemical dissolution, the shape of the conical nanopores could be visualized with the SEM. Figure 4.2a shows a FESEM image of a nanowire of conical shape, revealing the conical shape of nanopore. The nanopore contains a large opening at one end (base) and a small opening at the other end (tip).

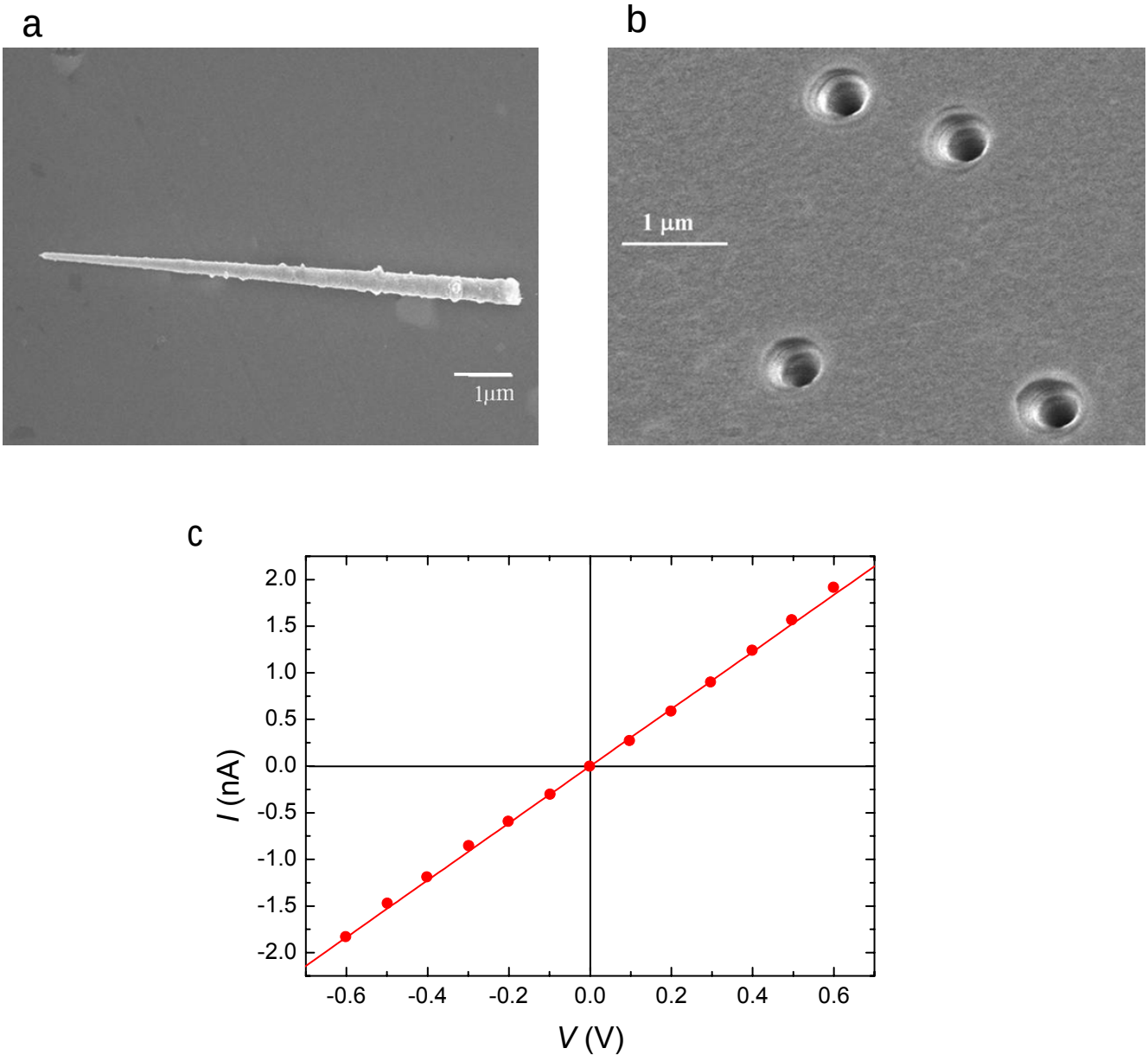

Figure 4.2: (a) FESEM image of a gold nanowire electrochemically deposited in the nanopore which exhibits the conical shape of the nanopore. (b) FESEM image of base openings of conical nanopores in PET membrane containing 10^7 pores/cm^2. (c) A typical *I-V* curve of a single conical nanopore measured in 1 M KCl electrolyte solution at pH 3.

The size of the base opening of nanopores was estimated by FESEM images of the etched membrane surface. Figure 4.2b shows an image of a polymer sample on the side of the big openings having a base diameter (D) of ~530 nm. Since the tip is too small to be imaged by SEM, its diameter was estimated from the conductivity measurement, according to Eq. (4). The *I-V* curve of the corresponding single conical nanopore in 1 M KCl solution at pH 3 is shown in Figure 4.2c. From the plot, the slope of the linear *I-V* relation was extracted which gives a value (I/V) of approximately 3.1. Together with the value of the base diameter ($D \sim 530$ nm), the calculated tip diameter (d) according to Eq. (4) is ~ 8.0 nm.

4.2 Selective transport of analytes through cylindrical nanopores

The fabrication of nanopores was achieved by first irradiating PET membranes with energetic ions followed by selective chemical etching of the ion tracks. This ion track technology has opened up the possibilities of control over: (1) the pore areal densities by adjusting the number of ions penetrating through the membrane, (2) pore size (diameter down to a few nanometers) and geometries (various shapes, e.g. cylindrical, conical or biconical), and (3) tailoring the surface properties at will by the use of functionalities (carboxyl groups), generated during track-etching for desired applications such as biosensors [51, 72, 73] and nanofluidic ionic diodes [74]. However, most of the applications have been applied by using single conical nanopores. For nanoporous membranes, Au-coated nanopores in polycarbonate (PC) have been widely used for the transport control of molecules across the pores. Up to now, a variety of methods to control the surface properties of nanopores in PC have been published. Firstly, Martin and co-workers developed a strategy for tuning the surface properties and opening diameter of track-etched pores in polymer membranes. Their method is based on the electroless deposition of a gold layer on the pore walls, followed by the chemisorption of thiols bearing variable functionalities [75-77]. The gold nanotubes embedded in the polymer membranes have been successfully implemented for the charge- or size-dependent molecular transport and separation of drug enantiomers [78, 79]. Chun and Stroeve have demonstrated that the self-assembled monolayers of functional molecules on these nanotubes can be used for the pH-responsive transport of ions and protein analytes through nanoporous membranes [80].

Later on, Thayumanavan and co-workers developed a straightforward strategy to control both surface charge properties and effective diameter of pores in polymer membranes. In this methodology, the nanopore coating was achieved by first adsorption of Sn^{2+} ions on the inner walls followed by the chemical attachment of selected polymer molecules having the desired size and polarity. These modified membranes have been used for the separation and discrimination of small organic and protein molecules based on their charge, size and hydrophobicity [81].

In this framework, it is highly desirable to develop and design alternative strategies enabling the facile control over pore surface charge by directly exploiting the already existing chemical functionalities on the inner walls. In this study, nanopores fabricated in polyethylene terephthalate (PET) membranes possess carboxylic ($-COOH$) groups, generated during the track-etching process. At neutral and basic pH, due to the presence of ionized $-COO^-$ groups, the nanopores are negatively charged. The surface charge was reversed by direct covalent modification of $-COOH$ groups with primary amine ($-NH_2$) groups via carbodiimide coupling chemistry. The aminated nanopores are positively charged due to the protonated ammonium groups ($-NH_3^+$). These pores were successfully studied for the charge-selective transport of organic as well as protein molecules across the membrane.

4.2.1 Permeation of charged organic molecules

The transport experiments for organic molecules were performed with methyviologen (MV^{2+}) and 1,5-naphthalene disulfonate (NDS^{2-}). Their molecular structures are shown in Figure 4.3. For the experiments, phosphate buffer (10 mM, pH 6.5) was used as an electrolyte solution. Each analyte with 10 mM concentration was prepared in the buffer solution. The detail of the experiment was explained in Section 3.5.

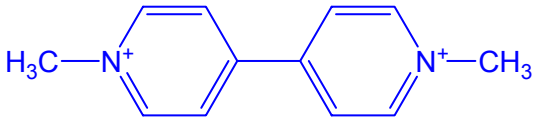

Methylviologen (MV^{2+})

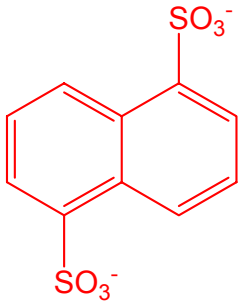

1,5-naphthalene disulfonate (NDS^{2-})

Figure 4.3: Chemical structure of organic analytes studied in mass transport experiments.

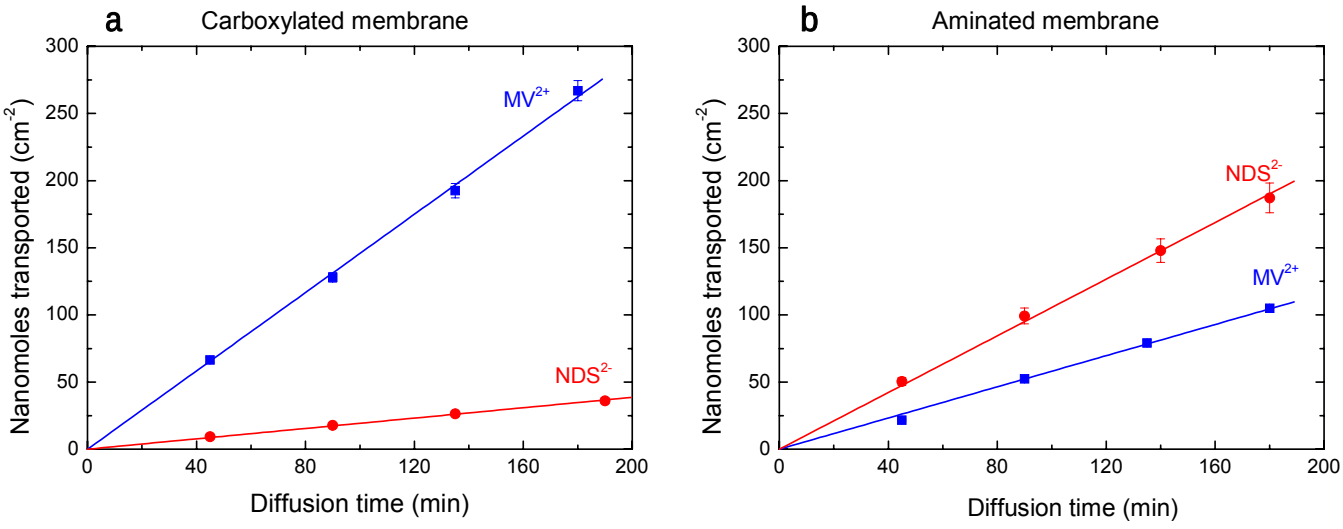

Figure 4.4: Diffusion of MV^{2+} and NDS^{2-} through pores with diameter 20 nm: (a) prior to and (b) after modification with EDA in membranes possessing 3×10^8 pores cm^{-2}.

The transport of analytes was first performed with a track-etched membrane (carboxylated membrane) prior to any further chemical treatment. Then, the membrane was modified with ethylene diamine (EDA) and used again for the transport experiments. The permeation flux of charged analytes (MV^{2+} and NDS^{2-}) across the membrane with areal density 3×10^8 pores cm^{-2} having diameter of ~20 nm is shown in Figure 4.4. The flux reveals the number of moles of the charged molecules transported through the membrane per unit time and is obtained from the slope of these plots. It was observed that in a carboxylated membrane, positively charged analyte (MV^{2+}) has higher flux as compared to that of negatively charged (NDS^{2-}) analyte. In contrast, EDA-modified membrane (aminated membrane) selectively transported the negatively charged analytes (NDS^{2-}). It means that the permselectivity was reversed after modification with amine groups.

It must be noted that in these experiments there is no electric field applied across the membrane. This means that the transport of molecules across the membrane is not governed by electro-osmosis or electrophoresis but only due to the molecular diffusion from the feed cell to the permeate cell. Therefore, in this case the major mechanisms governing the mass transport through nanopores are: (a) volume exclusion, (b) hydrophobic interactions, and (c) electrostatic interactions [82]. In our system, MV^{2+} and NDS^{2-} have quite similar molecular volumes of 0.637 and 0.680 nm^3, respectively [77]. Furthermore, the molecular structures of MV^{2+} and NDS^{2-} both contain two benzyl rings which determine their same hydrophobic behavior within the nanopores. Therefore, the volume exclusion and hydrophobic interaction mechanisms can be neglected in this case. Hence, in our system, the pores were selectively affecting ion permeation via electrostatic interactions. In aqueous solution, the functional amine or carboxyl groups on the pore walls are electrically charged due to protonation or deprotonation, respectively. As mentioned above, this charge spurs the formation of an EDL inside the pore, which contains a higher concentration of counter-ions than of co-ions. At a large distance from the surface, the pore walls therefore seem neutral. However, if the diameter of a pore is comparable to the thickness of the electrical double layer, solute ions passing through the pore interact with fixed surface charges. For this reason, charged nanoporous membranes selectively transport ions with charge opposite to that of the fixed ions on the pore walls, while co-ions are prohibited electrostatically from entering the nanopore [31, 83]. A scheme of the selective transport is shown in Figure 4.5.

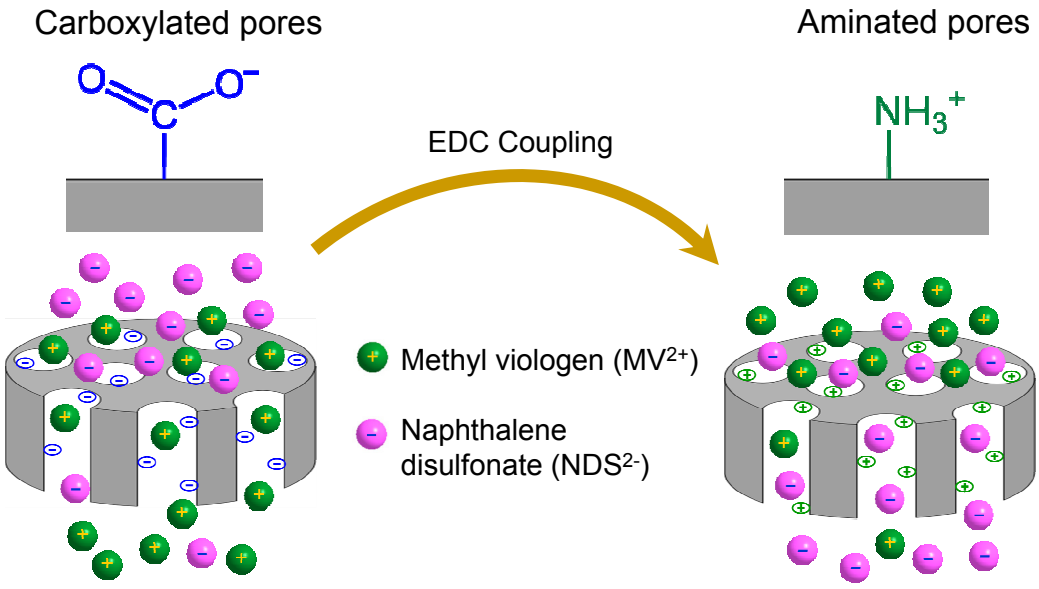

Figure 4.5: Schematic illustration of permselective ionic transport through cylindrical nanopores across the membrane.

The track-etched PET membranes have an isoelectric point (*pI* 3.8) [84], so that at neutral pH, ionized carboxylate ($-COO^-$) anions import negative charges to the walls of the nanopores. Therefore, the carboxylated multipore membrane only allows the selective transport of positively charged (MV^{2+}) molecules and rejects negatively charged NDS^{2-} molecules. During the chemical modification, carboxyl groups were converted into terminated amino ($-NH_2$) groups. At neutral pH, these terminated amino groups import positive charge to the pore surface. As a result, the modified pores favor the permeation of negatively charged (NDS^{2-}) molecules.

For the quantification of the permselectivity of the membrane, the selectivity coefficients (α) are defined as the ratio of the high and low flux values:

for an unmodified membrane:

$$\alpha_{MV/NDS} = \frac{flux(MV^{2+})}{flux(NDS^{2-})} \tag{5}$$

for a modified membrane:

$$\alpha_{NDS/MV} = \frac{flux(NDS^{2-})}{flux(MV^{2+})} \tag{6}$$

As a result from Figure 4.4, the selectivity coefficients for carboxylated and aminated membranes are 7.7 and 1.8, respectively. Although the aminated membrane is anion permselective, the selectivity coefficient is much smaller than that of the carboxylated membrane which is cation permselective, suggesting that the functionalization was not complete, or the amino groups are not fully protonated at pH = 6.5. Consequently, there was still a certain amount of carboxylic groups remaining unmodified on the pore surface which allowed MV^{2+} to diffuse across the membrane. However, this problem can be solved by incorporating the highly charged polymer polyethyleneimine (PEI) via EDC/PFP coupling chemistry. For comparison, the surface chemistry of the pore wall with EDA and PEI incorporated is given in Figure 4.6. To see how the incorporated PEI affected the transport properties of the membrane, the EDA and PEI modified membranes with the same fluence ($7x10^8$ pores cm^{-2}) and pore diameter (~20 nm) were exploited for the mass transport experiments.

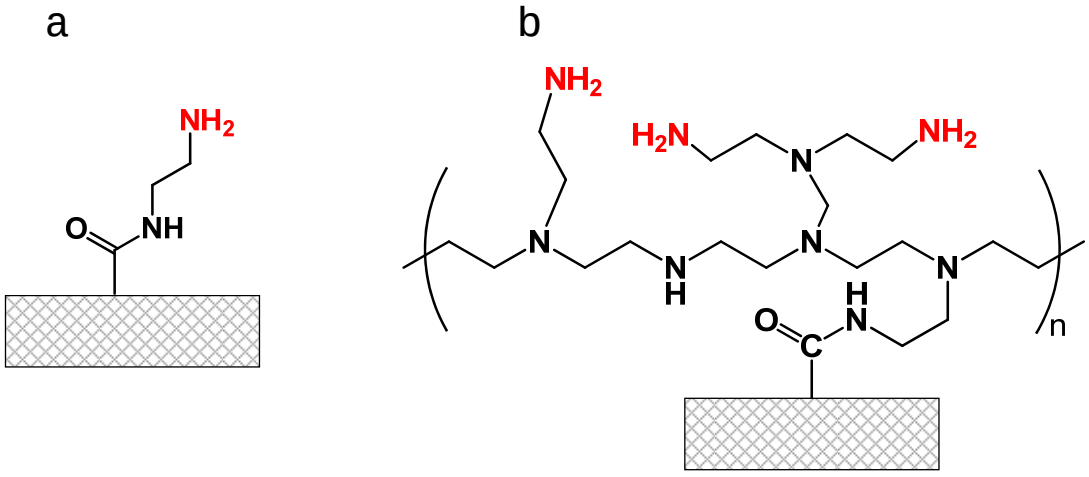

Figure 4.6 Scheme illustrating the surface chemistry of the pore wall after the modification with (a) ethylene diamine and (b) polyethyleneimine molecules.

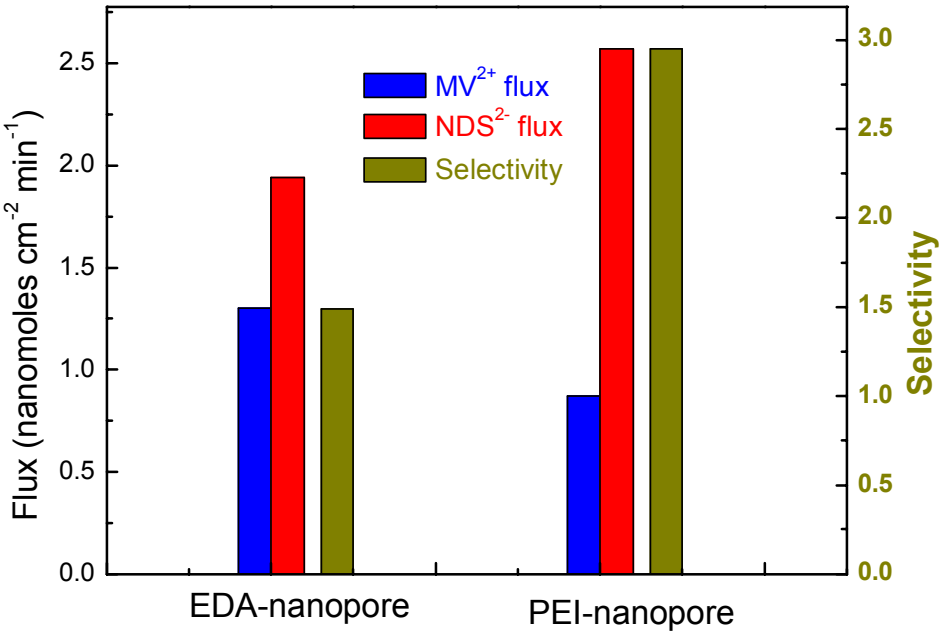

Figure 4.7: Flux data of MV^{2+} and NDS^{2-} and the selectivity coefficient in EDA- and PEI-nanopores ($d \sim$ 20 nm) through membranes containing $7x10^8$ pores cm^{-2}.

The results presenting the permeation data of analyte flux in EDA-modified and PEI-modified nanopores are shown in Figure 4.7. As expected, at neutral pH, both membranes containing positively charged (amino group) pores are anion-selective, showing the flux of NDS^{2-} is higher than that of MV^{2+}. However, there are dramatic differences between EDA- and PEI-nanopores. As compared to EDA-nanopore, PEI-nanopore shows an increase in NDS^{2-} flux and a decrease in MV^{2+} flux. Consequently, the selectivity (ratio of NDS^{2-} flux over MV^{2+} flux) is enhanced by a factor of 2 (from 1.5 to 3). The results indicated that the incorporation of PEI onto the pore walls increases the density of positive charges on the walls, enhancing the anion-selectivity of the membrane.

4.2.2 Permeation of biomolecules

Efficient biomolecule separation is crucial for biomedical applications. The transport and separation of proteins have been studied in thin alumina membranes [85] and gold coated nanopores embedded in PC membranes [86]. In our case, a track-etched membrane with pore diameter ~ 75 nm and density 3×10^8 pores cm^{-2} was used for selective transport of protein molecules such as lysozyme and bovine serum albumin (BSA). In the transport experiments, protein analytes at a concentration of 10^{-4} M were prepared in 10 mM phosphate buffer pH 6.5. The moles transported across the carboxylated membrane vs. time are plotted in Figure 4.8 (top). It was observed that the flux of lysozyme was higher than that of BSA. Here, in addition to electric charges, hydrophobic interactions as well as molecular size of protein analytes also influence the permeation significantly [26, 87]. Moon *et al.* proved that the surface covered with lysozyme is more hydrophobic than the surface clad with BSA [88], whereas $-COO^-$ groups make the surface hydrophilic. In principle, BSA (more hydrophilic) has a stronger interaction with the surface than lysozyme, which should result in higher flux of BSA. However, in phosphate buffer saline at pH 6.5,

BSA (isoelectric point *pI* 4.7) is negatively charged, and lysozyme (*pI* 11.0) is positively charged. This brings electrostatic interactions into play, so that BSA is rejected by the $-COO^-$ groups while lysozyme can pass through the pore. Regarding the volume exclusion mechanism, due to the higher molecular weight of BSA (66 kDa) compared to that of lysozyme (14.7 kDa), the hydrodynamic radii of BSA and lysozyme are 3.8 nm [89] and 1.8 nm [90], respectively. As a consequence, the lysozyme molecules can move more freely in the nanopores which, when regarded separately, would lead to higher flux of lysozyme.

The flux of BSA and lysozyme after modification of the membrane with EDA, in the course of which the surface charge was switched from negative ($-COO-$) to positive ($-NH_3^+$), is shown in Figure 4.8 (bottom). The BSA flux is higher than that of lysozyme, although BSA has a larger hydrodynamic diameter. Here, positively charged lysozyme molecules are repelled from the positively charged pores. Furthermore, since BSA is more hydrophilic than lysozyme, it is more strongly attracted by the hydrophilic nanopores. Therefore, in this case the electrostatic and hydrophobic/hydrophilic interactions between electrically charged biomolecules and the nanopore walls are more prominent than molecular size effects. The calculated selectivity for the 75 nm sized pores in a carboxylated membrane was $\alpha_{Lys/BSA} = 2.36$, while in the aminated membrane, where BSA has a higher flux than lysozyme (0.014 compared to 0.01 nmol cm^{-2} min^{-1}), the selectivity was calculated as $\alpha_{BSA/Lys} = 1.44$.

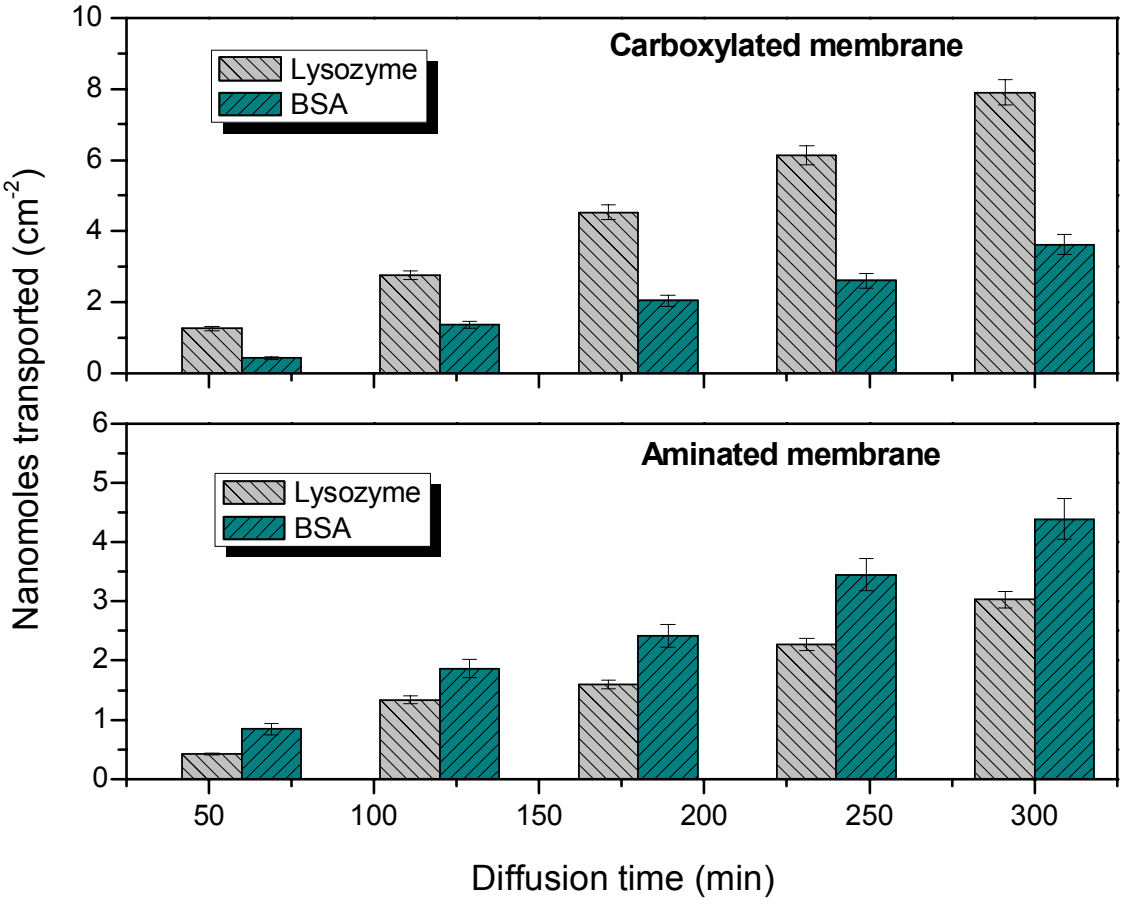

Figure 4.8: Diffusion of BSA and lysozyme at pH 6.5 before (a) and after (b) modification with EDA through pores of ~ 75 nm diameter, pore density ~ $3x10^8$ cm^{-2}.

The role of surface charge on the permselective transport of proteins across the membrane can be further approved by studying the mass transport of proteins with similar molecular weights. Bovine serum albumin (BSA, 66 kDa) and bovine hemoglobin (BHb, 65 kDa) are chosen because they are close in size (~ 1.01 times molecular weight difference). The *pI* of BSA and BHb are 4.7 and 7.0, respectively. In the transport experiments, pH of buffer solutions was adjusted to 6.0. At this pH value, BSA is negatively charged and BHb is positively charged, in accordance to their isoelectric points. Figure 4.9 depicts the diffusion results of these two proteins in ~ 50-nm carboxylated pores with the density of $5x10^9$ cm^{-2}. It shows that only BHb can pass through the membrane while there is no observed flux of BSA. The surface charge obviously governs the biomolecule transport in this case. Both BSA and pore are negatively charged and repel each other, whereas positively charged BHb is easily transported through the pores via electrostatic interactions. As a result, only BHb molecules are able to pass through the pores. Therefore, it can be concluded that track-etched nanopores in PET have great potential in separation of similar-sized proteins with different charges.

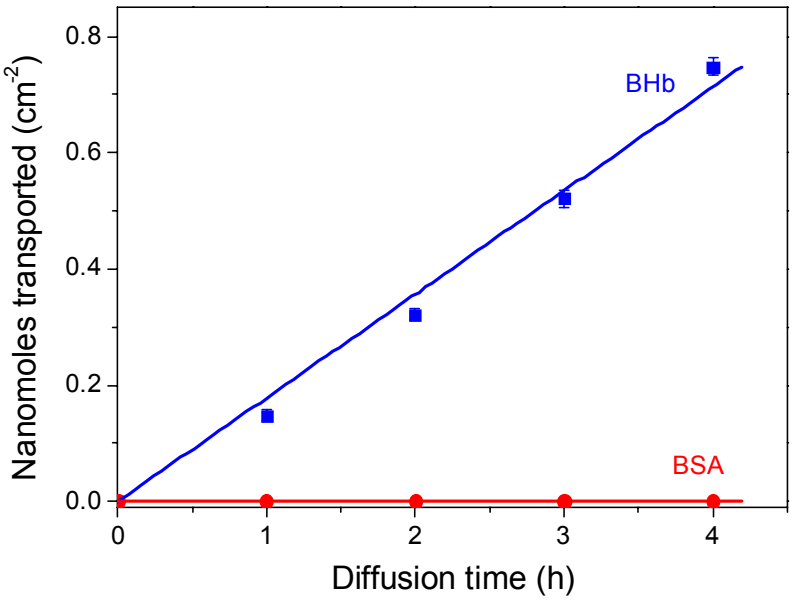

Figure 4.9: Diffusion of BSA and BHb at pH 6.0 in carboxylated nanopores of ~ 50 nm, pore density ~ $5x10^9$ cm^{-2}.

4.3 Estimation of surface charge density in cylindrical nanopores (*)

In order to elucidate the permselective properties of charged nanopores, it is important to know the fixed charge density on the inner surface of the pore. Surface charge is one of the most important properties of nanopores since it governs ion transport through the pores, especially when the salt concentration is low. As mentioned in the previous chapters, track-etched nanopores in PET membranes possess carboxylic groups on their surface. The negative charge density depends on pH through the chemical equilibrium between protonated carboxylic and deprotonated carboxylate groups. It is also affected by many parameters such as polymer chemical structure, the conditions of irradiation (heavy ion, energy), and etching conditions. Therefore, it is very important to determine the concentration of fixed charges in the nanopores fabricated under these conditions in this study.

In this section, a theoretical model based on the Poisson and Nernst-Planck (PNP) equations is used to describe the ionic transport through a single cylindrical nanopore. This model has been successfully used to study the ionic transport through charged conical nanopores [91-94]. By using a minimum number of free parameters, the model was used to study the *I-V* curves of conical nanopore systems and calculate the profiles of average ionic concentration and electric potential along the pore. Detailed theoretical and experimental data have also been provided to investigate the role of the electrostatic interactions responsible for the permselectivity, ionic conduction and rectification properties of conical nanopores [92]. In this study, this model is used for the case of single cylindrical nanopores. Previously, this model was applied to a system where we assumed that the functional (–COOH) groups are uncharged at pH 3 and negatively charged at pH 7. Here, the model has been extended by taking into account the presence of H^+ and OH^- ions in the solutions to describe the ionic transport across a nanopore within a wide range of pH conditions. The extended model is very useful not only for the estimation of surface charge density at a certain pH but also for the determination of pK_a value and the total concentration of carboxylic groups inside the pore.

4.3.1 Theory

Figure 4.10 shows schematically a polymer sample containing a single cylindrical nanopore of radius a, which separates two electrolyte KCl solutions. The pore has a length of l which extends from $x = 0$ to $x = l$. In order to control the pH of the external solutions, either HCl or KOH is added to the electrolyte solution. Therefore, the ionic mobile species in the system are the salt ions (K^+, Cl^-), and the hydrogen (H^+) and hydroxide (OH^-) ions. $c_{S,k}$ and pH_k express, respectively, the KCl concentration and the pH value in solution k ($k = L$ for the left solution and $k = R$ for the right solution). The pore is assumed to be long and narrow, $l >> a$. The external solutions are assumed to be perfectly stirred, and the whole system is considered to be isothermal and at steady state. Also, $c_{i,k}$ and ϕ_k refer, respectively, to the concentration of the species i ($i = K^+$, H^+, Cl^- and OH^-) and the dimensionless electric potential in the bulk of the external solution k. $c_i(x)$ and $\phi(x)$ are the local concentration of the species i and the local dimensionless electric potential within the pore. $\Delta\phi_L = \phi(0) - \phi_L$ and $\Delta\phi_R = \phi_R - \phi(l)$ denote, respectively, the dimensionless Donnan potential drops through the left and right interfaces, and $\Delta\phi = \phi(l) - \phi(0)$ is the dimensionless potential drop within the pore. Finally, V is the applied potential difference, and I is the total electric current passing through the nanopore across the membrane.

(*) The theoretical model and calculations included in this section are provided by Prof. Patricio Ramírez from the Polytechnic University of Valencia, Spain

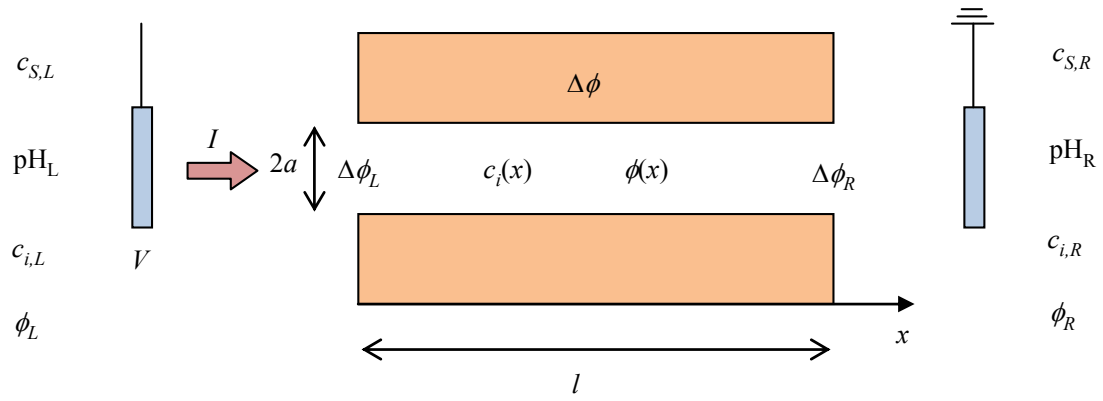

Figure 4.10: Schematic illustration of a cylindrical nanopore used in the model.

This model relies on the application of three basic equations to describe the ionic transport through the nanopore [91]. Those equations are:

the 1D Nernst-Planck equation

$$\vec{J}_i = -D_i(\nabla c_i + z_i c_i \nabla \phi), \tag{7}$$

the Poisson equation

$$\nabla^2 \phi = -\frac{F^2}{\varepsilon R T} \sum_i z_i c_i, \tag{8}$$

and the continuity equation

$$\nabla . \vec{J}_i = 0, \tag{9}$$

where $\vec{J}_i$, D_i and z_i are, respectively, ionic flux, diffusion coefficient and charge number of ionic species i, and ε is the dielectric permittivity of the solution within the pore. Also, R is the gas constant, T is the absolute temperature and F is the Faraday constant.

In order to solve the equations (7)-(9), some approximations have to be introduced. Because the pore is long and narrow ($l >> a$), we assume that ionic fluxes have only an axial component. Therefore, equation (7) then becomes

$$J_i = -D_i\left(\frac{dc_i}{dx} + z_i c_i \frac{d\varphi}{dx}\right). \tag{10}$$

When the two surrounding chemical solutions are identical, the concentration of mobile charge c_i is constant inside the pore. The equation (10) can be written in the form

$$J_i = -z_i D_i c_i \frac{d\phi}{dx}. \tag{11}$$

Since c_i is constant along the pore Eq. (11) can be easily integrated and yields

$$J_i = -z_i D_i c_i \frac{\Delta\phi}{l}. \tag{12}$$

Also, the continuity equation (9) can be written in the form

$$\frac{d}{dx}(\pi a^2 J_i) = 0. \tag{13}$$

As a result of the fabrication process, the pore contains weak acid carboxylic groups. We assume that the neutral (COOH) and dissociated (COO^-) forms of the carboxylic groups are in equilibrium with the H^+ ions of the solution within the pore,

$$-\mathrm{COOH} \underset{}{\overset{K_a}{\rightleftharpoons}} -\mathrm{COO}^- + \mathrm{H}^+, \tag{14}$$

where K_a is the equilibrium constant for the dissociation reaction which has the following relation

$$10^{-pK_a} \equiv K_a = \frac{X_C^N c_{H^+}}{X_C^0}, \tag{15}$$

where X_C^0 and X_C^N are, respectively, the volume concentration of neutral and dissociated forms of the carboxylic groups. The concentration of carboxylic groups, X_{CT}, is given by

$$X_{CT} = X_C^N + X_C^0. \tag{16}$$

Combining equations (15) and (16), the volume fixed charge concentration of the pore yields

$$X_C^N = \frac{X_{CT}}{1 + c_{H^+}/K_a}. \tag{17}$$

The surface density (σ) of ionizable groups is related to the volumic concentration of carboxylic groups through the condition

$$\sigma\, 2\pi a l = F\, X_{CT}\, \pi a^2 l. \tag{18}$$

The concentrations of H^+, OH^-, and in the external solutions are

$$c_{H^+,k} = 10^{-\mathrm{pH_k}}, \; k = L, R, \tag{19}$$

$$c_{OH^-,k} = K_W / c_{H^+,k}, k = L, R, \quad (20)$$

where $K_W = 10^{-14}$ M^2. Assuming the electroneutrality condition in the external solutions, the following relation is obtained:

$$c_{K^+,k} + c_{H^+,k} = c_{Cl^-,k} + c_{OH^-,k}, k = L, R. \quad (21)$$

For $pH_k \leq 7$ ($k = L, R$), HCl is added to the solution, and then Eq. (21) gives

$$c_{K^+,k} = c_{S,k}, k = L, R, \quad (22)$$

$$c_{Cl^-,k} = c_{S,k} + c_{H^+,k} - c_{OH^-,k}, k = L, R. \quad (23)$$

For $pH_k > 7$ ($k = L, R$), KOH is added to the solution, and then Eq. (21) gives

$$c_{Cl^-,k} = c_{S,k}, k = L, R, \quad (24)$$

$$c_{K^+,k} = c_{S,k} - c_{H^+,k} + c_{OH^-,k}, k = L, R. \quad (25)$$

The external and pore ionic concentrations are connected through the Donnan equilibrium conditions at the pore|solution interfaces $x = 0$ and $x = l$

$$c_i(0) = c_{i,L} \exp(-z_i \Delta\phi_L), \quad (26)$$

$$c_i(l) = c_{i,R} \exp(z_i \Delta\phi_R). \quad (27)$$

Combining Eqs. (26) and (27) with the electroneutrality condition inside the pore we obtain

$$\sum_i z_i c_i - X_C^N = 0. \quad (28)$$

In the case of long pores, equation (28) can be used instead of Poisson equation (8) [95].

The following equations are found:

$$\left(1 + \frac{c_{K^+,k}}{c_{H^+,k}}\right) u_k - \frac{X_C^N}{c_{H^+,k}} - \frac{c_{Cl^-,k} + c_{OH^-,k}}{c_{H^+,k}} \frac{1}{u_k} = 0, \quad k = L, R, \quad (29)$$

where $u_L \equiv c_{H^+}(0) / c_{H^+,L}$ and $u_R \equiv c_{H^+}(l) / c_{H^+,R}$. Equation (29) can be solved for u_k using the Newton-Raphson procedure. Once the unknowns u_k have been determined, one can obtain the pore concentrations $c_i(0)$ and $c_i(l)$ as well as the Donnan potential differences $\Delta\phi_L$ and $\Delta\phi_R$ from Eqs. (26) - (28).

Numerical integrating of equations (12) and (13) and taking into account the boundary conditions in equations (26)-(27) provides the ionic fluxes for any applied voltage $V \equiv RT\,(\phi_L - \phi_R) / F$. From the ionic fluxes, the total electric current passing through area cross-section of the nanopore is

$$I = \sum_i z_i F \pi a^2 J_i . \tag{30}$$

As a result, we obtain the following equation for the *I-V* curve:

$$I = \frac{F^2}{RT}\frac{\pi a^2}{l}\left(D_{K^+} c_{K^+} + D_{Cl^-} c_{Cl^-} + D_{H^+} c_{H^+} + D_{OH^-} c_{OH^-} \right) V . \tag{31}$$

4.3.2 Fitting theoretical calculations to experimental results

The experimental data were obtained with PET membranes containing single cylindrical nanopores. The etching process was described in section 3.2.1. For the measurement of *I-V* curves, the membrane was mounted between the two halves of the conductivity cell, and both halves of the cell were filled with 0.1 M KCl solution at certain pH. An Ag/AgCl electrode was placed into each half-cell solution, and the Keithley 6487 picoammeter/voltage source (Keithley Instruments, Cleveland, OH) was used to apply the desired transmembrane potential difference in order to measure the resulting ion current flowing through the pore by applying a scanning triangle voltage from -2V to +2V.

In all cases, the *I-V* curves of the nanopore were measured under symmetric electrolyte KCl solution of concentration $c_{S,L} = c_{S,R} = 0.1$ M. The nanopore sample used for the theoretical calculations had a radius of about 12 nm, which was roughly estimated from conductivity measurement (Eq. 3). The *I-V* curves of the pore are shown in Figure 4.11a for different pH values from 2 to 12. The solution pH was achieved by adding HCl or KOH into the solutions ($pH_L = pH_R = pH$). The plot shows that all curves exhibit linear behaviour due to the symmetric (cylindrical) geometry of the pore though the pore surface is uncharged (low pH) or negatively charged (high pH). The linear *I-V* curve indicates that the absolute values of ion currents at voltages of opposite polarities with the same amplitude are the same.

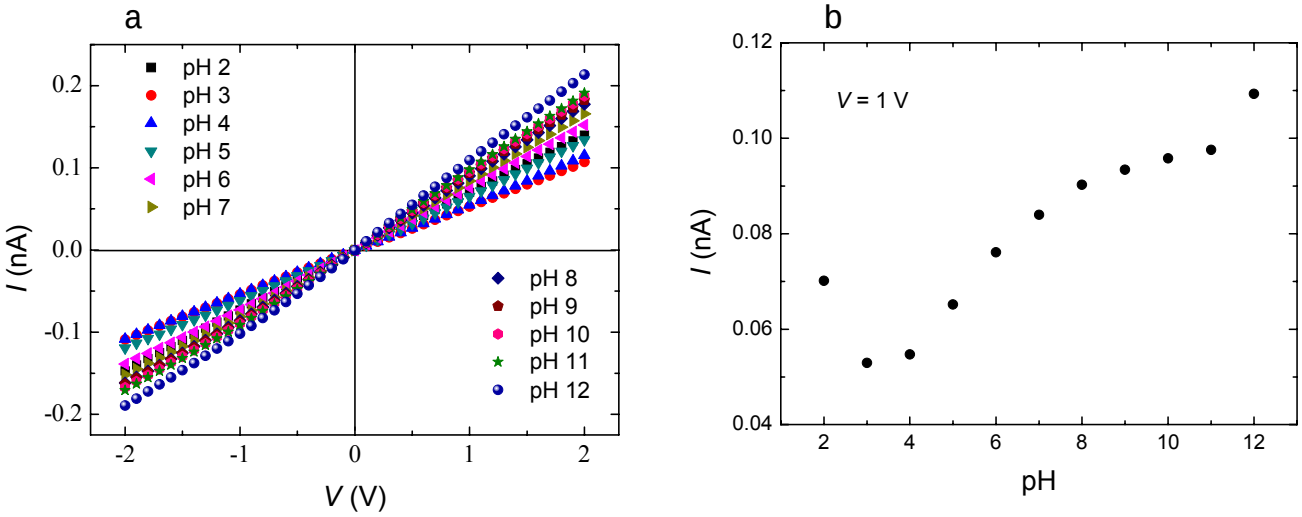

Figure 4.11: (a) Experimental *I-V* curves of the nanopore in 0.1 M KCl at different pH values ($pH_L = pH_R$ pH); (b) Experimental *I*-pH curves of the pore at $V = 1$ V.

In order to visualize the changes in nanopore conductance as a function of pH, it is more convenient to represent the results with *I* vs pH plot at a given voltage (*V*). Figure 4.11b shows a typical s-shaped curve of measured currents obtained at $V = 1$ V. It is noted that the results at different *V* values produce analogue s-shaped curves. Typically, the s-shaped curve shows the increase in current of the pore when pH increases from 3 to 11. This can be explained by the fact that the pore is uncharged at pH = 3-4 and completely negatively charged at pH = 8-11. Therefore, a higher amount of negatively charged groups (–COO^-) would lead to a higher conductivity of the pore (the observed current at certain voltage). It is also observed in the Figure 4.11b that relatively high currents were measured at pH = 2 and pH = 12. It originates from the fact that it was necessary to add high amounts of HCl and KOH to the solution in order to obtain these extreme pH values. As a result, the ionic strength of the solution and the current values both increased dramatically.

For the theoretical calculations, we have used $T = 293$ K and the (infinite dilution) diffusion coefficients $D_{K+} = 1.96\times10^{-5}$ cm^2/s, $D_{Cl-} = 2.03\times10^{-5}$ cm^2/s, $D_{H+} = 9.31\times10^{-5}$ cm^2/s, and $D_{OH-} = 5.28\times10^{-5}$ cm^2/s of the ionic species [96]. The parameters of the model are the total concentration of carboxylic groups X_{CT}, the pore radius (*a)* and the pK_a value of the carboxylic groups. To fit the experimental data, at first, the pore radius was estimated in the limit of the uncharged pore (pH = 3-4). At this pH range, the pore is uncharged due to the protonation of –COOH groups. In this case, $X_C^N = 0$ and the PNP theoretical model described above has only one fitting parameter, the pore radius $a = d/2$ (*d* is pore diameter). The results of experimental *I-V* curve at pH 3 and fitting appear in Figure 4.12a. In the case of the pore used in this study, the theoretically estimated value for *a* is around 11.5 nm.

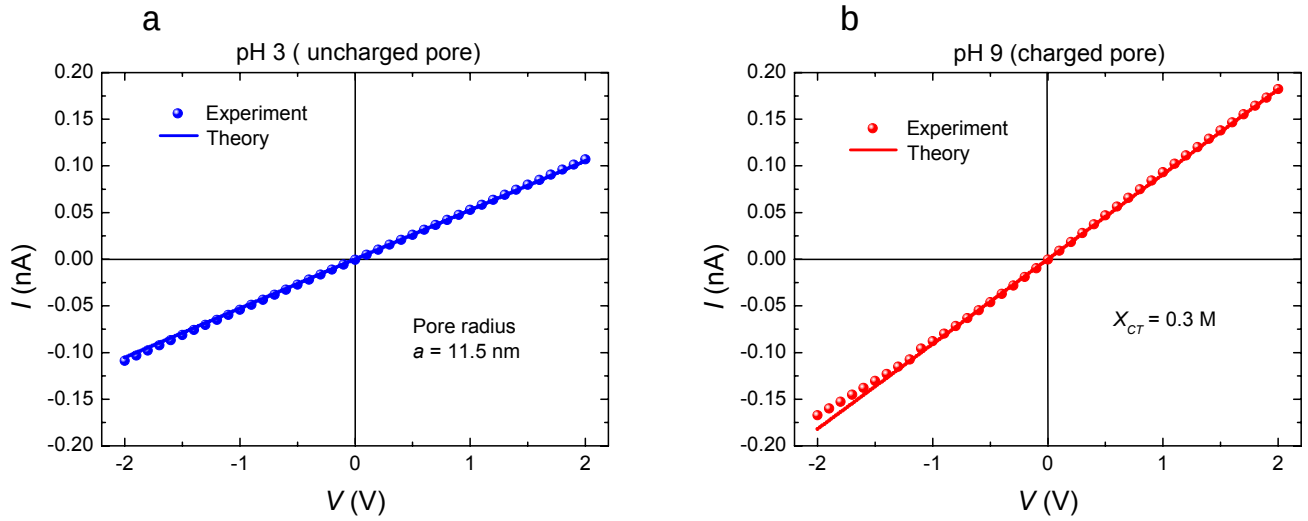

Figure 4.12: Experimental and theoretical *I-V* curves of a nanopore sample. (a) At pH = 3. (b) At pH = 9.

Secondly, the model was fitted to the experiments in the case of 0.1 M KCl at pH = 8-11. In this case, X_{CT} was calculated in the limit of the completely charged pore. Figure 4.12b depicts the experimental and theoretical *I-V* curves at pH = 9. It can be seen that there is only slightly measurable asymmetry in measurements of the current especially at high voltage. This might be due to the fact that the two sides of the original PET foil are not perfectly identical. Also, the inhomogeneity of the polymer foil could lead to the asymmetric geometry of the pore at the beginning of the etching process [97]. From the *I-V* curves, the best fitting value for X_{CT} at pH = 9 is ~ 0.3 M. By applying the results to Eq. (18), the density of fixed charges $\sigma = 1.0e$ nm^{-2} is obtained. Finally the pK_a value was derived from the slope of the transition

region (pH = 4-8) in the *I*-pH plot. The results of the fitting at different voltage appear in Figure 4.13 and the best fitting parameters are given in Table 4.1.

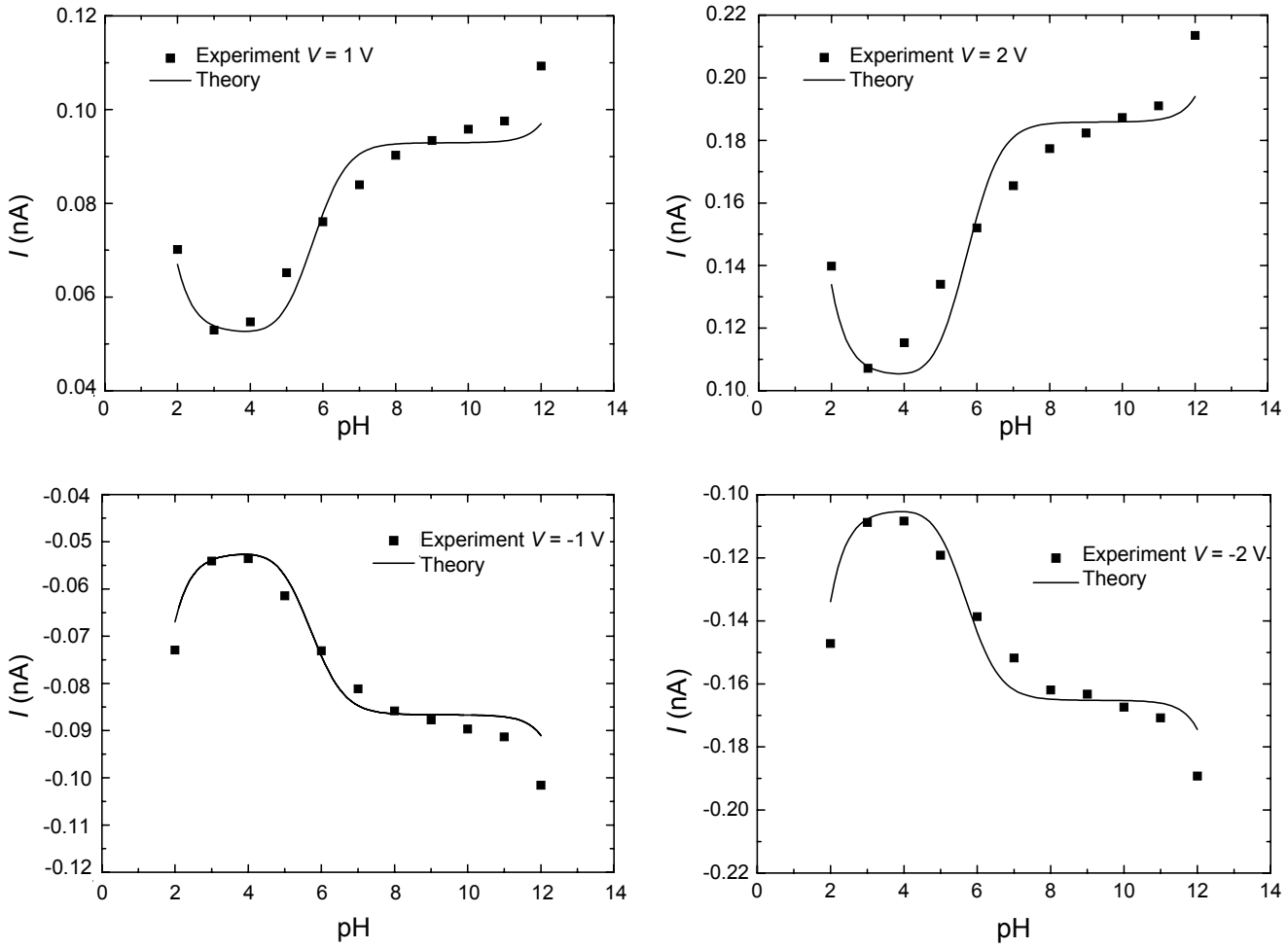

Figure 4.13: Comparison of *I*-pH plots between theory and experiments at different voltages.

Table 4.1: Fitting data at different voltages.

Voltage (V)	X_{CT} (M)	σ (e nm^{-2})	pK_a
-2	0.25	0.87	5.1
-1.5	0.27	0.93	5.1
-1.0	0.27	0.93	5.1
1.0	0.3	1.0	5.1
1.5	0.3	1.0	5.1
2	0.3	1.0	5.1

It is found that the best fitting value of pK_a is about 5.1 in all cases. This is in agreement with the pK_a value of carboxylic groups (pKa = 5.7) recently reported in the literature by measuring streaming potential in cylindrical pores of track-etched PET membranes [98]. We can also see from the Table that at positive voltage, $\sigma = 1.0e$ nm^{-2} is reproducible and at negative voltage $\sigma \sim 0.9e$ nm^{-2} is obtained which

also exhibits reproducible behaviour. The discrepancy in the estimation of charge density at different voltages is not much and this is probably due to the inhomogeneity of the polymer.

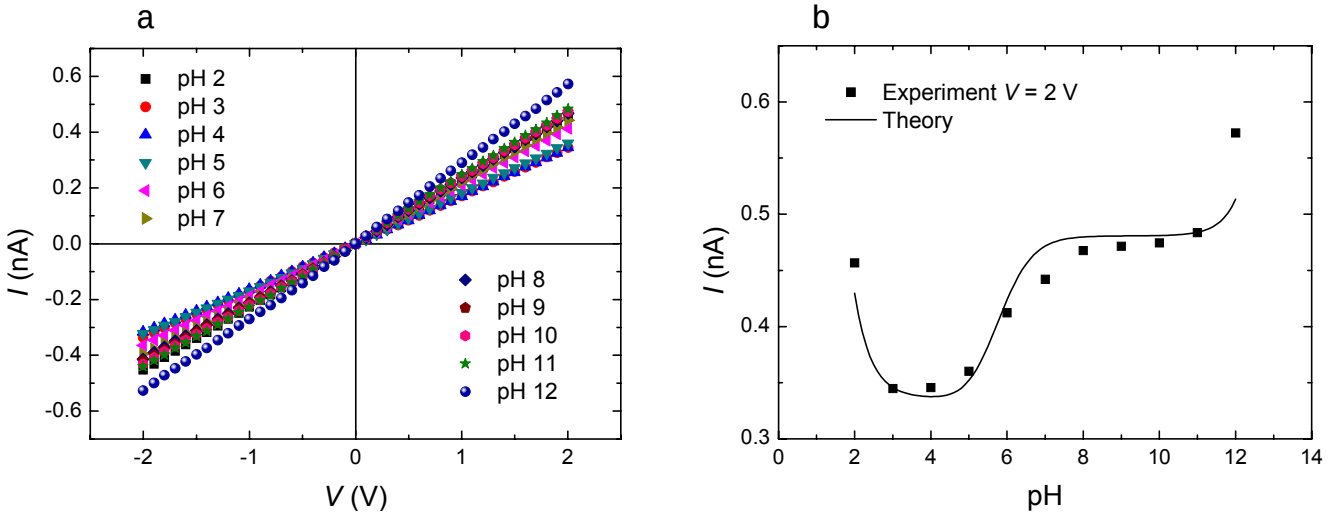

Figure 4.14: (a) Experimental *I-V* curves of the nanopore (a = 22 nm) in 0.1 M KCl at different pH values; (b) Experimental and theoretical *I*-pH curves of the pore at V = 2 V.

To check the reproducibility of the model, the same procedure was applied to another nanopore sample which has an estimated radius of ~ 22 nm. The experimental *I-V* curves in the pH range from 2 to 12 are presented in Figure 4.14a. Firstly, the pore radius of 21 nm was calculated in the limit of the uncharged pore (pH = 3-4). Secondly, in the limit of the completely charged pore (pH = 8-11), the concentration of –COOH groups (X_{CT}) and charge density (σ) were found to be 0.21 M and 1.3e nm^{-2}, respectively. Finally, the pK_a value of 5.2 was obtained from the slope in the transition region (pH = 4-8) in the *I*-pH curve (Figure 4.14b).

In short, it can be concluded that the data show the feasibility of the extended model based PNP equations in estimating the concentration of fixed charges and pK_a value of –COOH groups in cylindrical nanopores in PET. It is necessary to consider the cylindrical nanopores used in the mass transport experiments in the previous section. If the pK_a value of –COOH is 5.15, approximately 96% of COOH groups are deprotonated at pH = 6.5 according to Eq. (15). When the total charge density on the pore walls ranges from 0.9 to 1.3e nm^{-2} and each charge corresponds to one –COOH group, as a result, the charge density on the nanopore surface is ranging from 0.85 to 1.25e nm^{2} at pH = 6.5.

4.4 Factors affecting nanopore transport properties

In the previous section, an experimental demonstration of charge-selective transport of ionic species in nanopores was discussed. The permselectivity of these pores was studied with charged organic analytes and biomolecules. For practical reasons, the nanoporous membranes with high selectivity and high throughput are required for the separation of mixtures of molecules. This would make the separation processes consume less time and provide products of high purity. Therefore, in this part, the effects of pore density, pore diameter, ionic strength of electrolyte solution and applied voltage have been taken into account to find the optimum conditions for the best performance of the membrane.

Most transport phenomena at the nanoscale pores are driven either by electrokinetic flow or surface mediated transport. Thus, the experimental results will first focus exclusively on the diffusion of analyte through the pores by surface mediated transport. Then, by an applied electric field, electrokinetic phenomena occurring in nanopores will also affect the permeation of the analytes across the membrane, resulting in the selectivity and throughput changes of the membrane performance.

4.4.1 Pore areal density

For the application of nanoporous membranes in separation processes, an important issue is to improve the molecular flux through the membrane. Wirtz *et al.* reported that protein flux can be increased by about two orders of magnitude by applying a pressure difference (~ 1.4 atm) across the membrane in order to drive the feed solution [64]. The pores were fabricated in commercial polycarbonate membranes and the maximal pore density was approximately $6x10^8$ pores/cm^{-2}. In this study, the flux of molecules is enhanced by simply increasing the pore areal density in the membrane. Figure 4.15 presents flux data of MV^{2+} and NDS^{2-} at pH 6.5 through carboxylated pores with diameter 20 nm as a function of pore density (3×10^7, 3×10^8 and 7×10^8 pores cm^{-2}). The results indicate that the flux of each analyte was enhanced accordingly by increasing the porosity. As expected, the selective coefficients are almost the same for samples with high and low pore density. The fluxes of the analytes increased about ten-fold by increasing the pore density to a factor of 10 (from 3×10^7 to 3×10^8 pores cm^{-2}). The flux of MV^{2+} can be enhanced up to 3.5 nanomols cm^{-2} min^{-1} (7 x 10^8 pores cm^{-2}) while the selectivity still remains ~10.

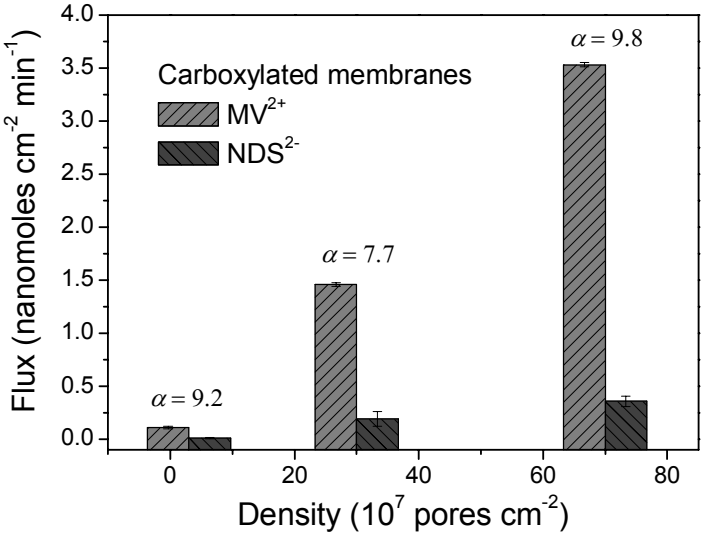

Figure 4.15: Flux data of MV^{2+} and NDS^{2-} at pH 6.5 through carboxylated pores with diameter 20 nm as a function of pore density.

4.4.2 Extension of electrical double layer

The extension of EDL determines how much the EDL occupies the nanopore volume and this can be controlled by manipulation of pore diameter (d) and the Debye length (λ_D). This section deals with the experimental results on the effects of these two parameters to the nanoporous membrane performance. The Debye length can be manipulated by the ionic strength of the electrolyte, and the pore diameter can be easily controlled by the etching time of the track membranes. The scheme presenting the EDL extension and ion distribution inside nanopores is given in Figure 4.16 and can be understood as follows:

a. If we keep the λ_D constant and change the pore diameter, the smaller pore will be more occupied by the EDL.
b. On the other hand, if the pore size is constant, the EDL in electrolyte solution of low ionic strength (thick λ_D) is more developing inside the pore.

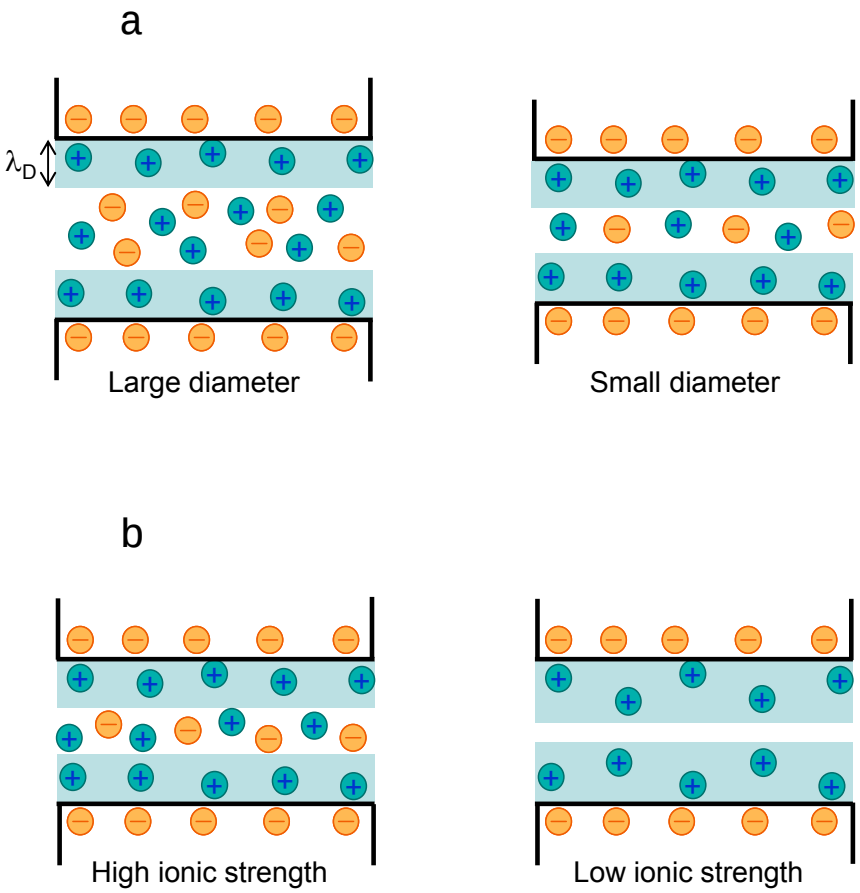

Figure 4.16: Schemes illustrating the extension of EDL inside a nanopore: (a) pore with different diameter and (b) pores of the same size with different ionic strength.

In general, the extension of EDL is proportional to the Debye length and inversely proportional to the pore diameter. It can be quantified by the following relation:

$$\text{Extension of EDL (\%)} = 100 * (2 * \lambda_D)/d \quad (32)$$

Pore diameter

The results of the molecular flux in a carboxylated membrane containing pores of different diameters (14, 20 and 28 nm) and the membrane selectivity are shown in Figure 4.17. The electrolyte in these experiments was kept constant (10 mM phosphate buffer), resulting in a λ_D value of approximately ~ 1.5 nm [85]. It is obvious that the increase in pore diameter will lead to higher molecular flux for both negatively and positively charged analytes. However, if the pore diameter is bigger, the selectivity between oppositely charged analytes becomes less. According to the calculation from Eq. (32), the extension of EDL is ~ 21, 15 and 11% in pores with diameter of 14, 20 and 28 nm, respectively. Therefore, the pore selectivity is proportional to the coverage of EDL inside pores. This means that the nanopore with smaller diameter will provide the higher selectivity.

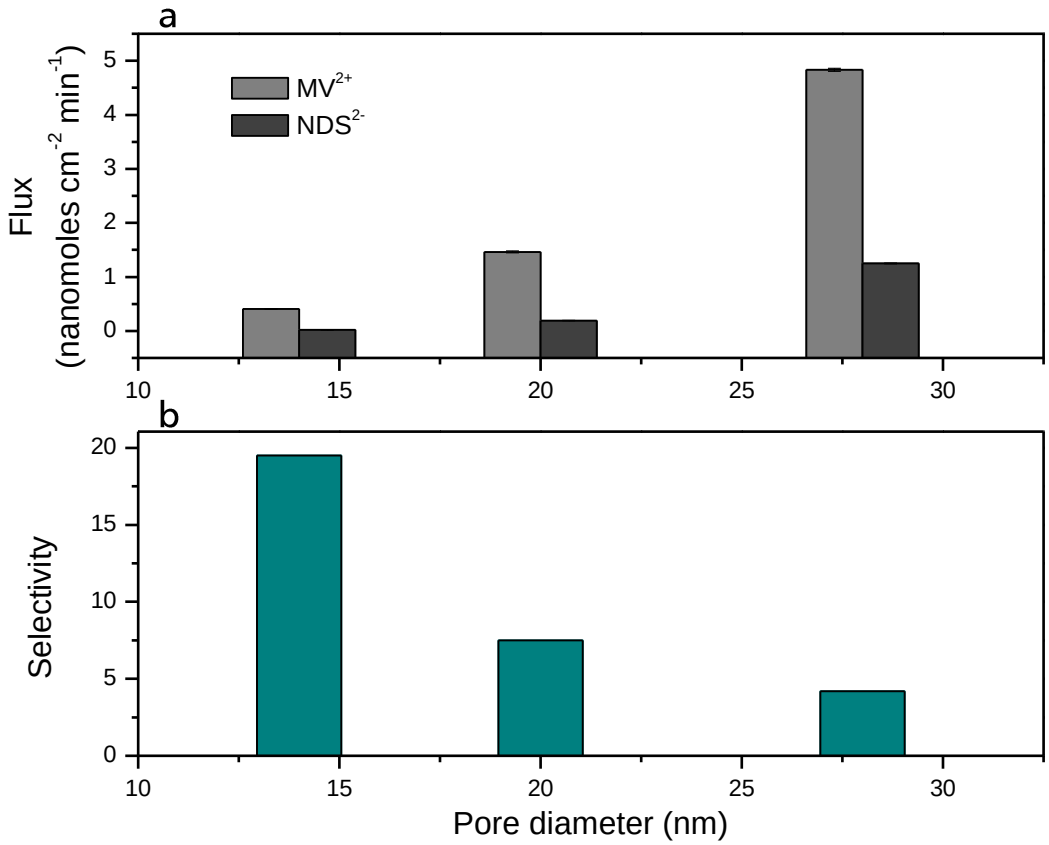

Figure 4.17: (a) Flux data of MV^{2+} and NDS^{2-} at pH 6.5 through carboxylated pores ($3x10^8$ pores cm^{-2}) with different diameter (14, 20, and 28 nm); (b) selectivity of the membrane as a function of pore diameter.

Buffer concentration (Debye length)

Buffer ionic strength provides a mechanism for adjusting the dimensions of the electrical double layer. To achieve this goal, a carboxylated (negatively charged) membrane with pore diameter ~14 nm was used for the transport of MV^{2+} and NDS^{2-}, using different buffer concentrations (100, 10 and 1 mM PBS). Figure 4.18 presents the flux data as a function of Debye length corresponding to each buffer concentration. It is obvious that the flux of MV^{2+} increases, while the flux of NDS^{2-} decreases when increasing the Debye length (decreasing buffer concentration). As a result, the selectivity was increased

from 3.1 to 18 when the concentration of buffer solution decreased from 100 to 10 mM, the selectivity was even increased up to the value of ~180 in the case of 1 mM buffer concentration. This can be explained by the fact that at low electrolyte concentrations, the Debye length, and hence the extension of the double layer, is large. The calculated extension of EDL is 6, 21 and 56% corresponding to 100 mM, 10 mM and 1 mM buffer solutions, respectively.

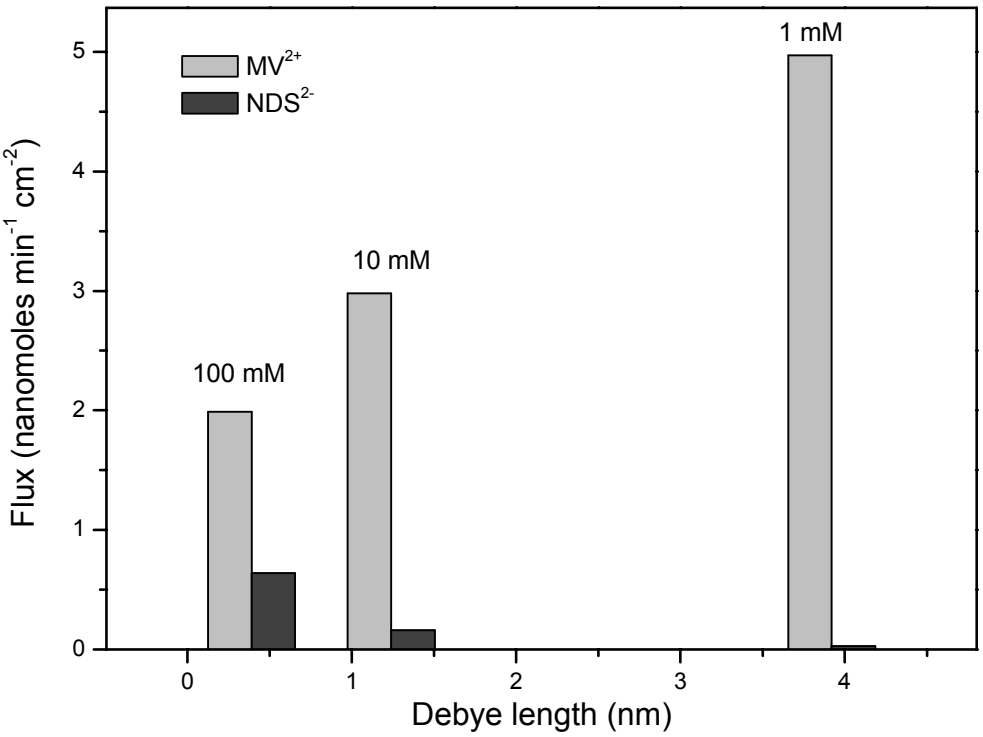

Figure 4.18: Data of MV^{2+} and NDS^{2-} flux at pH 6.5 through carboxylated pores with diameter 14 nm and pore density 7 x 10^8 cm^{-2} as a function of Debye length of buffer solutions.

The explanation for the relationship between the extension of the EDL and the selectivity of the nanopore is that the EDL results in the excess of counter-ions inside a charged nanopore. This enrichment of counter-ions in and exclusion of co-ions from the nanopore due to electrostatic interactions with the surface charge is called exclusion-enrichment effect [36]. The experimental and theoretical data obtained from the permselectivity of nanopores showed that at low ionic strength the exclusion-enrichment effect was enhanced due to the extension of the electrical double layer. In the case of a negatively charged pore, the molecular flux of negatively charged analytes is proportional to the cross section of the nanopore where the EDL is not covered. When the EDL becomes larger at low ionic strength, the effective cross section through which anions can diffuse is diminished, resulting in a lower molecular flux. For positively charged analytes, the enrichment effect at low ionic strength increases the number of molecules in the nanopore that can be transported by the diffusion. This results in a higher molecular flux. Overall, the combination of two effects leads to higher flux and selectivity of the nanopore.

Roughness of the nanopore surface

It is important to mention that the selective transport of the nanopores is achievable even in high buffer concentration. For example, the flux data in Figure 4.18 show that at 100 mM buffer concentration the carboxylated membrane also preferentially transports MV^{2+} and a selectivity coefficient of 3.1 is obtained. In this case, the EDL is very thin ($\lambda_D \sim 0.4$ nm) and the extension of EDL is only 6% in a 14-nm nanopore. The enhanced selectivity can be attributed to the surface roughness of the nanopores. The rough surface of etched PET foils was previously studied by scanning force microscopy in water [99]. In this study, by replica technique, the nanopore surface can be directly visualized by imaging the nanowires deposited in the nanopores.

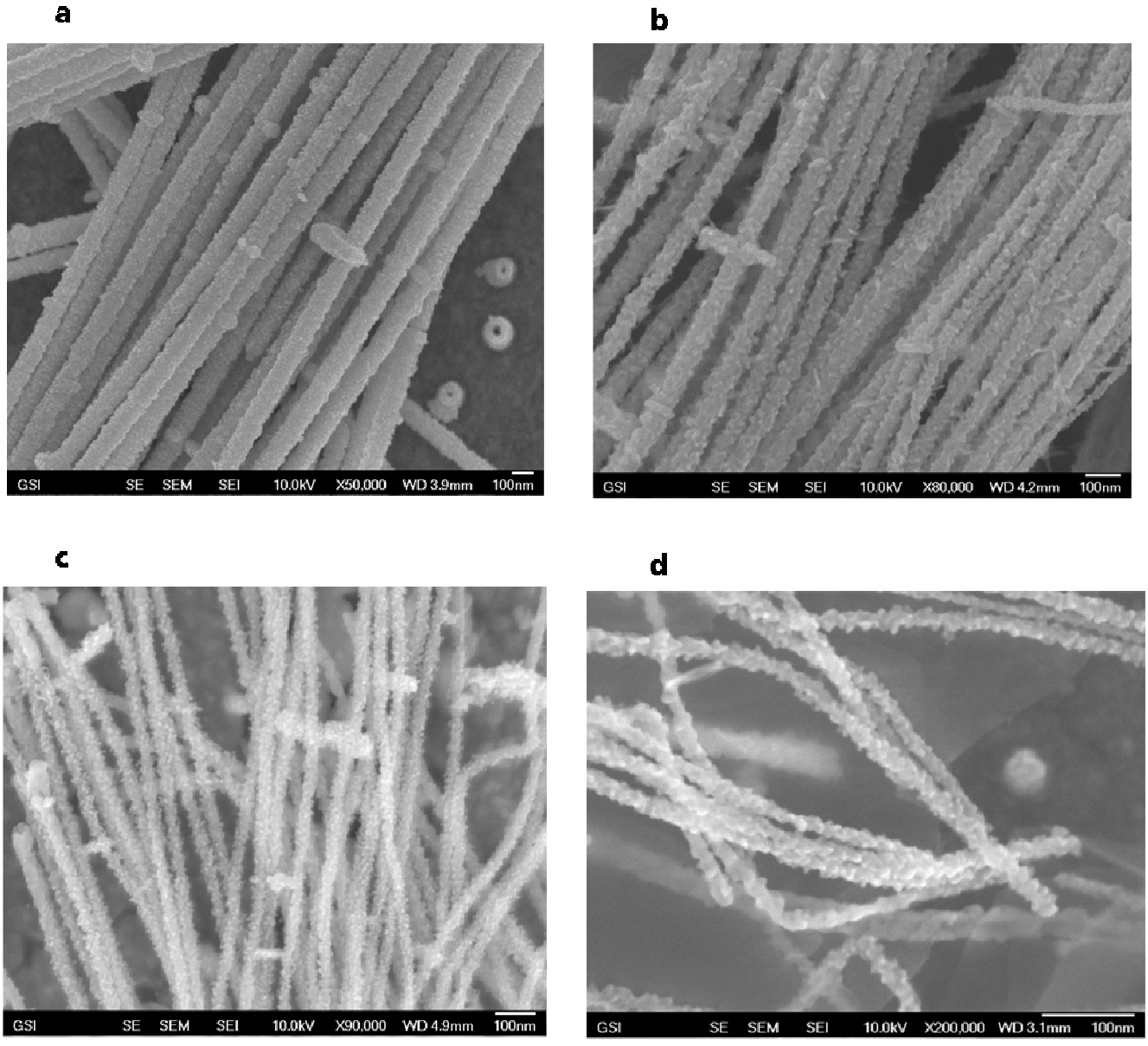

Figure 4.19: FESEM images of Au nanowires deposited in nanopores with different pore diameters. (a) $d \sim 100$ nm. (b) $d \sim 60$ nm. (c) $d \sim 30$ nm. and (d) $d \sim 20$ nm.

Figure 4.19 shows FESEM images of Au nanowires generated by filling nanopores with different pore diameters. It is obvious that the etching process of PET membranes results in roughening of the nanopore surface. Yet, the degree of roughness becomes more prominent when the pore diameter

decreases. During the etching process, the polymer chains are broken and form so-called “dangling ends”, i.e. chains with carboxylic end groups which make the pore surface rough. These dangling ends perform random movements when the etched membrane is immersed in a solution [99, 100]. The roughness of the pore walls can enhance the selectivity of the membrane by two means: (1) the surface area increased by the roughness and the movement of charged analytes which is slower inside roughness steps, resulting in an increased interaction of analytes with the charged walls; and (2) some restriction regions inside the nanopore where the effective cross-section is smaller than the opening of the nanopores, making the real extension of EDL inside the pore larger than that of the calculation.

4.4.3 Potential across the membrane

In this section, the mass transport of charged organic molecules was studied with an electric field applied across the track-etched membranes. The electric field is an efficient tool to modulate the flux of a charged molecule since its transport rate is dependent on the number of charges on the molecule, and the direction and the strength of the electric field. Under an applied voltage, the molecular flux through nanopores is controlled not only by the diffusion, but also by electrokinetic effects such as electro-osmosis, and electrophoresis. Electro-osmotic flow occurs in nanopores with charged sidewalls when an electric field applied along the pore sets the electrical double layer in motion. The EDL drags the electrically neutral bulk fluid along and, as a result, a net flow is created if the Debye length is much smaller than the pore width [101]. Electrophoresis is the flow of charged molecules under an electric field. For simple charged organic molecules in diluted buffer concentration, the direction of electrophoretic flow is the same as that of ion migration which drives a charged molecule toward the opposite pole of the electrode. The scheme illustrating electro-osmosis and electrophoresis in a negatively charged nanopore is shown in Figure 4.20.

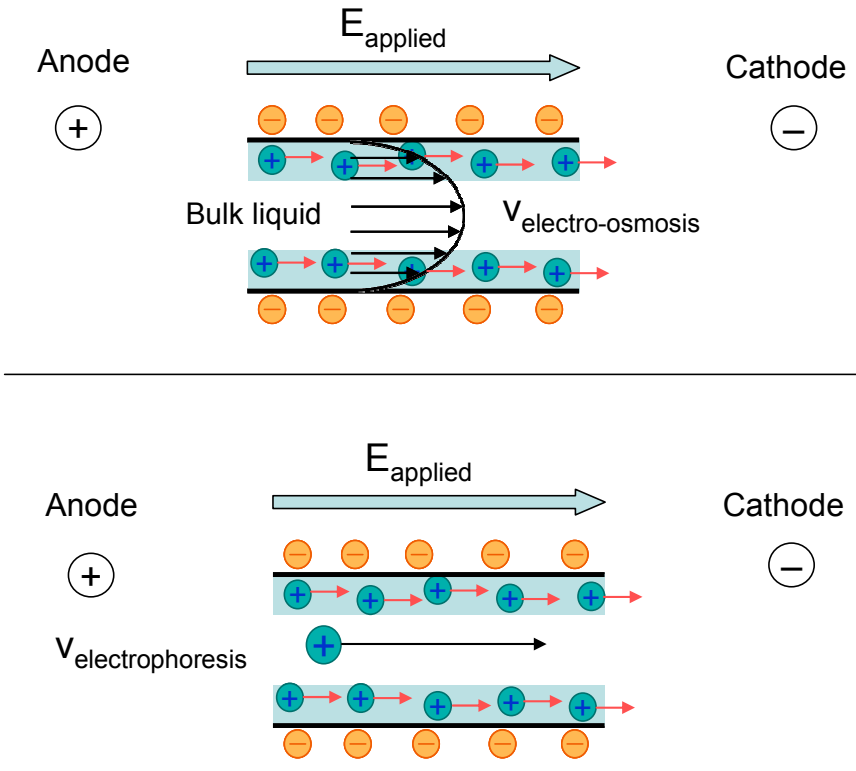

Figure 4.20: Scheme illustrating electro-osmosis and electrophoresis in a nanopore.

In this work, the effect of electric field on the transport properties of the membrane was studied experimentally. With the aim to enhance the selectivity and the throughput of the membrane, the direction of the electric field is selected in such a way that the electro-osmotic flow is in the direction from the feed cell to the permeate cell. Therefore, in the case of a carboxylated (negatively charged) membrane, the electric field is applied with the anode immersed in the feed cell (Figure 4.20). The experimental setup is shown in Figure 4.21.

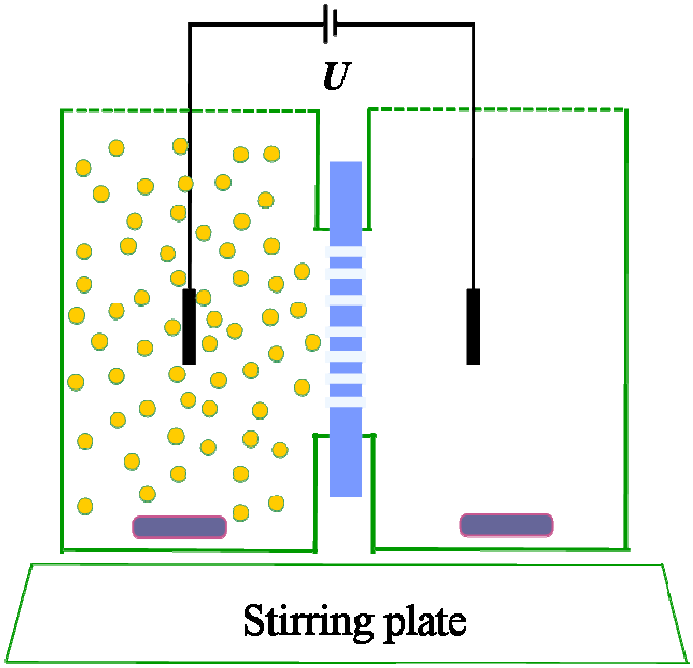

Figure 4.21: Experimental setup with an electric field applied across the nanoporous membrane.

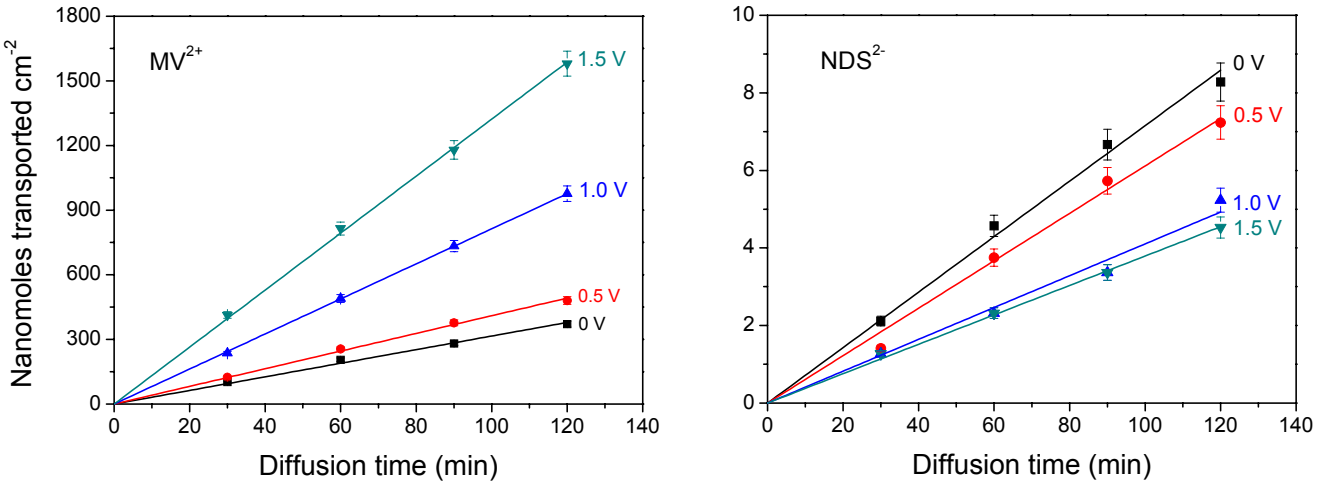

Figure 4.22: Data of MV^{2+} and NDS^{2-} flux at pH 6.5 through a carboxylated membrane with pore diameter ~ 10 nm and pore density 5 x 10^9 pores cm^{-2} for different electric field strengths.

The flux data for the transport of MV^{2+} and NDS^{2-} through a carboxylated membrane with pore diameter ~ 10 nm and pore density 5 x 10^9 pores cm^{-2} with different applied voltages is presented in Figure 4.22. The flux values and the membrane selectivity are summarized in Table 4.2. It is clearly

observed that: (1) when an electric field is applied, the flux of MV^{2+} increases and that of NDS^{2-} decreases; (2) the increase in electric field strength also increases this trend. Three main factors govern the transport of analyte through nanopores in these experiments are: (1) diffusion of molecule due to its concentration gradient; (2) electro-osmosis, driven by the high concentration cation in the EDL inside the pore, always drives solvent flow toward the cathode; and (3) ion migration (electrophoresis) also moves the charged molecules toward the oppositely charged electrode, independent of bulk solvent flow.

Table 4.2: Flux (nanomoles·cm^{-2}·min^{-1}) data and selectivity coefficient (α) in experiments with an applied electric field.

Applied Voltage (V)	Flux		α
	MV^{2+}	NDS^{2-}	
0	3.16	0.072	43.9
0.5	4.10	0.061	67.2
1.0	8.13	0.041	**198.3**
1.5	13.22	0.038	**347.9**

In the absence of an electric field, transport of analyte is governed by the diffusion which drives the analyte from high concentration region (feed cell) to low concentration region (permeate cell). Therefore, the surface charge and double layers within the pores are expected to play an important role in transporting charged analytes through nanopores. The high membrane selectivity to MV^{2+} is obviously due to negatively charged surface, narrow pores (~ 10 nm) and thick double layer (~ 3 nm for 10 mM phosphate buffer). In the presence of the electric field, electro-osmotic and electrophoretic forces will contribute to the analyte permeability. Considering the transport of MV^{2+}, the electro-osmotic flow of the solution inside the pore drives the analyte towards the cathode (permeate cell) due to the EDL of positive ions. Also, the electrophoretic force moves positively charged analyte towards the cathode (negative pole). Both these effects lead to the dramatic increase in MV^{2+} flux. In the case of NDS^{2-}, the electro-osmotic flow moves analyte to the cathode (permeate cell) but the electrophoretic force drives NDS^{2-} to the anode (feed cell). Therefore, there is a competition in the control of NDS^{2-} flux. The data from Table 4.2 show that the flux of NDS^{2-} decreases when the electric field strength increases. That means the electrophoresis dominates the analyte transport in this case. The electro-osmosis also plays a role but has less impact.

The reproducibility of the results was confirmed with positively charged nanopores modified with PEI. In these experiments, the electric field was applied in such a way that the cathode was immersed in the feed solution. With this configuration, electro-osmosis and electrophoresis will move NDS^{2-} to the anode (permeate cell) and MV^{2+} to the cathode (feed cell). As a result, the flux of NDS^{2-} increases and that of MV^{2+} decreases, as can be seen in Figure 4.23. The selectivity is ~ 400 with 1 V applied as compared to 28 without an electric field.

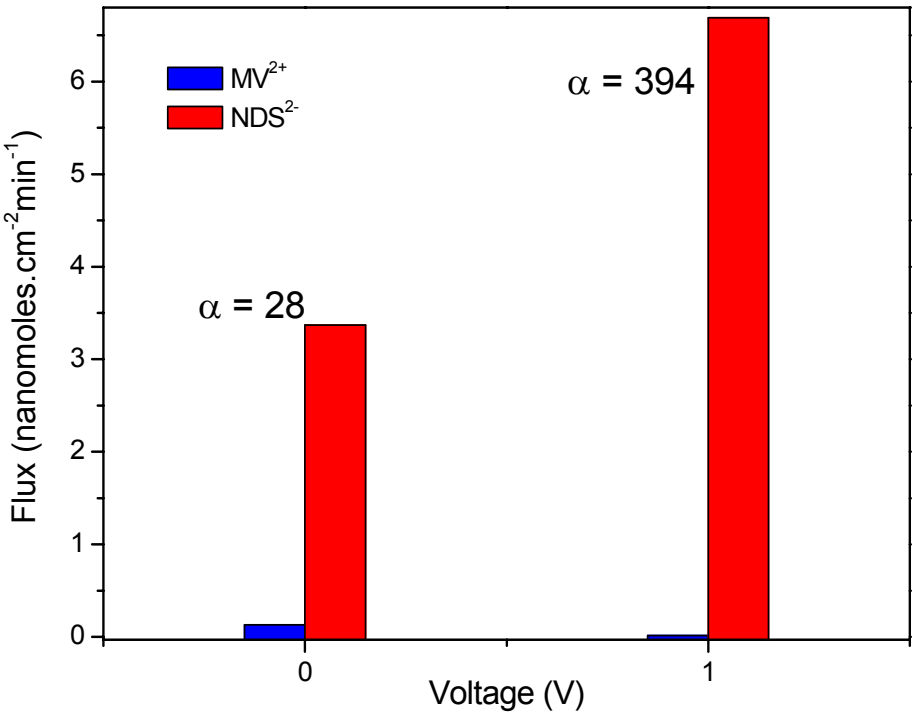

Figure 4.23: Data of flux of MV^{2+} and NDS^{2-} at pH 6.5 through aminated (PEI) membrane with pore diameter ~ 10 nm and pore density 5 x 10^9 pores cm^{-2} prior to and after the application of an electric field.

4.5. Transport of a mixture of organic molecules

Track-etched nanopores in PET membranes show high permselectivity to charged molecules, suggesting that these membranes are useful for the separation of anionic and cationic species. To test this, a transport experiment with a mixture of two charged molecules was performed. In this case, the feed-half cell was filled with a mixture of MV^{2+} and NDS^{2-} (10^{-4} M concentration of each analyte) in the same buffer solution (10 mM and pH = 6.5). Carboxylated nanopores with density 10^{10} pores cm^{-2} and pore diameter 10 nm were used for this purpose. An electric field of 1 V was applied in a way that the cathode was immersed in the permeate-half cell.

Figure 4.24a shows absorption spectra for 10^{-4} M MV^{2+}, 10^{-4} M NDS^{2-} and a mixture of the two species. It can be seen that NDS^{2-} has a strong absorption band at 226 nm, where the absorption of MV^{2+} is very weak. On the other hand, MV^{2+} shows a peak of absorbance with a maximum at 258 nm, where the NDS^{2-} absorbance is weak. Figure 4.24b depicts the absorption spectrum of the permeate solution after 120 min of the transport experiment. From the measured absorbances at 226 nm and 258 nm, the concentration of both analytes in the permeate solution can be calculated. It was observed that the concentration of MV^{2+} is ~ $4.5x10^{-5}$ M while there was no NDS^{2-} detected. In other words, after 120 min of the permeation, about half of the MV^{2+} molecules were successfully separated from the mixture of the two species. Therefore, it can be concluded that track-etched nanopores in PET membranes can be exploited in the separation application of charged molecules.

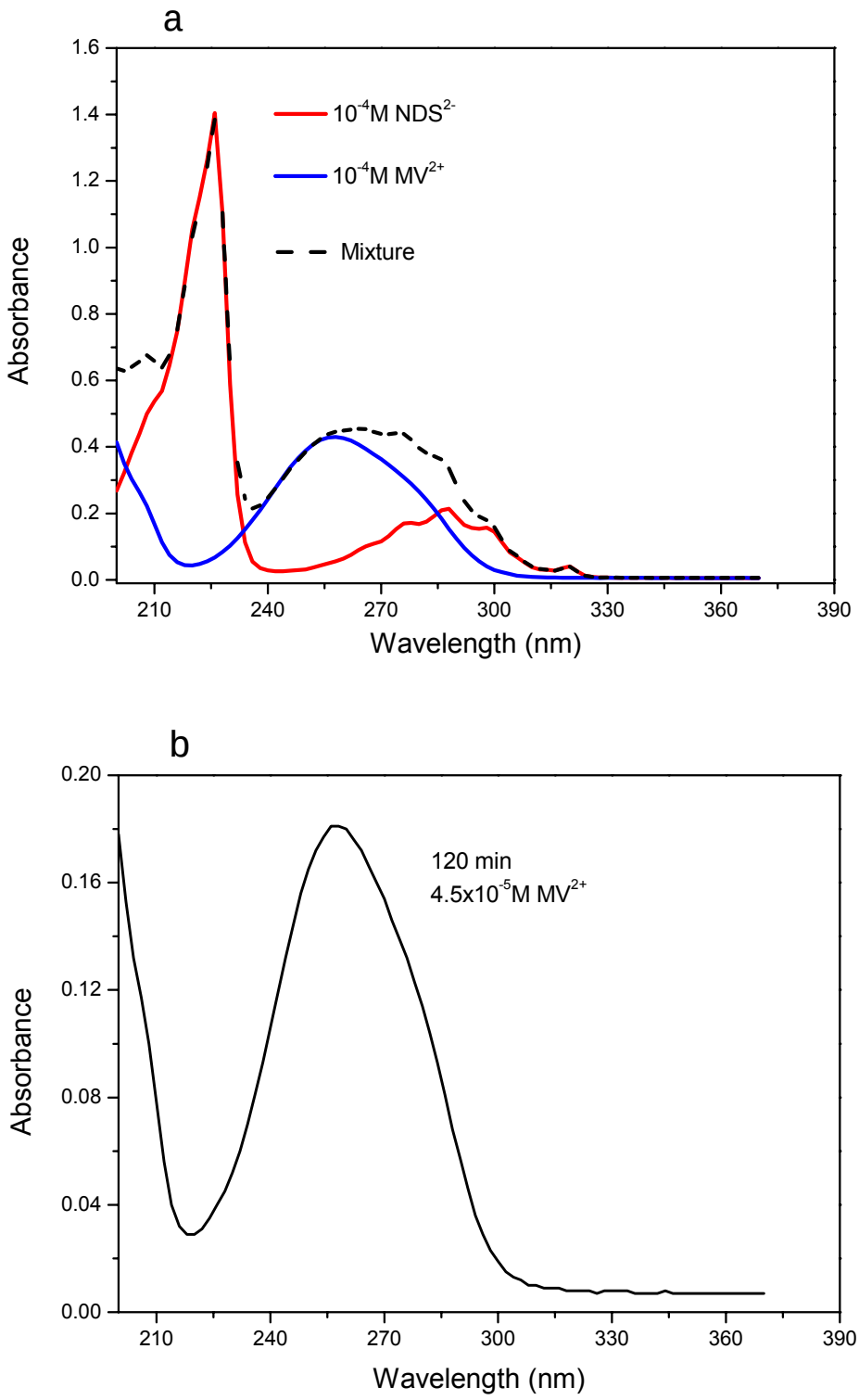

Figure 4.24: Absorption spectra of analyte solutions in two-molecule transport experiment. (a) Spectra of solutions of 10^{-4} M MV^{2+}, 10^{-4} M NDS^{2-} and of a mixture of the two species before the permeation. (b) Spectrum of the permeate solution after 120 min of permeation.

4.6 ATP modulated transport through track-etched nanopores

The scientific community has been interested in developing different methodologies to achieve active control over the ionic/molecular transport in nanoconfined environment under the influence of external stimulus for separation, or drug delivery. The previous sections described how the control of the ionic species is modulated by the surface charge of pores. However, permeability of ionic species can also be controlled via steric blocking or unblocking of the molecular gates. For instance, ten Elshof and co-workers have introduced the concept of molecular gate which was physically opened or closed by the addition of surfactant molecules [102]. Recently, Li and coworkers have demonstrated a pH responsive smart gate, in which charged nanoparticles play a key role to control the open/close state of the gate for the transport of biomolecules [103]. Moreover, the ionically controlled nanoscopic molecular gates have been developed by using an ordered mesoporous material functionalized with a monolayer of polyamine at the external surface. The gate opens/closes via tuning the pH value and/or with the addition of anions in the bulk solution [104]. In this framework, the creation of such artificial nanodevices based on synthetic pores is still a remaining challenge in the biophysics and materials science communities.

In this section, the fabrication of an anion controlled molecular gate based on track-etched nanopores modified with polyethyleneimine (PEI) is demonstrated. The ionic/molecular transport can be accurately controlled by manipulating the adenosine 5´-triphosphate (ATP) concentration in the external environment. The experiments were performed with cylindrical multi-nanopores and single conical nanopores. The presence of ATP leads to significant decrease in the flux of charged molecules (NDS^{2-}) in cylindrical nanopores as well as to the rectified ion flux in single conical nanopores, representing the closure of the ionic gate. The scheme illustrating the function of the gate is shown in Figure 4.25.

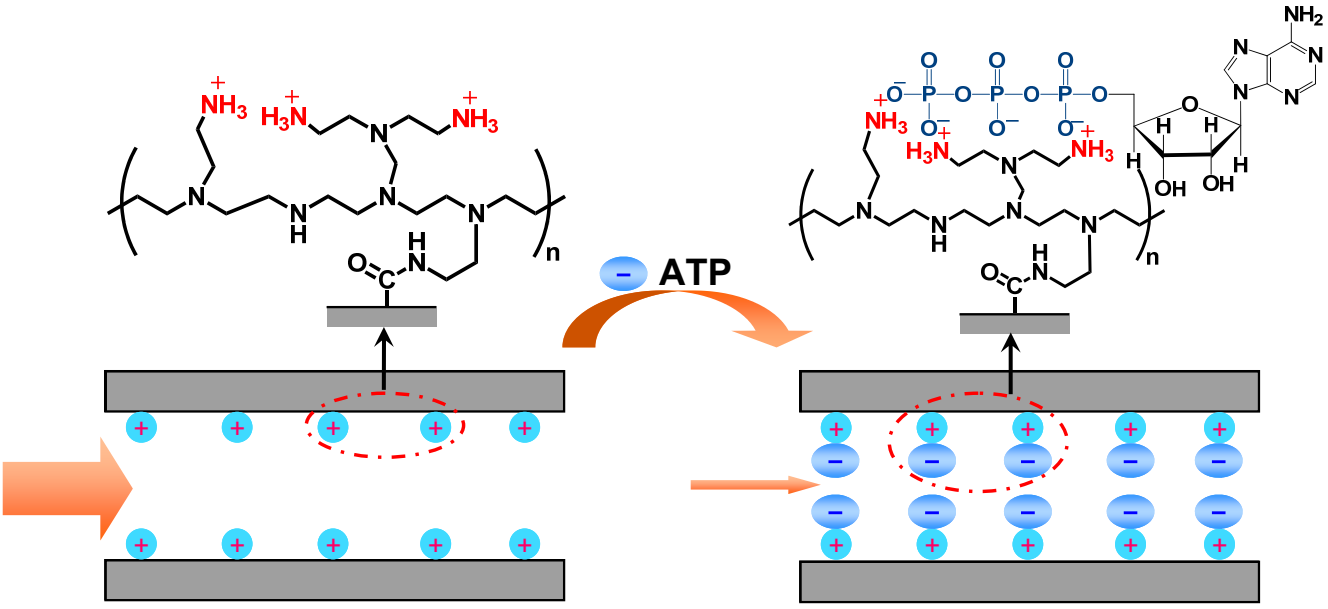

Figure 4.25: Scheme illustrating the function of the gate in a cylindrical PEI modified nanopore.

The influence of co-addition of ATP in the analyte solution on the selective permeability was investigated by monitoring the ionic flux of doubly charged dye NDS^{2-} through PEI-modified membranes. The mass-transport experiments were performed with membranes containing cylindrical nanopores (10^9 pores cm^{-2}). Figure 4.26 displays the permeation flux of NDS^{2-} across two track-etched

membranes of different pore diameters before and after the addition of ATP along with analyte (NDS^{2-}) in the feed solution. It is evident that in the absence of ATP, the PEI-modified membrane selectively permeates NDS^{2-} molecules across the pores. The charged pore walls play a significant role in this permeation process. As discussed above, an electrical double layer was generated inside the charged pore, which contains a higher concentration of NDS^{2-} ions. Therefore, NDS^{2-} ions selectively diffused through the membrane. However, the fluxes of NDS^{2-} were drastically decreased in the presence of ATP (100 μM) in the feed solution. Namely, the molecular fluxes are about 80% lower than that in the absence of ATP. A possible explanation for this is that the bulky ATP molecules, being electrostatically attached to the inner walls, led to the reduction of surface charges and also inner pore diameter, which in turn suppresses the selectivity and the observed NDS^{2-} ion flux.

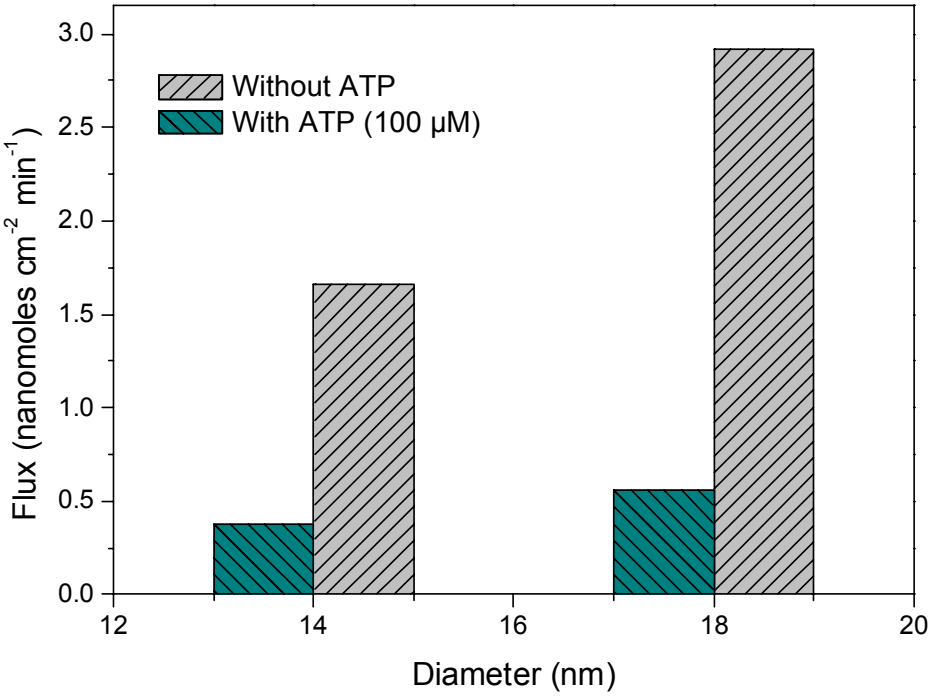

Figure 4.26: Diffusion of NDS^{2-} analyte through PEI-modified membrane, containing cylindrical nanopores (10^9 pores cm^{-2}) of ~ 18 and 14 nm in diameter prior to and after the addition of 100 μm ATP in the analyte solution.

In order to check the reproducibility of the system, also experiments on single conical nanopore were performed. A membrane containing a single conical nanopore was mounted between the two halves of the conductivity cell, and both halves of the cell were filled with 0.1 M KCl (pH = 6.5) solution. The measurements of *I-V* curves were mentioned in section 3.6. Various concentrations of ATP prepared in the same electrolyte solution were used for the measurement of respective *I-V* curves.

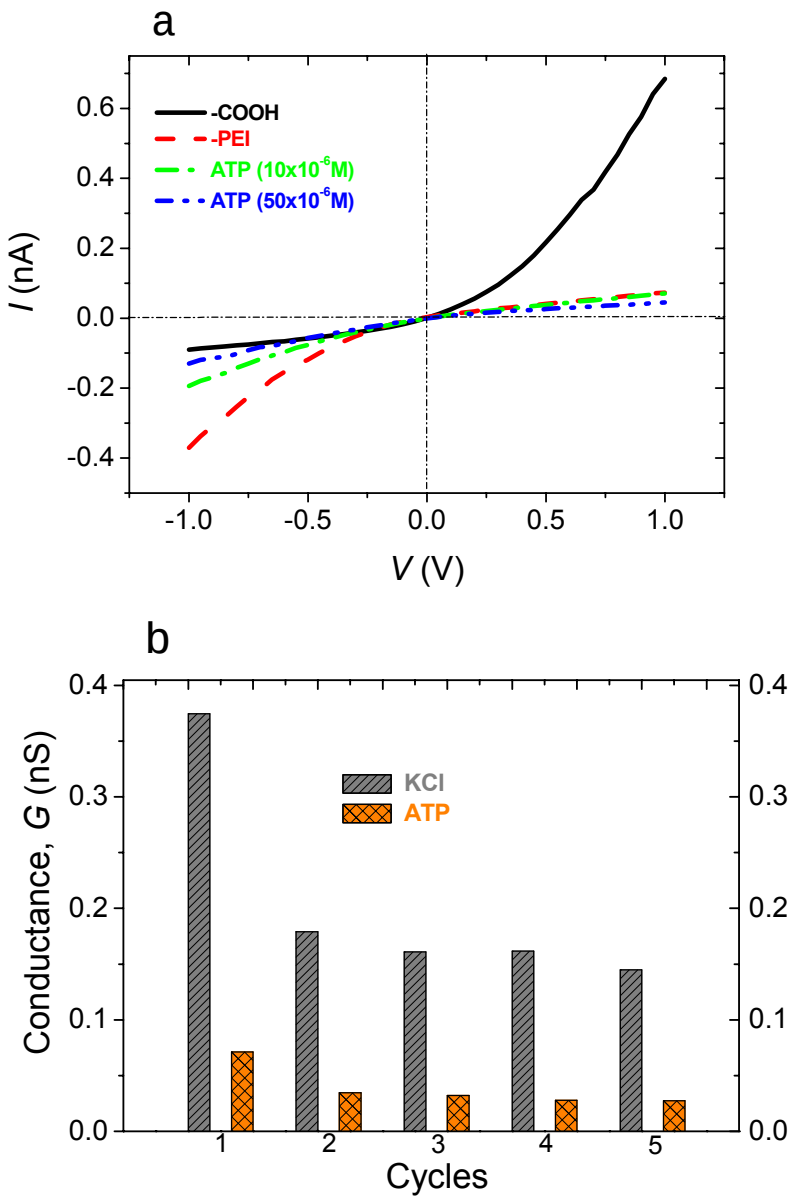

Figure 4.27: (a) *I–V* curves corresponding to a single conical nanopore with tip $d \sim 9$ nm and base $D \sim 170$ nm in diameter, prior to (black solid line) and after (red dashed line) functionalization with PEI measured in 0.1 M KCl electrolyte solution along with different ATP concentrations. (b) Reproducible variation of pore conductance in the absence ("on" state) and presence of ATP ("off" state) in the electrolyte solution (*I-V* curves are measured by Dr. Mubarak Ali).

Figure 4.27a shows *I–V* curves of a single conical nanopore prior to and after modification with PEI. As is well-known, the direction of rectification in conical pores is solely based on polarity and magnitude of surface charge. Before modification, the pore rectifies the ionic current due to the presence of inherent $-COO^-$ groups. After modification, pore surface charge and polarity were switched from negative to positive, resulting in the inversion of rectification [105, 106]. As expected, the presence of ATP, even at micro molar concentrations in the electrolyte solution, led to a significant decrease in the rectified ion current which in turn reduced the pore conductance. The conductance of a PEI-modified pore measured at -1 V was 0.37 nS. The addition of 10 μM ATP reduced the conductance to 0.19 nS, i.e., ~ 48% decrease

was recorded. This decrease in conductance was even more pronounced when working with more concentrated ATP solutions.

The presence of 50 μM ATP resulted in a further reduction of pore conductance to 0.13 nS. It means that increasing the ATP concentration from 10 to 50 μM resulted in a ~ 65% decrease in conductance compared to the initial value under the applied bias. As is well-known, ionic conductance in confined geometries depends on two factors: (i) surface charge density and (ii) effective diameter of the pore [9, 107]. The electrostatically adsorbed ATP analyte led to the reduction of both charge density and effective diameter, especially at the tip opening which governs the ionic transport across the conical pore. At low ATP concentrations, both factors might play a significant role in the reduction of pore conductance. But at high concentration, it was observed that high ATP concentrations lead to the blockage of pore tip instead of flipping the surface charge, and the applied electric field cannot break the ATP binding from the pore surface [108]. This clearly demonstrates that in our case the size of ATP plays a dominant role in the ion flux blocking. The above experimental results provide clear evidence that the PEI-modified pore acted as an anion-controlled molecular gate. The gate was only opened in the presence of small anions such as Cl^-, while bulky ATP anions, having a hydrodynamic radius ~ 0.8 nm [109], closed the gate through the formation of strong complexes with the protonated amino groups at the pore tip opening. Rostovtseva and Bezrukov reported that the single voltage-dependent anion pores (mitochondrial porin) reconstituted into a planar lipid bilayer also exhibit a decreased ionic current in the presence of ATP, which in turn suppresses the pore conductance [109].

Figure 4.27b displays the reproducibility of the system in terms of open “ON” and closed “OFF” states of the nanogate. It was observed that, in measuring the second cycle, the pore did not gain the initial level of conductance. This can be interpreted considering that a specified number of ATP molecules remain attached to the pore surface through hydrogen bonding which could not be washed out completely. Further reversing the ATP concentration in the electrolyte solution reflects highly reproducible changes in the pore conductance, and the difference between the higher conducting state and the lower one is remarkably constant.

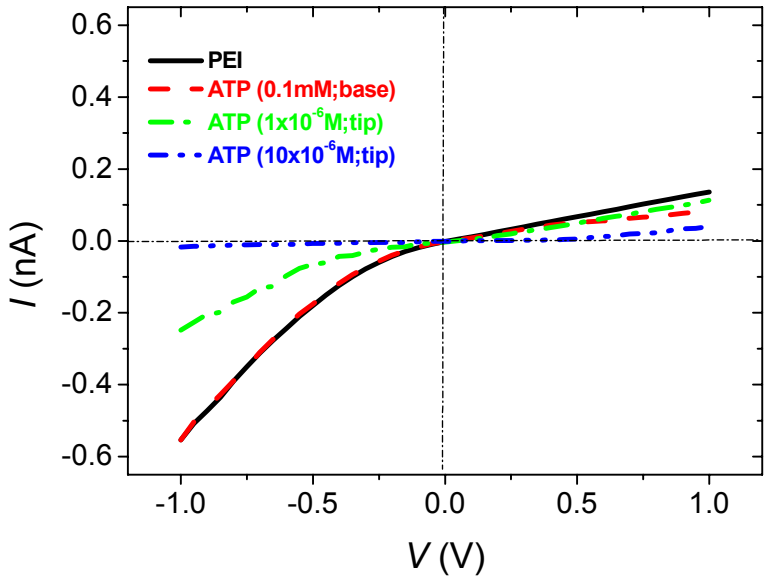

Figure 4.28: Current–voltage characteristics of a PEI-modified pore with tip $d \sim 6$ nm and base $D \sim 272$ nm in diameter, measured in 0.1 M KCl with asymmetric addition of ATP concentrations (*I-V* curves are measured by Dr. Mubarak Ali).

Moreover, we have also investigated the effect of ATP on *I–V* curves, upon exposing the pore to ATP concentration under asymmetric conditions (Figure 4.28). It is worth mentioning that the PEI-modified conical pores rectify the ion current due to the flow of anions (Cl^- ions) from tip to base opening. By employing ATP on the base side, we did not observe any change in the rectified ion flux through the tip opening. Due to the anion-selective behaviour of the pore, ATP molecules situated on the base side do not pass through the tip. Therefore, they do not have any impact on charge and effective diameter at the tip side. In contrast, introduction of ATP on the tip side led to a significant decrease in the rectified ion current. Here, adsorbed ATP molecules shield the positive charges and also have an impact on the tip diameter which governs the ionic transport. Therefore, the addition of 1 and 10 mM ATP on the tip opening induces a decrease of ~55 and 97% in the transmembrane ionic current, respectively. Hence, high ATP concentration led to almost complete blockage of ionic current. This clearly demonstrates that the bulky ATP anions were electrostatically trapped during their passage at the tip opening and hindered the flow of ions through the pore.

In short, we have described here the construction of a device which demonstrates ATP-modulated ionic transport through synthetic nanopores. The “on/off” switching is chemically actuated via ATP in the external environment with which the molecular gate is opened and closed. The functioning is based on the electrostatical/hydrogen-bonding interactions of ATP which in turn control the ion flux through the nanopores. In this context, we believe that such simple and economically affordable nanodevices would be applicable for sensing, directed molecular transport and separation, and targeted drug delivery at the nanoscale level.

4.7 Saccharide/glycoprotein recognition inside synthetic ion pores modified with boronic acid

For biosensors being developed based on molecular recognition, the recognition of carbohydrates in water is very important in many respects. Saccharides play a crucial role in various metabolic processes and other biological activities, such as cellular recognition [110] and signal transduction [111], or as targets for bacterial infections [112]. In particular, the control of glucose concentration in blood is essential for patients suffering from diabetes mellitus. Additionally, the quantification of fructose or other saccharides in food and beverages is another important field of interest. Up to now, most biosensors for saccharide recognition mainly rely on the use of an enzymatic assay. Particularly, glucose sensors function on the basis of the reaction between glucose and glucose oxidase or glucose dehydrogenase to generate redox mediator species, which are thereafter detected electrochemically [113]. Fructose has been detected by fructose dehydrogenase enzyme [114]. While providing good selectivity to target saccharides, such sensors rely on the rate of reaction between the enzyme and saccharides and hence are inherently sensitive to factors influencing enzyme activity. In addition, current enzymatic based sensors offer specificity for only a few saccharides and are unstable under harsh conditions [115, 116].

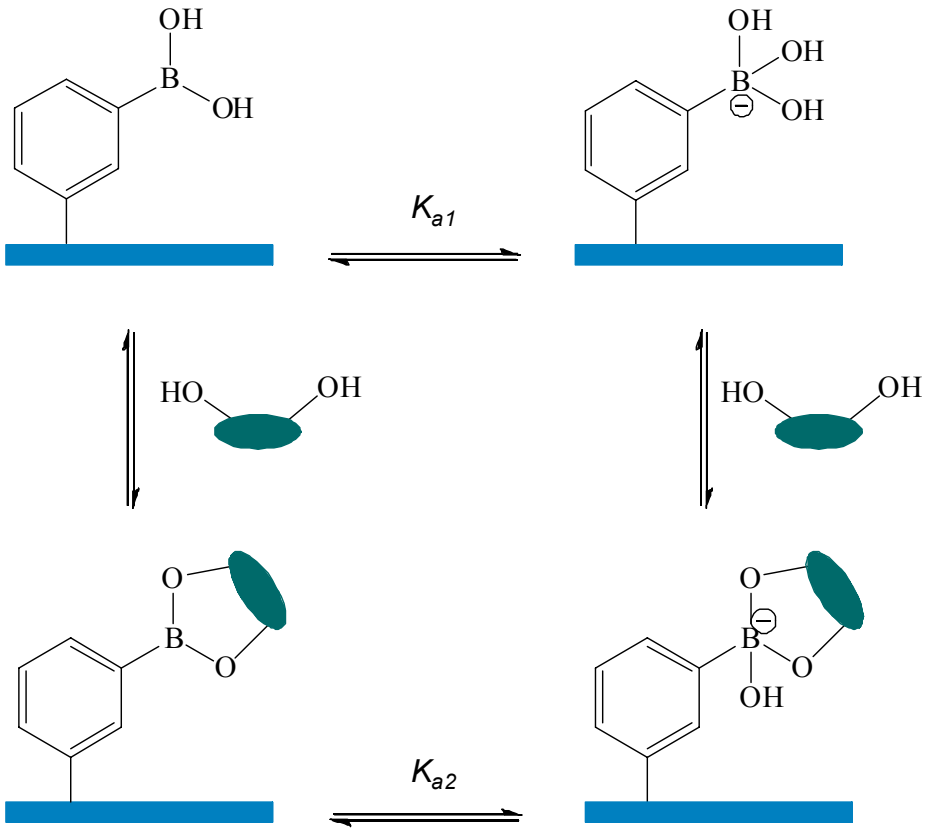

Figure 4.29: Scheme illustrating the binding process between phenylboronic acid and a diol (a molecule containing two hydroxyl groups). The blue bar represents the nanopore surface.

Through synthetic design, there exists the potential to develop stable sensors for saccharides, which could be both sensitive and selective for a desired saccharide. To date, many detection systems that have been developed rely upon noncovalent interactions, such as hydrogen bonding, for recognition of guest species. However, in the case of aqueous systems neutral guests may be heavily solvated. Therefore,

synthetic receptors, using non-covalent interactions, have not yet been designed due to the effective hydrogen bonding competition of bulk water for low concentrations of monosaccharides [117]. For this reason, a great deal of attention has been devoted to the development of synthetic molecular receptors using boronic acid (BA) based compounds. In aqueous basic media, boronic acids are known to form, rapidly and reversibly, five- and six-membered cyclic esters with *cis*-1,2- and 1,3-diols, respectively. The binding process of phenylboronic acids with diols is illustrated in Figure 4.29. Due to their linked array of hydroxyl groups, saccharides provide an ideal structural framework for binding to boronic acids [118]. While enzyme-based sensors are not directly amenable to the detection of bound sugars, an affinity-based sensor can potentially be employed for the detection of both free and bound sugars. In contrast to enzymatic sensors, the detection principle here rests on complexation, which is a reversible, equilibrium-based reaction without the consumption of the analyte.

Here, we demonstrate a facile method to fabricate monosaccharide/glycoprotein sensors using single conical nanopores prepared in polyethylene terephthalate (PET) membranes. Such single pores have proven to function as a novel biosensing platform based on surface charge dependent ionic transport across the pore [11, 119]. Because of the track-etching process, carboxyl (–COOH) groups were generated on the pore surface. Then, the BA receptor was covalently attached to the pore surface by coupling chemistry. The BA-modified pores have the ability to detect common monosaccharides (glucose, fructose). The detection principle is derived from the measurement of current–voltage (*I*–*V*) characteristics of the nanopores in electrolyte solutions. In conical nanopores, rectification and permselectivity depend strongly on surface charge density and effective diameter, especially at the tip opening of the pore. Any minor change in the surface charge or effective cross-section can lead to a detectable change of the *I*–*V* signal. In the presence of saccharides, the saccharide–boronic acid complex results in the change of surface charge from neutral (boronic acid) to negative (boronate ions). In addition to free carbohydrate, the sensing platform can also be able to detect bound-carbohydrate moieties in ovalbumin (glycoprotein). In the case of glycoprotein, the binding with BA changes both the nanopore surface charge and the effective pore diameter.

4.7.1 Functionalization of pore surface with boronic acid

The conical nanopores in PET membranes were fabricated by means of track-etching technique. As a result of the etching process, carboxyl (–COOH) groups are generated on the nanopore walls with a density of about one group per nm^2. The boronic acid receptor was covalently attached to the pore wall through carbodiimide coupling chemistry. The carboxyl groups and amino groups of 3-aminophenylboronic acid molecules (APBA) were linked via an amide bond to the pore surface (see Figure 3.12). The successful BA immobilization was confirmed by measuring the *I*–*V* curves of unmodified and BA-modified nanopores in 0.1 M KCl at neutral pH. The $–COO^-$ groups are negatively charged at neutral pH, and therefore the as-prepared conical pore is cation selective and exhibits the ion current rectification characteristic [92]. The current is rectified due to the preferential flow of cations from the small toward the large pore opening. As a result, the *I*–*V* curve exhibits rectification behavior with a high conducting state ($V > 0$) and a low conducting state ($V < 0$), as shown in Figure 4.30a. When BA is chemically attached to the inner pore walls, there exists an equilibrium between neutral boronic acid (**1**) and negatively charged boronate (**2**) as shown in Figure 4.29. The pK_{a1} of this process in the case of APBA is found to be ~8.9 [120]. Therefore, at pH 7 which is approximately 2 units lower than the pK_a, BA groups are mostly in neutral (uncharged) state. Consequently, a BA-modified pore exhibits a linear *I*–*V* curve (Figure 4.30b).

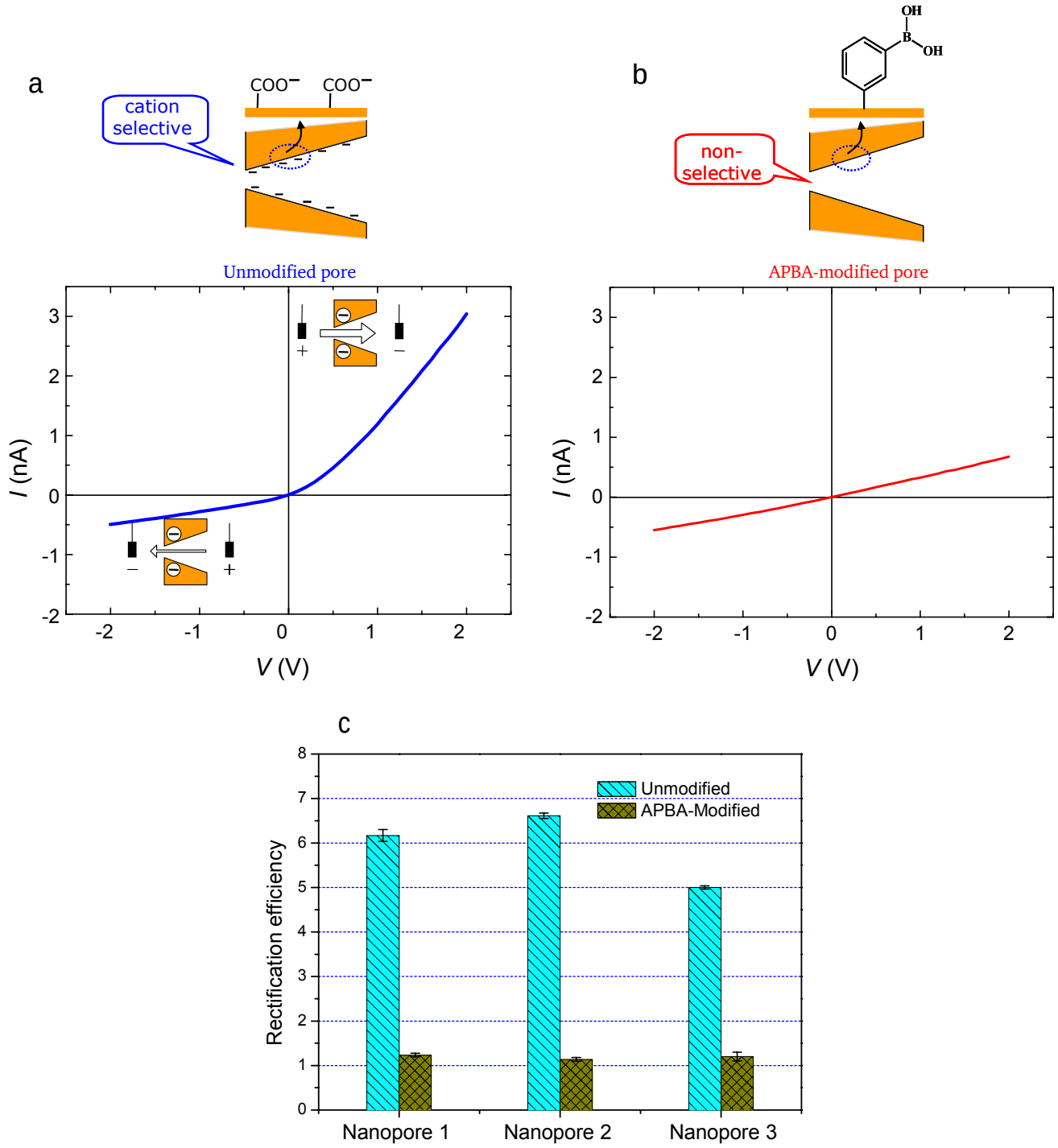

Figure 4.30: Current–voltage characteristics in 0.1 M KCl (pH 7) of nanopore having $D = 530 \pm 40$ nm and $d = 8 \pm 1$ nm: (a) unmodified nanopore and (b) APBA-modified nanopore; (c) Rectification efficiency (at 2 V) of different nanopores prior to and after modification: nanopore 1 ($D = 530 \pm 40$ nm, $d = 8 \pm 1$ nm), nanopore 2 ($D = 460 \pm 20$ nm, $d = 13 \pm 2$ nm), nanopore 3 ($D = 480 \pm 30$ nm, $d = 16 \pm 2$ nm).

The rectification properties of the nanopores can be quantified by calculating the rectification degree (f_{rec}) defined as the ratio of absolute values of ion current measured at voltages of the same amplitude but opposite polarities. Figure 4.30c exhibits the reproducibility of modification reaction. In the case of unmodified pores, a rectification degree at pH 7 (2 V) displays well-defined rectification behavior with high f_{rec} values (~6). For BA-modified nanopores, the f_{rec} values were close to 1 (~1.2), indicating that the pore surface is almost uncharged which in turn led to loss of the rectification characteristics of the pore.

4.7.2 Binding mechanism between boronic acid and diols

In order to elucidate the sensing mechanism, the reversible binding between boronic acid and diols of carbohydrate moieties has to be demonstrated. The binding scheme is shown in Figure 4.29. As mentioned above, in the absence of saccharides, both uncharged (**1**) and negatively charged forms (**2**) of BA exist in equilibrium with a certain pK_{a1} (~8.9). In the presence of saccharides, boronic acid covalently reacts with 1,2 or 1,3 diols to form a five- or six-membered cyclic ester, respectively. The esters of the complex also exist in equilibrium with the uncharged (**3**) and negatively charged (**4**) forms. It is known that pK_a of the ester is often about two to four units lower than that of the corresponding boronic acid. This is due to the fact that the saccharide–boronic acid complex is a stronger acid than the free boronic acid [121]. The values of pK_{a2} of boronate esters from phenylboronic acid with fructose and with glucose are 4.6 and 6.8, respectively [122]. For the sensing of monosaccharide molecules, the working pH should be in between pK_a of boronic acid and pK_a of ester form. Therefore, the pH 7 was chosen and at this pH, the nanopore surface is switched from neutral to negative by the addition of glucose/fructose. The change in surface charge is confirmed by *I*–*V* characteristic measurements. The pH-dependent reversible binding scheme is shown in Figure 4.31a, and the results of glucose binding in an APBA-nanopore are given in Figure 4.31b. In the absence of glucose, the *I*–*V* curve shows ohmic behavior with a f_{rec} value of 1.2. In the presence of 20 mM glucose, diols in glucose form a reversible boronate complex with the boronic acid group on the nanopore surface. The negatively charged complex then rectifies the current to a certain extent with higher f_{rec} value (2.2). Since the glucose binding is reversible, after washing the nanopore with an acidic solution (pH 3), the complex became unstable, the glucose molecules were released, and the nanopore surface was regenerated by uncharged boronic acid groups. Therefore, almost loss of rectification characteristics was observed with f_{rec} ~1.2.

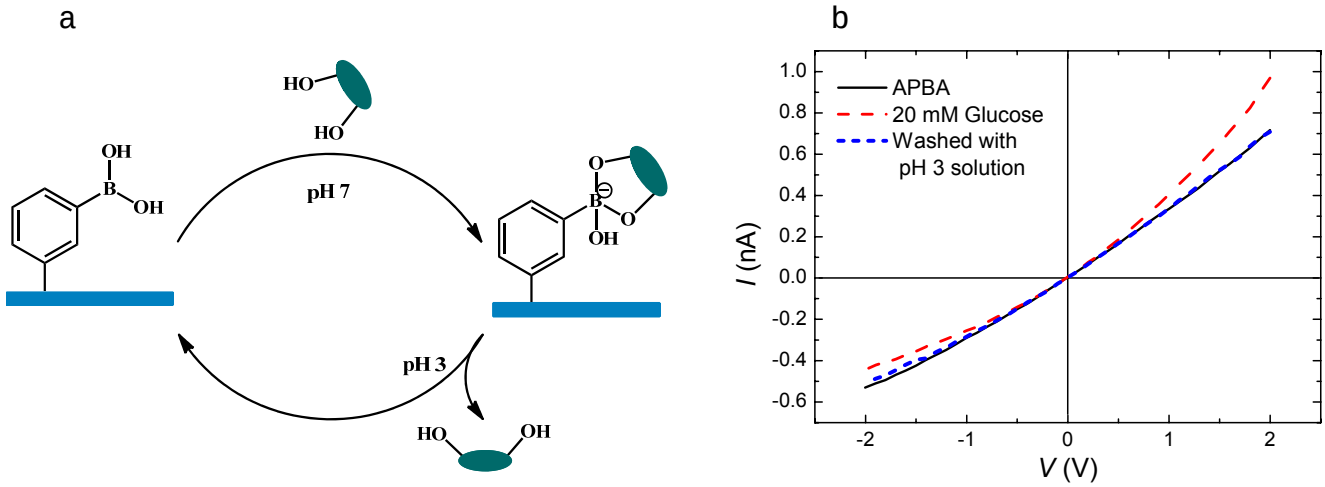

Figure 4.31: (a) Scheme of reversible binding between a saccharide and a boronic acid receptor; (b) *I*–*V* curves for 0.1 M KCl solution in a nanopore (D = 530 ± 40, d = 8 ± 1 nm): APBA-modified nanopore (black solid line); after addition of 20 mM glucose (red dashed line) and after washed with pH 3 solution (blue dotted line).

It is also important to be sure that the binding events which result in an increase of rectification efficiency of nanopores are the complex formation of boronate anions between boronic acid and diols in saccharide molecules. Additional experiments have been performed in the following way: A

carboxylated conical nanopore was modified with propylamine instead of APBA. This also neutralizes the surface charge of the nanopore wall similar to the APBA-modified nanopore, because the hydrocarbon $-C_3H_7$ group has no charge. The results in Figure 4.32a show the *I–V* curves of a nanopore prior to and after modification with propylamine. It is obvious that the propylamine-modified nanopore shows linear behavior as compared to the well-defined ion current rectification behavior of the carboxylated nanopore. The effect of glucose concentration (5–30 mM) on current rectification was also studied (Figure 4.32b). It was found that the addition of glucose in solution did not change the *I–V* behavior of the pore which indicates that the propyl group has no binding affinity towards diols in saccharide molecules.

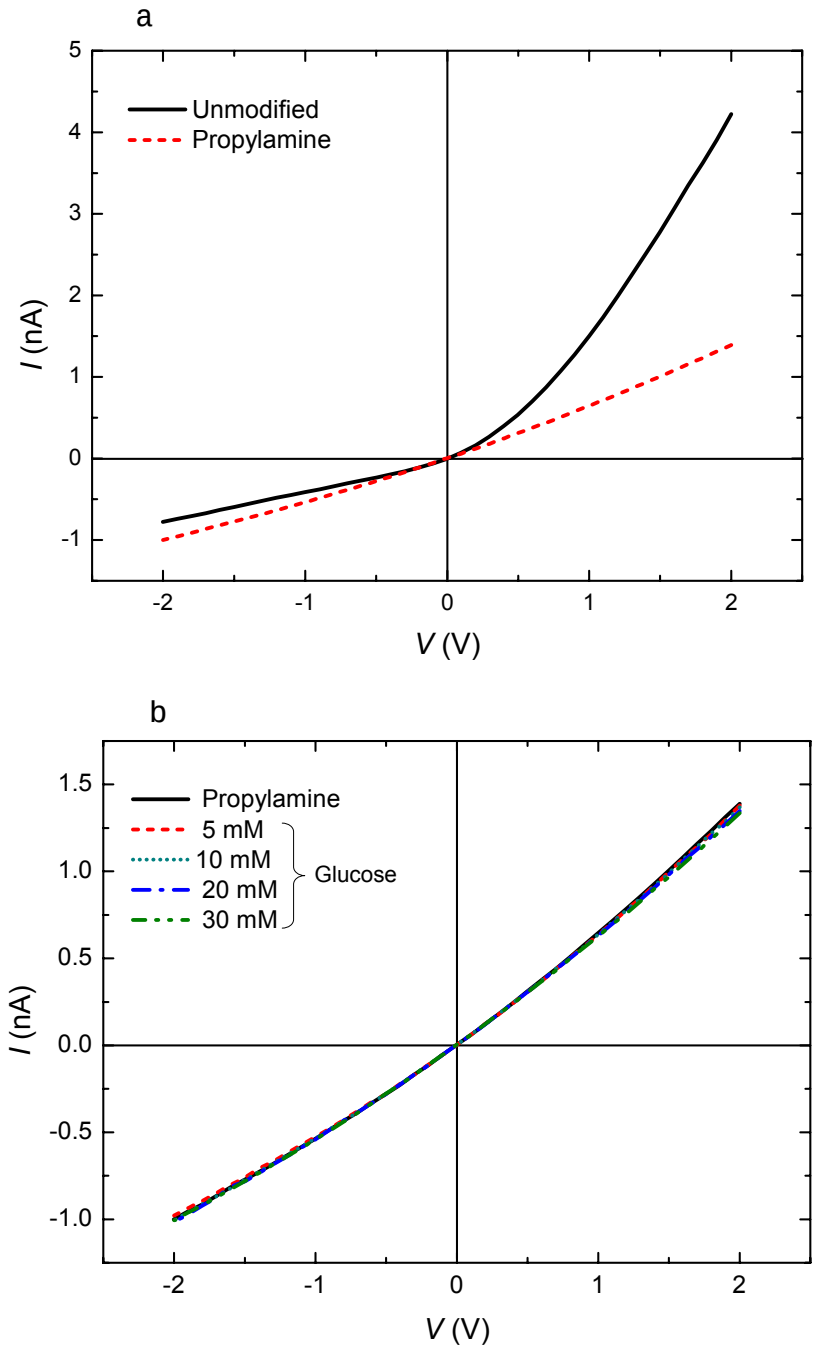

Figure 4.32: Current–voltage characteristics in 0.1 KCl at pH 7 of a nanopore having $D = 570 \pm 50$ nm and $d = 12 \pm 1$ nm; (a) propylamine-modified nanopore (dashed red); (b) propylamine-modified nanopore with different concentrations of glucose.

4.7.3 Recognition of monosaccharides

For the determination of the detection limit of these sensors, the concentration dependence of the complexation between two common monosaccharides (glucose and fructose) and boronic acid was studied. For these experiments, 0.1 M KCl solution (pH 7) containing glucose or fructose at different concentrations was filled into a BA-modified nanopore, and the *I–V* characteristics were recorded. The results are shown in Figure 4.33a and b for glucose and fructose complexation, respectively. Obviously, the addition of saccharides induces the changes in rectification behavior of the ion current with the concentration range from 3 to 30 mM. This range covers the physiologically normal region of glucose concentration in human blood (4.4–6.1 mM) [123]. The observed rectifying current originates from the binding between boronic acid and 1,2-diols of glucose and fructose to form five-membered rings of boronate anions. It has to be noted that both uncharged and charged forms of boronic acid (Figure 4.29) reversibly bind with diols in saccharides to generate uncharged trigonal boronic acid ester and negatively charged tetrahedral boronate ester, respectively. However, the tetrahedral ester structure is thermodynamically more stable than the trigonal one, and therefore, the pore surface is negatively charged. It is also important to mention that ion current rectification is strongly dependent on the surface charge of the pore walls, which can be regulated by the saccharide concentration. In both cases, an increase in concentration induces stronger ion current rectification. This can be explained by the fact that an increase in saccharide concentration leads to a higher concentration of boronate anions (**4**) formed and thereby an increase of negative charge density on the pore surface. When the nanopore was exposed to 30 mM glucose solution, f_{rec} increased from ~1.2 to ~2.9. For fructose, f_{rec} was enhanced from ~ 1 to ~5.8.

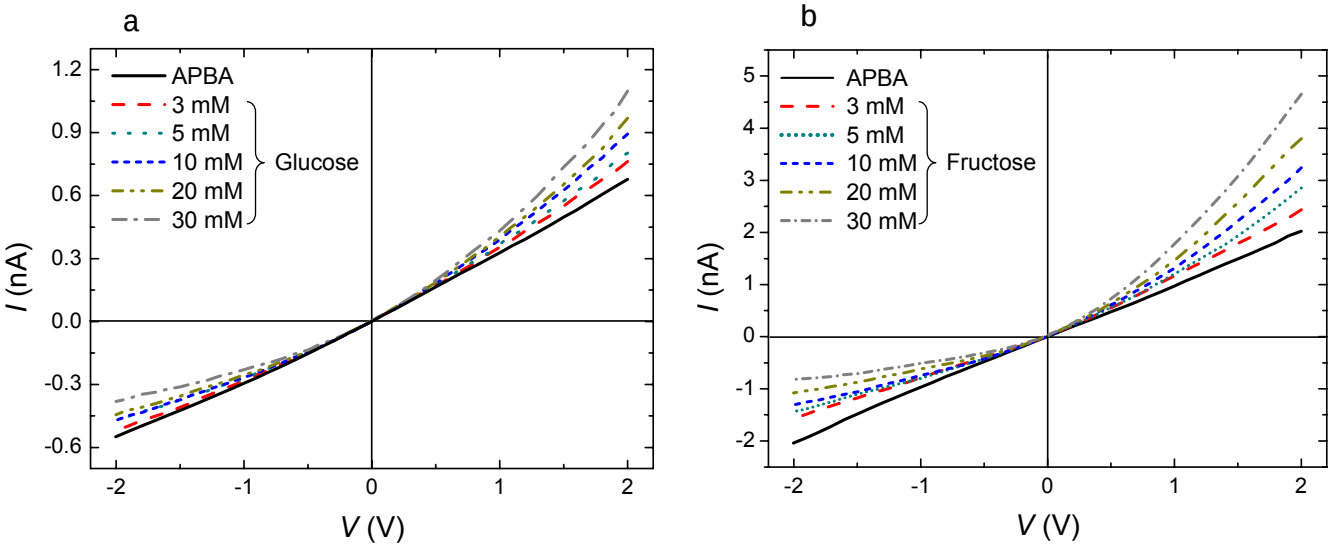

Figure 4.33: Current–voltage characteristics for 0.1 M KCl solution at pH 7 in the case of (a) glucose (D = 530 ± 40 nm and d = 8 ± 1 nm) and (b) fructose (D = 670 ± 60 nm and d = 20 ± 2 nm).

For the comparison of binding ability between glucose and fructose, we assume that the modification of APBA on pore walls affects neither the geometry nor the opening of the nanopore tip significantly. Then, the rectification behavior or rectification degree is governed by surface charge on the pore walls. The binding efficiency of a saccharide is defined as follows:

$$\text{Binding efficiency}\,(\%) = \frac{f_{rec}\,(\text{binding}) - f_{rec}\,(\text{APBA})}{f_{rec}\,(\text{COOH}) - f_{rec}\,(\text{APBA})} \text{ x } 100$$

where f_{rec}(binding) is the rectification efficiency of the APBA-modified nanopore upon the addition of saccharide, f_{rec}(APBA) denotes this efficiency of the APBA-modified nanopore, and f_{rec}(COOH) is the one of the unmodified nanopore. From this definition, the binding efficiency is 0% when f_{rec}(binding) is equal to f_{rec}(APBA), and it amounts to 100% when f_{rec}(binding) is equal to f_{rec}(COOH). The relation between binding efficiency and saccharide concentration is depicted in Figure 4.34, and it is also obvious that the binding efficiency is proportional to the saccharide concentration. Additionally, the binding efficiency of fructose is higher than that of glucose at the same concentration. This means that the binding affinity of fructose with boronic acid is higher than that of glucose. At a concentration of 30 mM, the binding efficiency of fructose is ~75%, which is more than twice when compared to glucose (~35%). These results are in agreement with the reported values that the binding constant of fructose in aqueous solution is much higher than that of glucose [115, 124]. Even among the monosaccharides, fructose possesses the highest association constant because a five-membered ring with cis-1,2-diols of fructose is usually the most stable one [125]. The explanation could be derived from the fact that pK_a of the phenylboronate ester molecules of d-fructose (4.6) is lower than that of d-glucose (6.8) [122]. Therefore, at pH 7, more boronate ester molecules of fructose are formed as compared to those of glucose at the same concentration.

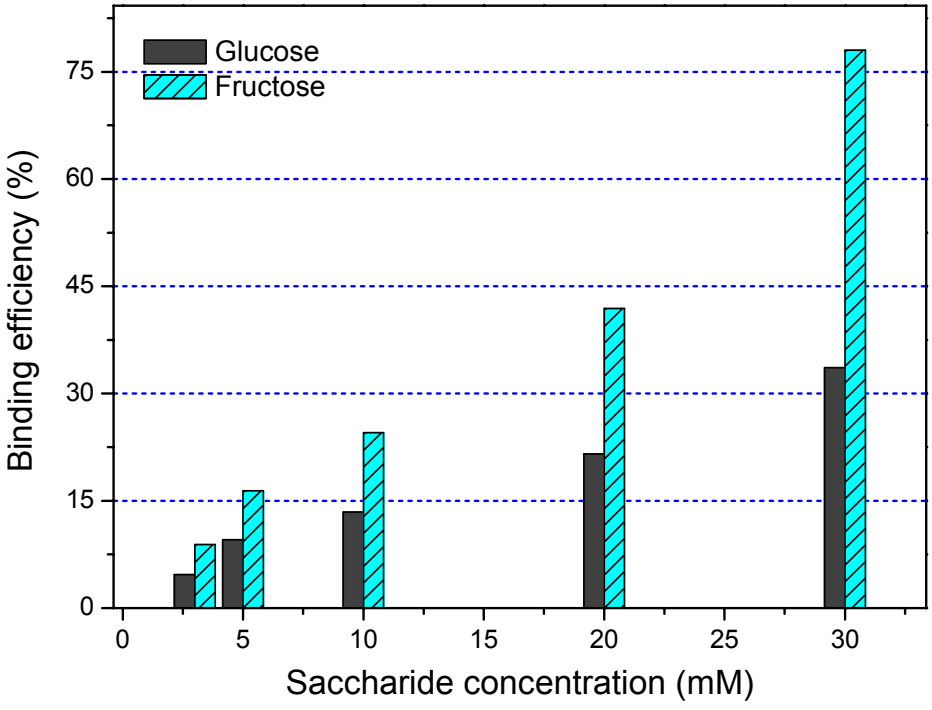

Figure 4.34: Binding efficiency of glucose and fructose as a function of concentration.

4.7.4 Recognition of glycoproteins

In this study, the sensing platform can also be employed for glycoprotein recognition. Glycoproteins are key constituents in varied cellular processes in living organisms [126]. The recognition of glycoprotein is particularly important because changes in expression and abundance of glycoproteins in cellular environments are often associated with tumor proliferation. Ovalbumin was chosen as the analyte for sensing experiments of glycoprotein in BA-nanopores. The ovalbumin is constituted of 385 amino acids with the glycosylation site of single carbohydrate moiety [127]. In the sensing experiments, the nanopores were exposed to 0.1 M KCl solutions at pH 7 containing different concentrations of ovalbumin. The resulting *I–V* characteristics are shown in Figure 4.35a. The binding between boronic acid and ovalbumin to form negatively charged boronate ester was observed at protein concentration of 50 nM. The indication is the increased ion current rectification as compared to the linear *I–V* characteristic of the BA-nanopore. The rectification degree (1 V) vs. ovalbumin concentration relation is displayed in Figure 4.35b. As expected, when the protein concentration goes up to 500 nM, the rectification increases accordingly. However, further increase in concentration leads to the reduction of f_{rec} which is due to a lowering of the ionic current at positive voltage (Figure 4.35a). Increasing the glycoprotein concentration from 50 nM to 1 μM dropped the ion current of the nanopore at +1 V from 0.33 to 0.17 nA (~50%). This originates from the fact that ovalbumin is a large biomolecule, which has a molecular weight of approximately 44 kDa and a hydrodynamic radius of ~3 nm [128]. Therefore, the attachment of ovalbumin molecules to the pore wall was expected to diminish the effective pore opening.

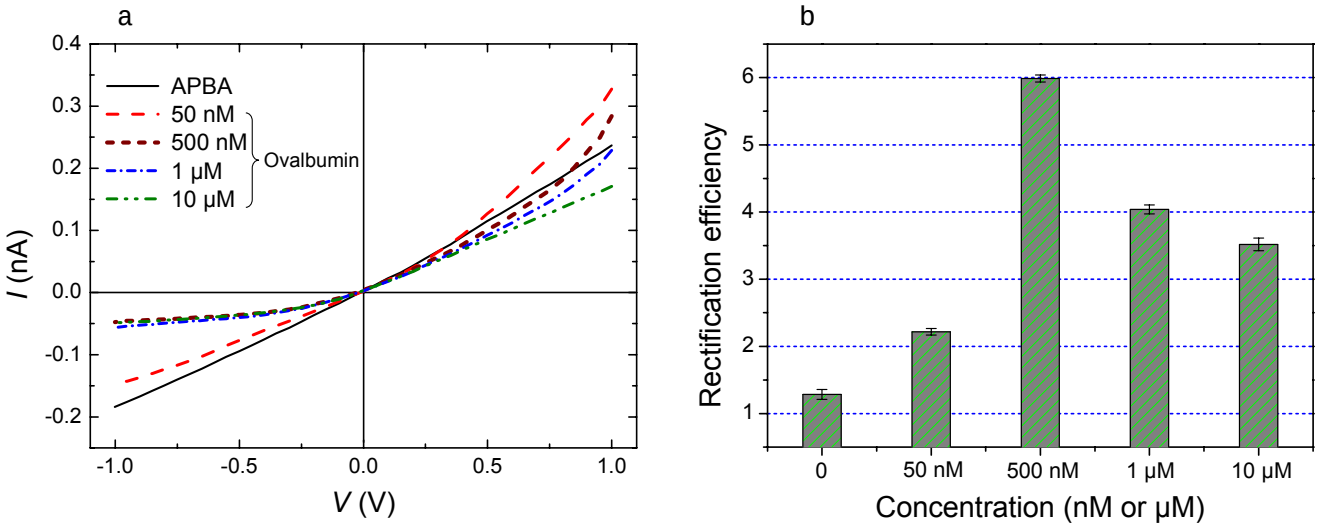

Figure 4.35: (a) *I–V* curves in glycoprotein sensing experiments in a conical nanopore with tip diameter 8 ± 1 nm and base diameter 400 ± 30 nm; (b) the rectification degree of this nanopore at 1 V.

A supplement experiment has been performed to confirm the above explanation. For this purpose, a cylindrical pore was used for the saccharide–boronic acid complexation process. The fabrication of cylindrical nanopores is shown in Section 3.2. For a single cylindrical nanopore, the *I–V* curve exhibits ohmic behavior (no rectification of ionic current). This means that the current flow through the nanopore is governed by the resistance of the pore which is inversely proportional to the effective

opening. Figure 4.36a shows the *I–V* curves of a cylindrical nanopore with various concentrations of ovalbumin in 0.1 M KCl solutions at pH 7. Furthermore, Figure 4.36b presents the corresponding pore conductance upon the addition of ovalbumin which is calculated from the slopes of the curves in Figure 4.36a. It is shown that by increasing the ovalbumin concentration to 500 nM or higher, the pore conductance significantly decreased. This observation suggests that the resistance of the pore increases upon the addition of glycoprotein, indicating that the binding of carbohydrate moieties with boronic acid on the pore surface leads to a lowering in the effective diameter.

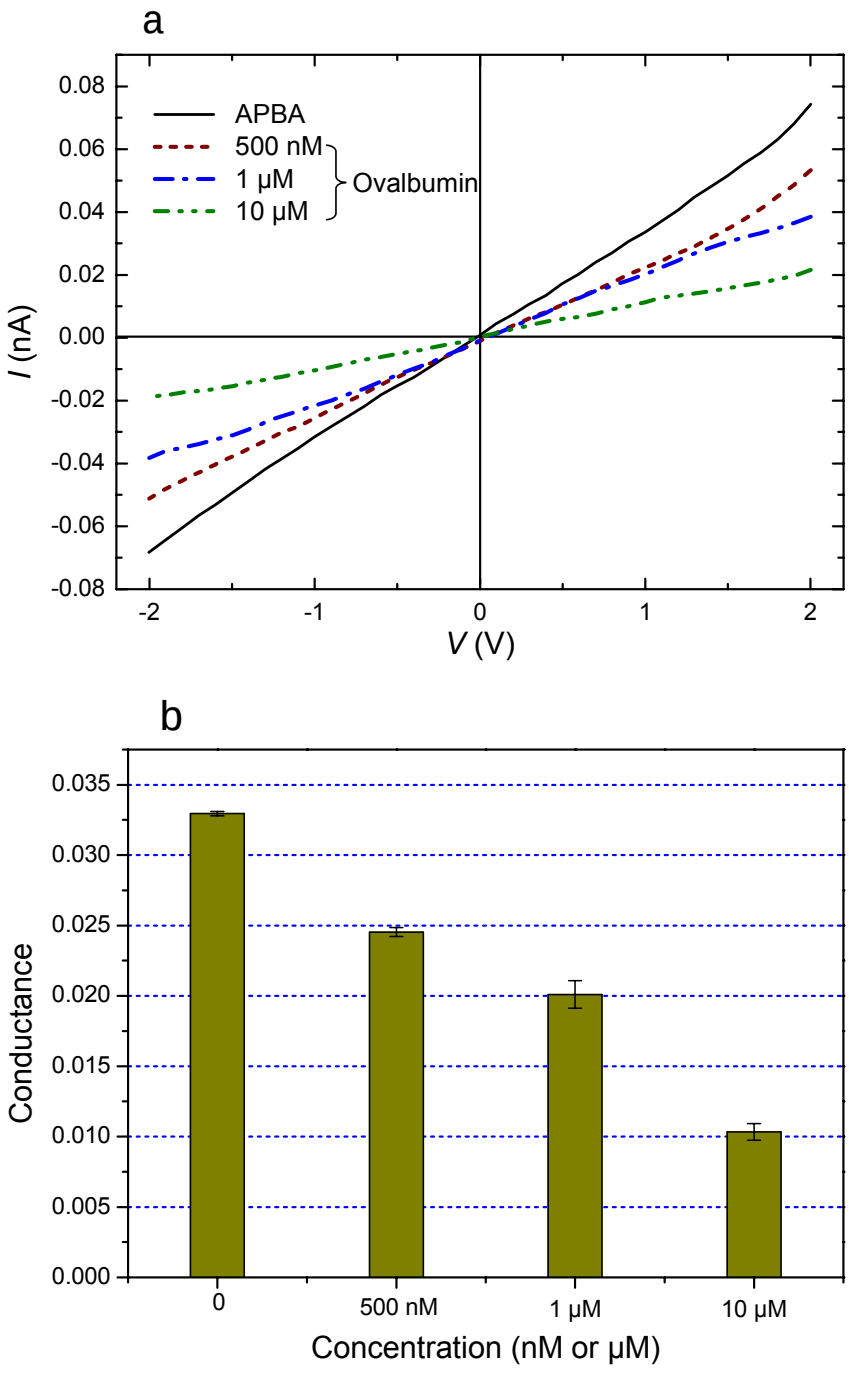

Figure 4.36: *I–V* curves in glycoprotein sensing experiments using a cylindrical nanopore with diameter 13 ± 1 nm; (a) *I–V* curves at different concentrations of ovalbumin and (b) nanopore conductance as a function of ovalbumin concentration.

Negative control experiments have been performed to be sure that the blocking of nanopores does not originate from the physical adsorption of protein on the pore surface. Unmodified cylindrical and conical nanopores were used for the *I–V* curves in the same conditions of electrolyte with different concentrations of ovalbumin. The results in Figure 4.37 show that in the presence of ovalbumin the ion current in both cases (cylindrical and conical) does not change as compared to the native nanopores. Only at high concentration (10 μM), a slight decrease in the ion current was observed. Therefore, it could be concluded that the decrease in current Figure 4.35 and Figure 4.36) is due to the binding of ovalbumin with boronic acid leading to a lowered effective diameter.

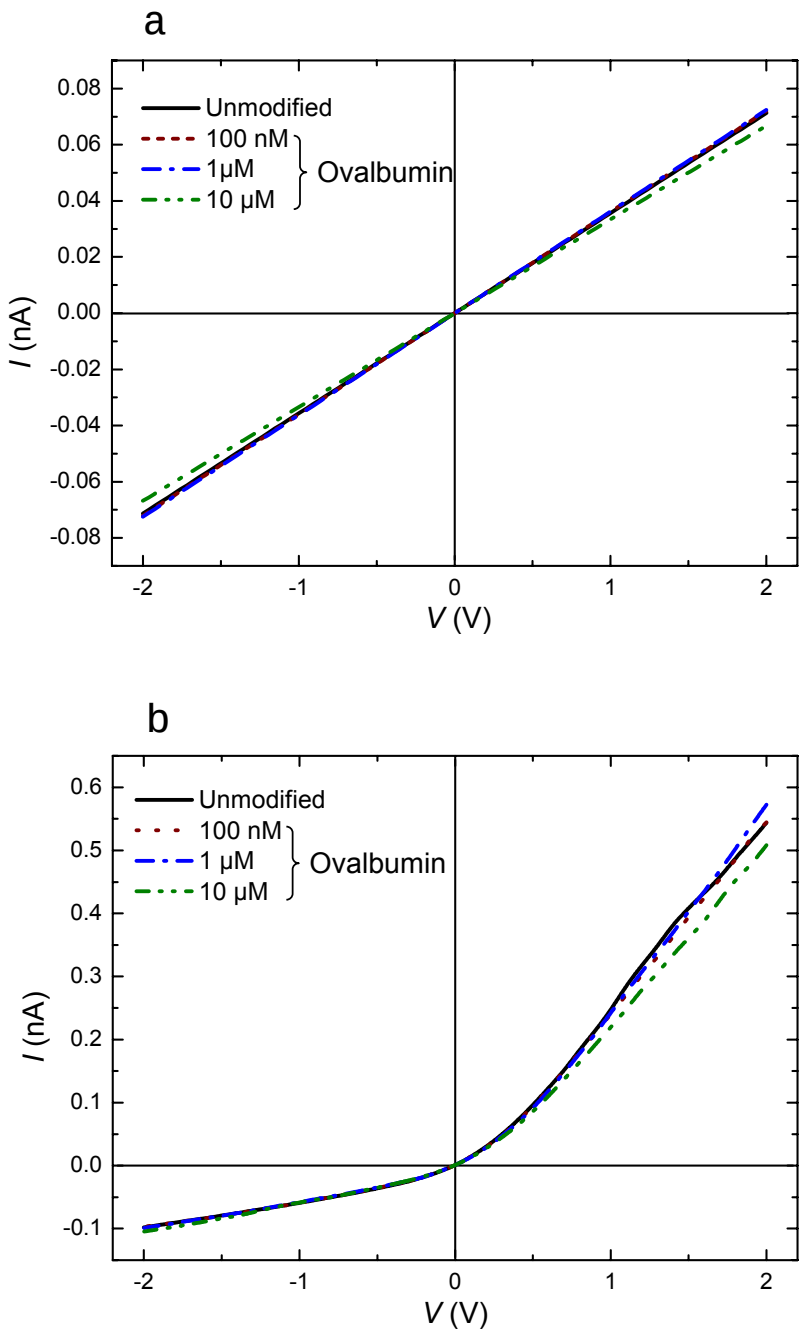

Figure 4.37: *I–V* curves in glycoprotein control experiments using (a) a cylindrical nanopore with diameter 12 ± 1 nm and (b) a conical nanopore with tip diameter 9 ± 1 nm and base diameter 450 ± 40 nm.

Briefly, we have demonstrated an easy and robust method to fabricate saccharide and glycoprotein sensors based on track-etched nanopores in polymer membranes. At neutral pH, conical pores rectify the ion current due to the presence of carboxylate groups. After modification, the rectification characteristic of the pores disappeared which confirms the successful immobilization of neutral APBA moieties. In the recognition step, the addition of saccharides led to the conversion of uncharged boronic acid into negatively charged boronate anion ester moieties, and subsequent rectification of the ion current was observed. The saccharide–boronic acid complex onto the pore walls was found to be reversible. We have also demonstrated that the rectification degree is enhanced by increasing the concentration of glucose/fructose in the working electrolyte solution. It has been shown that the binding capability of fructose was higher than that of glucose molecules. Furthermore, we have also shown that the presence of ovalbumin (glycoprotein) also reduced the effective diameter of the pore. Based on these experimental results, we envision that the presented sensing platform can be further applied effectively to cell cultures.

5 Summary and outlook

This thesis demonstrated the controlled fabrication of nanopores in heavy ion tracked polymeric membranes. The experimental details provided a guide to select nanoporous membranes for separation and purification, biosensing and nanofluidic devices.

Cylindrical and conical nanopores (both single and multi-nanopores) were fabricated using symmetric and asymmetric track-etching techniques, respectively. As-prepared nanopores contain carboxylic groups (–COOH) on the surface and pore walls which were generated during ion irradiation and etching processes. These groups were chemically coupled with organic molecules having primary amine in their backbone via carbodiimide coupling chemistry to manipulate the chemical functionalities of the nanopore surface for the control of pore transport properties. The modification with diamine and polyethyleneimine (PEI) reversed the surface charge polarity from negative ($–COO^-$) to positive ($–NH_3^+$). 3-aminophenylboronic acid (APBA) moieties were attached to the pore walls for the detection of saccharide and glycoprotein molecules.

The experimental results demonstrated the permselective properties of the track-etched nanopores. The as-prepared nanopores are cation-selective due to the presence of ionized $–COO^-$ groups. On the other hand, ethylenediamine-modified nanopores showed anion-selectivity because protonated amine groups import positive charge polarity to the pore surface. The driving forces underlying these properties are the electrical double layer (EDL), generated due to the accumulation of counter-ions near the charged pore surface, and the electrostatic interactions between the guest molecules and the pore walls. The charged nanopores prefer to transport the oppositely charged analytes, showing higher flux in the optical measurements. The mass-transport experiments were performed with organic analytes (MV^{2+} and NDS^{2-}) and biomolecules (BSA, lysozyme and BHb). For biomolecules, in addition to their charge, the size and hydrophobic properties of the molecules also contribute to the molecular flux of each analyte.

A systematic study of different parameters of the nanopore performance was carried out to find the optimal conditions for high selectivity and high throughput for practical applications. Namely, increasing pore density will increase the molecular fluxes of both positively and negatively charged species. Lower pore diameter would lead to higher selectivity but lower molecular flux. By decreasing the ionic strength of the solution to some extent, both molecular flux and nanopore selectivity are higher. By proper application of an electric field, electrokinetic phenomena will also help to improve the nanopore performance.

A theoretical model based on the Poisson and Nernst-Planck (PNP) equations is used to describe the ionic transport through a single cylindrical nanopore. The model has been extended by taking into account the presence of H^+ and OH^- ions in the solutions to describe the nanopore ionic transport properties within a wide range of pH values. The extended model was useful not only for the estimation of pore surface charge density but also for the determination of the pK_a value. The experimental and theoretical results showed that the nanopore charge density ranges from 0.9 to 1.3 e/nm^2. The estimated pK_a of the pore surface –COOH groups was $\sim$ 5.1.

The fabrication of an anion controlled molecular gate based on track-etched nanopores modified with polyethyleneimine (PEI) is also demonstrated. The ionic/molecular transport can be accurately

controlled by manipulating the adenosine 5´-triphosphate (ATP) concentration in the external solution. The “on/off” switching is chemically actuated via ATP in the external environment with which the molecular gate is opened and closed. The functioning is based on the electrostatical/hydrogen-bonding interactions of ATP with amine groups of PEI which in turn control the ion flux through the nanopores.

For the future activities, it is planned to study the transport experiments of the analytes in different nanopore geometries, e.g., conical and biconical nanopores, and compared with the results from cylindrical nanopores to adjust the parameters for practical applications. The fabrication of nanopores in thinner PET membranes could be also very interesting for higher throughput.

Another interesting application of track-etched nanoporous PET membranes is the possibility to discriminate enantiomers, e.g., drug molecules. This can be successful by immobilizing the pore walls with cyclodextrin, a chiral selector known for its selective interactions between enantiomers.

6 References

[1] B. Hille, *Ionic channels of excitable membranes*, 3rd ed., Sinauer Associates Inc.: Sunderland, MA, 2001.

[2] A. Alcaraz, E.M. Nestorovich, M. Aguilella-Arzo, V.M. Aguilella, S.M. Bezrukov, Salting out the ionic selectivity of a wide channel: The asymmetry of OmpF. *Biophysical Journal* **2004**, *87*, 943-957.

[3] A. Alcaraz, P. Ramirez, E. Garcia-Gimenez, M.L. Lopez, A. Andrio, V.M. Aguilella, A pH-tunable nanofluidic diode: Electrochemical rectification in a reconstituted single ion channel. *Journal of Physical Chemistry B* **2006**, *110*, 21205-21209.

[4] C. Dekker, Solid-state nanopores. *Nature Nanotechnology* **2007**, *2*, 209-215.

[5] Z.S. Siwy, S. Howorka, Engineered voltage-responsive nanopores. *Chemical Society Reviews* **2010**, *39*, 1115-1132.

[6] M. Ali, V. Bayer, B. Schiedt, R. Neumann, W. Ensinger, Fabrication and functionalization of single asymmetric nanochannels for electrostatic/hydrophobic association of protein molecules. *Nanotechnology* **2008**, *19*, 485711.

[7] Z. Siwy, L. Trofin, P. Kohli, L.A. Baker, C. Trautmann, C.R. Martin, Protein biosensors based on biofunctionalized conical gold nanotubes. *Journal of the American Chemical Society* **2005**, *127*, 5000-5001.

[8] C.C. Harrell, Y. Choi, L.P. Horne, L.A. Baker, Z.S. Siwy, C.R. Martin, Resistive-pulse DNA detection with a conical nanopore sensor. *Langmuir* **2006**, *22*, 10837-10843.

[9] B. Yameen, M. Ali, R. Neumann, W. Ensinger, W. Knoll, O. Azzaroni, Synthetic Proton-Gated Ion Channels via Single Solid-State Nanochannels Modified with Responsive Polymer Brushes. *Nano Letters* **2009**, *9*, 2788–2793.

[10] X. Hou, F. Yang, L. Li, Y.L. Song, L. Jiang, D.B. Zhu, A Biomimetic Asymmetric Responsive Single Nanochannel. *Journal of the American Chemical Society* **2010**, *132*, 11736-11742.

[11] M. Ali, S. Mafe, P. Ramirez, R. Neumann, W. Ensinger, Logic Gates Using Nanofluidic Diodes Based on Conical Nanopores Functionalized with Polyprotic Acid Chains. *Langmuir* **2009**, *25*, 11993-11997.

[12] E.B. Kalman, I. Vlassiouk, Z.S. Siwy, Nanofluidic bipolar transistors. *Advanced Materials* **2008**, *20*, 293-297.

[13] M.L. Kovarik, S.C. Jacobson, Nanofluidics in Lab-on-a-Chip Devices. *Analytical Chemistry* **2009**, *81*, 7133-7140.

[14] A. Piruska, M. Gong, J.V. Sweedler, P.W. Bohn, Nanofluidics in chemical analysis. *Chemical Society Reviews* **2010**, *39*, 1060-1072.

[15] H.G. Zhang, X.D. Yu, P.V. Braun, Three-dimensional bicontinuous ultrafast-charge and -discharge bulk battery electrodes. *Nature Nanotechnology* **2011**, *6*, 277-281.

[16] P.W. Bohn, Nanoscale Control and Manipulation of Molecular Transport in Chemical Analysis. *Annual Review of Analytical Chemistry* **2009**, *2*, 279-296.

[17] K.M. Zhou, J.M. Perry, S.C. Jacobson, Transport and Sensing in Nanofluidic Devices. *Annual Review of Analytical Chemistry* **2011**, *4*, 321-341.

[18] H. Bayley, P.S. Cremer, Stochastic sensors inspired by biology. *Nature* **2001**, *413*, 226-230.

[19] C. Wei, A.J. Bard, S.W. Feldberg, Current rectification at quartz nanopipet electrodes. *Analytical Chemistry* **1997**, *69*, 4627-4633.

[20] P. Apel, Track etching technique in membrane technology. *Radiation Measurements* **2001**, *34*, 559-566.

[21] J.D. Uram, K. Ke, A.J. Hunt, M. Mayer, Submicrometer pore-based characterization and quantification of antibody-virus interactions. *Small* **2006**, *2*, 967-972.

[22] N. Patterson, D.P. Adams, V.C. Hodges, M.J. Vasile, J.R. Michael, P.G. Kotula, Controlled fabrication of nanopores using a direct focused ion beam approach with back face particle detection. *Nanotechnology* **2008**, *19*, 235304.

[23] H.M. Kim, M.H. Lee, K.B. Kim, Theoretical and experimental study of nanopore drilling by a focused electron beam in transmission electron microscopy. *Nanotechnology* **2011**, *22*, 275303.

[24] A.J. Storm, J.H. Chen, X.S. Ling, H.W. Zandbergen, C. Dekker, Fabrication of solid-state nanopores with single-nanometre precision. *Nature Materials* **2003**, *2*, 537-540.

[25] R. Karnik, K. Castelino, R. Fan, P. Yang, A. Majumdar, Effects of biological reactions and modifications on conductance of nanofluidic channels. *Nano Letters* **2005**, *5*, 1638-1642.

[26] J.P. Fu, R.B. Schoch, A.L. Stevens, S.R. Tannenbaum, J.Y. Han, A patterned anisotropic nanofluidic sieving structure for continuous-flow separation of DNA and proteins. *Nature Nanotechnology* **2007**, *2*, 121-128.

[27] J.M. Perry, K.M. Zhou, Z.D. Harms, S.C. Jacobson, Ion Transport in Nanofluidic Funnels. *ACS Nano* **2010**, *4*, 3897-3902.

[28] J.T. Mannion, C.H. Reccius, J.D. Cross, H.G. Craighead, Conformational analysis of single DNA molecules undergoing entropically induced motion in nanochannels. *Biophysical Journal* **2006**, *90*, 4538-4545.

[29] A. Holtzel, U. Tallarek, Ionic conductance of nanopores in microscale analysis systems: Where microfluldics meets nanofluidics. *Journal of Separation Science* **2007**, *30*, 1398-1419.

[30] R.B. Schoch, J.Y. Han, P. Renaud, Transport phenomena in nanofluidics. *Reviews of Modern Physics* **2008**, *80*, 839-883.

[31] D. Stein, M. Kruithof, C. Dekker, Surface-charge-governed ion transport in nanofluidic channels. *Physical Review Letters* **2004**, *93*, 035901.

[32] R.B. Schoch, H. van Lintel, P. Renaud, Effect of the surface charge on ion transport through nanoslits. *Physics of Fluids* **2005**, *17*, 100604.

[33] R.J. Hunter, *Zeta Potential in Colloid Science: Principles and Applications*, Academic Press Inc.: London, 1981.

[34] L.-J. Cheng, *Ion and molecule transport in nanochannels*, PhD thesis, The University of Michigan, 2008.

[35] K.P. Singh, M. Kumar, Effect of surface charge density and electro-osmotic flow on ionic current in a bipolar nanopore fluidic diode. *Journal of Applied Physics* **2011**, *110*, 084322.

[36] A. Plecis, R.B. Schoch, P. Renaud, Ionic transport phenomena in nanofluidics: Experimental and theoretical study of the exclusion-enrichment effect on a chip. *Nano Letters* **2005**, *5*, 1147-1155.

[37] Z. Yuan, A.L. Garcia, G.P. Lopez, D.N. Petsev, Electrokinetic transport and separations in fluidic nanochannels. *Electrophoresis* **2007**, *28*, 595-610.

[38] G. Schmid, Electrochemistry of capillary systems with narrow pores. I. Overview. *Journal of Membrane Science* **1998**, *150*, 151-157.

[39] M.H. Oddy, J.G. Santiago, A method for determining electrophoretic and electroosmotic mobilities using AC and DC electric field particle displacements. *Journal of Colloid and Interface Science* **2004**, *269*, 192-204.

[40] S. Howorka, Z. Siwy, Nanopore analytics: sensing of single molecules. *Chemical Society Reviews* **2009**, *38*, 2360-2384.

[41] H. Bayley, O. Braha, L.Q. Gu, Stochastic sensing with protein pores. *Advanced Materials* **2000**, *12*, 139-142.

[42] D. Branton, D.W. Deamer, A. Marziali, H. Bayley, S.A. Benner, T. Butler, M. Di Ventra, S. Garaj, A. Hibbs, X.H. Huang, S.B. Jovanovich, P.S. Krstic, S. Lindsay, X.S.S. Ling, C.H. Mastrangelo, A. Meller, J.S. Oliver, Y.V. Pershin, J.M. Ramsey, R. Riehn, G.V. Soni, V. Tabard-Cossa, M. Wanunu, M. Wiggin, J.A. Schloss, The potential and challenges of nanopore sequencing. *Nature Biotechnology* **2008**, *26*, 1146-1153.

[43] J. Li, D. Stein, C. McMullan, D. Branton, M.J. Aziz, J.A. Golovchenko, Ion-beam sculpting at nanometre length scales. *Nature* **2001**, *412*, 166-169.

[44] H.B. George, D.P. Hoogerheide, C.S. Madi, D.C. Bell, J.A. Golovchenko, M.J. Aziz, Ion-sculpting of nanopores in amorphous metals, semiconductors, and insulators. *Applied Physics Letters* **2010**, *96*, 263111.

[45] S. Umehara, N. Pourmand, C.D. Webb, R.W. Davis, K. Yasuda, M. Karhanek, Current rectification with poly-L-lysine-coated quartz nanopipettes. *Nano Letters* **2006**, *6*, 2486-2492.

[46] M. Karhanek, J.T. Kemp, N. Pourmand, R.W. Davis, C.D. Webb, Single DNA molecule detection using nanopipettes and nanoparticles. *Nano Letters* **2005**, *5*, 403-407.

[47] R.L.P. Fleischer, P. B.; Walker, R. M., *Nuclear tracks in solids: Principles and applications*, Berkeley, University of California Press, 1975.

[48] P.Y. Apel, Y.E. Korchev, Z. Siwy, R. Spohr, M. Yoshida, Diode-like single-ion track membrane prepared by electro-stopping. *Nuclear Instruments & Methods in Physics Research Section B-Beam Interactions with Materials and Atoms* **2001**, *184*, 337-346.

[49] A. Mara, Z. Siwy, C. Trautmann, J. Wan, F. Kamme, An asymmetric polymer nanopore for single molecule detection. *Nano Letters* **2004**, *4*, 497-501.

[50] B. Schiedt, K. Healy, A.P. Morrison, R. Neumann, Z. Siwy, Transport of ions and biomolecules through single asymmetric nanopores in polymer films. *Nuclear Instruments & Methods in Physics Research Section B-Beam Interactions with Materials and Atoms* **2005**, *236*, 109-116.

[51] M. Ali, B. Schiedt, R. Neumann, W. Ensinger, Biosensing with Functionalized Single Asymmetric Polymer Nanochannels. *Macromolecular Bioscience* **2010**, *10*, 28-32.

[52] M. Ali, *Functionalization and Application of Ion Track-Etched Nanochannels in Polymer Membranes*. PhD Thesis, Technischen Universität Darmstadt, 2009.

[53] S.P. Adiga, C.M. Jin, L.A. Curtiss, N.A. Monteiro-Riviere, R.J. Narayan, Nanoporous membranes for medical and biological applications. *Wiley Interdisciplinary Reviews-Nanomedicine and Nanobiotechnology* **2009**, *1*, 568-581.

[54] P. Stroeve, N. Ileri, Biotechnical and other applications of nanoporous membranes. *Trends in Biotechnology* **2011**, *29*, 259-266.

[55] N. Itoh, K. Kato, T. Tsuji, M. Hongo, Preparation of a tubular anodic aluminum oxide membrane. *Journal of Membrane Science* **1996**, *117*, 189-196.

[56] P. Gu, H. Miao, Z.T. Liu, X.P. Wu, J.H. Zhao, Investigation of elastic modulus of nanoporous alumina membrane. *Journal of Materials Science* **2004**, *39*, 3369-3373.

[57] X.Y. Sun, F.Q. Xu, Z.M. Li, W.H. Zhang, Cyclic voltammetry for the fabrication of high dense silver nanowire arrays with the assistance of AAO template. *Materials Chemistry and Physics* **2005**, *90*, 69-72.

[58] S. Kipke, G. Schmid, Nanoporous alumina membranes as diffusion controlling systems. *Advanced Functional Materials* **2004**, *14*, 1184-1188.

[59] I. Vlassiouk, A. Krasnoslobodtsev, S. Smirnov, M. Germann, "Direct" detection and separation of DNA using nanoporous alumina filters. *Langmuir* **2004**, *20*, 9913-9915.

[60] H.D. Tong, H.V. Jansen, V.J. Gadgil, C.G. Bostan, E. Berenschot, C.J.M. van Rijn, M. Elwenspoek, Silicon nitride nanosieve membrane. *Nano Letters* **2004**, *4*, 283-287.

[61] C.C. Striemer, T.R. Gaborski, J.L. McGrath, P.M. Fauchet, Charge- and size-based separation of macromolecules using ultrathin silicon membranes. *Nature* **2007**, *445*, 749-753.

[62] R. Xie, L.Y. Chu, W.M. Chen, W. Xiao, H.D. Wang, J.B. Qu, Characterization of microstructure of poly (N-isopropylacrylamide)-grafted polycarbonate track-etched membranes prepared by plasma-graft pore-filling polymerization. *Journal of Membrane Science* **2005**, *258*, 157-166.

[63] J.R. Ku, P. Stroeve, Protein diffusion in charged nanotubes: "On-Off" behavior of molecular transport. *Langmuir* **2004**, *20*, 2030-2032.

[64] M. Wirtz, S.F. Yu, C.R. Martin, Template synthesized gold nanotube membranes for chemical separations and sensing. *Analyst* **2002**, *127*, 871-879.

[65] R. Spohr, *Ion Tracks and Microtechnology, Principles and Applications*, Vieweg & Sohn Verlagsgesellschaft mbH, Braunschweig, 1990.

[66] D. Severin, Study of the degradation process of polyimide induced by high energetic ion irradiation. PhD thesis, Philipps-Universität Marburg, 2008.

[67] The Stopping and Range of Ions in Matter. http://www.srim.org/index.htm.

[68] C. Trautmann, S. Bouffard, R. Spohr, Etching threshold for ion tracks in polyimide. *Nuclear Instruments & Methods in Physics Research Section B-Beam Interactions with Materials and Atoms* **1996**, *116*, 429-433.

[69] Z. Zhu, Y. Maekawa, Q. Liu, M. Yoshida, Influence of UV light illumination on latent track structure in PET. *Nuclear Instruments & Methods in Physics Research Section B-Beam Interactions with Materials and Atoms* **2005**, *236*, 61-67.

[70] D.M. Wang, T.H. Youn, T.T. Wu, J.Y. Lai, Effect of sputter coating on the observation of polymeric membrane structure. *Journal of the Chinese Institute of Chemical Engineers* **2001**, *32*, 13-22.

[71] B. Schiedt, Characterization and application of ion track-etched nanopores. PhD Thesis, The Ruperto-Carola University of Heidelberg, 2007.

[72] M. Ali, B. Yameen, R. Neumann, W. Ensinger, W. Knoll, O. Azzaroni, Biosensing and Supramolecular Bioconjugation in Single Conical Polymer Nanochannels. Facile Incorporation of Biorecognition Elements into Nanoconfined Geometries. *Journal of the American Chemical Society* **2008**, *130*, 16351-16357.

[73] I. Vlassiouk, T.R. Kozel, Z.S. Siwy, Biosensing with Nanofluidic Diodes. *Journal of the American Chemical Society* **2009**, *131*, 8211-8220.

[74] I. Vlassiouk, S. Smirnov, Z. Siwy, Nanofluidic ionic diodes. Comparison of analytical and numerical solutions. *ACS Nano* **2008**, *2*, 1589-1602.

[75] S.B. Lee, C.R. Martin, Electromodulated molecular transport in gold-nanotube membranes. *Journal of the American Chemical Society* **2002**, *124*, 11850-11851.

[76] K.B. Jirage, J.C. Hulteen, C.R. Martin, Nanotubule-based molecular-filtration membranes. *Science* **1997**, *278*, 655-658.

[77] S.B. Lee, C.R. Martin, pH-switchable, ion-permselective gold nanotubule membrane based on chemisorbed cysteine. *Analytical Chemistry* **2001**, *73*, 768-775.

[78] C.R. Martin, M. Nishizawa, K. Jirage, M. Kang, Investigations of the transport properties of gold nanotubule membranes. *Journal of Physical Chemistry B* **2001**, *105*, 1925-1934.

[79] S.B. Lee, D.T. Mitchell, L. Trofin, T.K. Nevanen, H. Soderlund, C.R. Martin, Antibody-based bio-nanotube membranes for enantiomeric drug separations. *Science* **2002**, *296*, 2198-2200.

[80] K.Y. Chun, P. Stroeve, Protein transport in nanoporous membranes modified with self-assembled monolayers of functionalized thiols. *Langmuir* **2002**, *18*, 4653-4658.

[81] E.N. Savariar, K. Krishnamoorthy, S. Thayumanavan, Molecular discrimination inside polymer nanotubules. *Nature Nanotechnology* **2008**, *3*, 112-117.

[82] F.H.J. van der Heyden, D.J. Bonthuis, D. Stein, C. Meyer, C. Dekker, Power generation by pressure-driven transport of ions in nanofluidic channels. *Nano Letters* **2007**, *7*, 1022-1025.

[83] Z. Siwy, E. Heins, C.C. Harrell, P. Kohli, C.R. Martin, Conical-nanotube ion-current rectifiers: The role of surface charge. *Journal of the American Chemical Society* **2004**, *126*, 10850-10851.

[84] L.E. Ermakova, M.P. Sidorova, M.E. Bezrukova, Filtration and electrokinetic characteristics of track membranes. *Colloid Journal* **1998**, *60*, 705-712.

[85] H.U. Osmanbeyoglu, T.B. Hur, H.K. Kim, Thin alumina nanoporous membranes for similar size biomolecule separation. *Journal of Membrane Science* **2009**, *343*, 1-6.

[86] K.Y. Chun, S. Mafe, P. Ramirez, P. Stroeve, Protein transport through gold-coated, charged nanopores: Effects of applied voltage. *Chemical Physics Letters* **2006**, *418*, 561-564.

[87] J.Y. Han, J.P. Fu, R.B. Schoch, Molecular sieving using nanofilters: Past, present and future. *Lab on a Chip* **2008**, *8*, 23-33.

[88] Y.U. Moon, R.A. Curtis, C.O. Anderson, H.W. Blanch, J.M. Prausnitz, Protein-protein interactions in aqueous ammonium sulfate solutions. Lysozyme and bovine serum albumin (BSA). *Journal of Solution Chemistry* **2000**, *29*, 699-717.

[89] A. Adel, M. Nadia, O. Mohamed, G. Abdelhafidh, Study of thermally and chemically unfolded conformations of bovine serum albumin by means of dynamic light scattering. *Materials Science & Engineering C-Biomimetic and Supramolecular Systems* **2008**, *28*, 594-600.

[90] A. Valstar, W. Brown, M. Almgren, The lysozyme-sodium dodecyl sulfate system studied by dynamic and static light scattering. *Langmuir* **1999**, *15*, 2366-2374.

[91] J. Cervera, B. Schiedt, P. Ramirez, A Poisson/Nernst-Planck model for ionic transport through synthetic conical nanopores. *Europhysics Letters* **2005**, *71*, 35-41.

[92] J. Cervera, B. Schiedt, R. Neumann, S. Mafe, P. Ramirez, Ionic conduction, rectification, and selectivity in single conical nanopores. *Journal of Chemical Physics* **2006**, *124*, 104706.

[93] J. Cervera, A. Alcaraz, B. Schiedt, R. Neumann, P. Ramirez, Asymmetric selectivity of synthetic conical nanopores probed by reversal potential measurements. *Journal of Physical Chemistry C* **2007**, *111*, 12265-12273.

[94] P. Ramirez, P.Y. Apel, J. Cervera, S. Mafe, Pore structure and function of synthetic nanopores with fixed charges: tip shape and rectification properties. *Nanotechnology* **2008**, *19*, 315707.

[95] J.A. Manzanares, S. Mafe, J. Pellicer, Current Efficiency Enhancement in Membranes with Macroscopic Inhomogeneities in the Fixed Charge-Distribution. *Journal of the Chemical Society-Faraday Transactions* **1992**, *88*, 2355-2364.

[96] E.L. Cussler, *Diffusion: Mass Transfer in Fluid Systems*, 3rd ed., New York: Cambridge University Press, 2009.

[97] P.Y. Apel, I.V. Blonskaya, O.L. Orelovitch, P. Ramirez, B.A. Sartowska, Effect of nanopore geometry on ion current rectification. *Nanotechnology* **2011**, *22*, 175302.

[98] P. Dejardin, E.N. Vasina, V.V. Berezkin, V.D. Sobolev, V.I. Volkov, Streaming potential in cylindrical pores of poly(ethylene terephthalate) track-etched membranes: Variation of apparent zeta potential with pore radius. *Langmuir* **2005**, *21*, 4680-4685.

[99] Z. Siwy, P. Apel, D. Baur, D.D. Dobrev, Y.E. Korchev, R. Neumann, R. Spohr, C. Trautmann, K.O. Voss, Preparation of synthetic nanopores with transport properties analogous to biological channels. *Surface Science* **2003**, *532*, 1061-1066.

[100] K. Schmidt-Rohr, W. Hu, N. Zumbulyadis, Elucidation of the chain conformation in a glassy polyester, PET, by two-dimensional NMR. *Science* **1998**, *280*, 714-717.

[101] M. Firnkes, D. Pedone, J. Knezevic, M. Doblinger, U. Rant, Electrically Facilitated Translocations of Proteins through Silicon Nitride Nanopores: Conjoint and Competitive Action of Diffusion, Electrophoresis, and Electroosmosis. *Nano Letters* **2010**, *10*, 2162-2167.

[102] R. Schmuhl, A. van den Berg, D.H.A. Blank, J.E. ten Elshof, Surfactant-Modulated Switching of Molecular Transport in Nanometer-Sized Pores of Membrane Gates. *Angewandte Chemie International Edition* **2006**, *45*, 3341-3345.

[103] X. Zhu, Y. Liu, J. Huang, G. Li, A pH-Responsive Gate Fabricated with Nanochannels and Nanoparticles. *Chemistry – A European Journal* **2010**, *16*, 1441-1444.

[104] R. Casasús, E. Climent, M.D. Marcos, R. Martínez-Máñez, F. Sancenón, J. Soto, P. Amorós, J. Cano, E. Ruiz, Dual Aperture Control on pH- and Anion-Driven Supramolecular Nanoscopic Hybrid Gate-like Ensembles. *Journal of the American Chemical Society* **2008**, *130*, 1903-1917.

[105] M. Ali, P. Ramirez, S. Mafe, R. Neumann, W. Ensinger, A pH-Tunable Nanofluidic Diode with a Broad Range of Rectifying Properties. *ACS Nano* **2009**, *3*, 603-608.

[106] I. Vlassiouk, Z.S. Siwy, Nanofluidic diode. *Nano Letters* **2007**, *7*, 552-556.

[107] M. Wanunu, A. Meller, Chemically modified solid-state nanopores. *Nano Letters* **2007**, *7*, 1580-1585.

[108] M. Ali, Q.H. Nguyen, R. Neumann, W. Ensinger, ATP-modulated ionic transport through synthetic nanochannels. *Chemical Communications* **2010**, *46*, 6690-6692.

[109] T.K. Rostovtseva, S.M. Bezrukov, ATP Transport Through a Single Mitochondrial Channel, VDAC, Studied by Current Fluctuation Analysis. *Biophysical Journal* **1998**, *74*, 2365-2373.

[110] N.O.L. Seto, S.V. Evans, Specificity in protein-carbohydrate recognition. *Current Organic Chemistry* **2000**, *4*, 411-427.

[111] J.C. Sacchettini, L.G. Baum, C.F. Brewer, Multivalent protein-carbohydrate interactions. A new paradigm for supermolecular assembly and signal transduction. *Biochemistry* **2001**, *40*, 3009-3015.

[112] R.J. Pieters, Carbohydrate Mediated Bacterial Adhesion. *Bacterial Adhesion: Chemistry, Biology and Physics* **2011**, *715*, 227-240.

[113] S.B. Bankar, M.V. Bule, R.S. Singhal, L. Ananthanarayan, Glucose oxidase - An overview. *Biotechnology Advances* **2009**, *27*, 489-501.

[114] T.W. Siegel, S.R. Smith, C.A. Ellery, J.R. Williamson, P.J. Oates, An enzymatic fluorometric assay for fructose. *Analytical Biochemistry* **2000**, *280*, 329-331.

[115] Tony D. James, Marcus D. Phillips, S. Shinkai, *Boronic Acids in Saccharide Recognition*, The Royal Society of Chemistry, Cambridge, 2006.

[116] S. Park, H. Boo, T.D. Chung, Electrochemical non-enzymatic glucose sensors. *Analytica Chimica Acta* **2006**, *556*, 46-57.

[117] A.P. Davis, R.S. Wareham, Carbohydrate recognition through noncovalent interactions: A challenge for biomimetic and supramolecular chemistry. *Angewandte Chemie-International Edition* **1999**, *38*, 2978-2996.

[118] M.D. Phillips, T.D. James, Boronic acid based modular fluorescent sensors for glucose. *Journal of Fluorescence* **2004**, *14*, 549-559.

[119] Z.S. Siwy, Ion-current rectification in nanopores and nanotubes with broken symmetry. *Advanced Functional Materials* **2006**, *16*, 735-746.

[120] J. Yan, G. Springsteen, S. Deeter, B.H. Wang, The relationship among pK(a),pH, and binding constants in the interactions between boronic acids and diols - it is not as simple as it appears. *Tetrahedron* **2004**, *60*, 11205-11209.

[121] T.D. James, S. Shinkai, Artificial receptors as chemosensors for carbohydrates. *Host-Guest Chemistry* **2002**, *218*, 159-200.

[122] G. Springsteen, B.H. Wang, A detailed examination of boronic acid-diol complexation. *Tetrahedron* **2002**, *58*, 5291-5300.

[123] J. Plank, J. Blaha, J. Cordingley, M.E. Wilinska, L.J. Chassin, C. Morgan, S. Squire, M. Haluzik, J. Kremen, S. Svacina, W. Toller, A. Plasnik, M. Ellmerer, R. Hovorka, T.R. Pieber, Multicentric, randomized, controlled trial to evaluate blood glucose control by the model predictive control algorithm versus routine glucose management protocols in intensive care unit patients. *Diabetes Care* **2006**, *29*, 271-276.

[124] L.I. Bosch, T.M. Fyles, T.D. James, Binary and ternary phenylboronic acid complexes with saccharides and Lewis bases. *Tetrahedron* **2004**, *60*, 11175-11190.

[125] Y.L. Zhang, X.M. Gao, K. Hardcastle, B.H. Wang, Water-soluble fluorescent boronic acid compounds for saccharide sensing: Substituent effects on their fluorescence properties. *Chemistry-a European Journal* **2006**, *12*, 1377-1384.

[126] P.M. Rudd, T. Elliott, P. Cresswell, I.A. Wilson, R.A. Dwek, Glycosylation and the immune system. *Science* **2001**, *291*, 2370-2376.

[127] A.D. Nisbet, R.H. Saundry, A.J.G. Moir, L.A. Fothergill, J.E. Fothergill, The Complete Amino-Acid-Sequence of Hen Ovalbumin. *European Journal of Biochemistry* **1981**, *115*, 335-345.

[128] W.L. Hulse, R.T. Forbes, A nanolitre method to determine the hydrodynamic radius of proteins and small molecules by Taylor dispersion analysis. *International Journal of Pharmaceutics* **2011**, *411*, 64-68.

Appendix

List of Abbreviations

αHL ..... α-hemolysin
AAO ..... Anodic aluminum oxide
APBA ..... 3-aminophenylboronic acid
ATP ..... Adenosine-triphosphate
BHb ..... Bovine hemoglobin
BSA ..... Bovine serum albumin
EDA ..... Ethylene diamine
EDC ..... *N*-(3-dimethyl-aminopropyl)-*N*-ethylcarbodiimide hydrochloride
EDL ..... Electrical double layer
FESEM ..... Field emission scanning electron microscopy
FIB ..... Focused ion beam
HCl ..... Hydrochloric acid
HCOOH ..... Formic acid
I–V ..... Current – voltage
KCl ..... Potassium chloride
KOH ..... Potassium hydroxide
MV^{2+} ..... Methyl viologen
NaOH ..... Sodium hydroxide
NDS^{2-} ..... 1,5-naphthalene disulfonate
PA ..... Propylamine
PC ..... Polycarbonate
PEI ..... Polyethyleneimine
PET ..... Polyethylene terephthalate
PFP ..... Pentafluorophenol
PI ..... Polyimide
pI ..... Isoelectric point
PNP ..... Poisson and Nernst-Planck
SEM ..... Scanning electron microscope
Si ..... Silicon
Si_3N_4 ..... Silicon nitride
TEM ..... Transmission electron microscope

List of Figures

List of Tables

List of Publications

[1] Quoc Hung Nguyen, Mubarak Ali, Veronika Bayer, Reinhard Neumann and Wolfgang Ensinger, Charge-selective transport of organic and protein analytes through synthetic nanochannels. *Nanotechnology* **2010**, *21,* 365701.

[2] Quoc Hung Nguyen, Mubarak Ali, Reinhard Neumann, and Wolfgang Ensinger, Saccharide/glycoprotein recognition inside synthetic ion channels modified with boronic acid. *Sensors and Actuators B: Chemical* **2012**, *162*, 216-222.

[3] Quoc Hung Nguyen, Mubarak Ali, Saima Nasir and Wolfgang Ensinger, Fabrication of Nanochannel Arrays for the Selective Transport of Ionic Species. *Nanopores for Bioanalytical Applications: Proceedings of the International Conference, The Royal Society of Chemistry* **2012**, 83-88.

[4] Mubarak Ali, Quoc Hung Nguyen, Reinhard Neumann and Wolfgang Ensinger, ATP-modulated ionic transport through synthetic nanochannels. *Chemical Communications* **2010**, *46*, 6690-6692.

[5] Mubarak Ali, Patricio Ramirez, Quoc Hung Nguyen, Saima Nasir, Javier Cervera, Salvador Mafe, and Wolfgang Ensinger, Single Cigar-Shaped Nanopores Functionalized with Amphoteric Amino Acid Chains: Experimental and Theoretical Characterization. *ACS Nano* **2012**, *6*, 3631-3640.

[6] Mubarak Ali, Saima Nasir, Quoc Hung Nguyen, Jugal Kishore Sahoo, Muhammad Nawaz, Tahir, Wolfgang Tremel, and Wolfgang Ensinger, Metal Ion Affinity-based Biomolecular Recognition and Conjugation inside Synthetic Polymer Nanopores Modified with Iron-Terpyridine Complexes. *Journal of the American Chemical Society* **2011**, *133*, 17307-17314.

[7] Saima Nasir, Mubarak Ali, Quoc Hung Nguyen and Wolfgang Ensinger, Stimuli-triggered Permeation of Ionic Analytes Through Nanopores Functionalised with Responsive Molecules, *Nanopores for Bioanalytical Applications: Proceedings of the International Conference, The Royal Society of Chemistry* **2012**, 76-82.

[8] Mubarak Ali, Saima Nasir, Quoc Hung Nguyen, Reinhard Neumann and Wolfgang Ensinger, Biochemical Sensing with Chemically Modified Synthetic Ion Channels, *Nanopores for Bioanalytical Applications: Proceedings of the International Conference, The Royal Society of Chemistry* **2012**, 32-37.

[9] Mubarak Ali, Saima Nasir, Patricio Ramirez, Ishtiaq Ahmed, Quoc Hung Nguyen, Ljiljana Fruk, Salvador Mafe, and Wolfgang Ensinger, Optical Gating of Photosensitive Synthetic Ion Channels. *Advanced Functional Materials* **2012**, *22*, 390-396.

The Curriculum Vitae (CV) is not included in the online version due to data protection reasons.